Model-Based Control of Tollmien-Schlichting Waves using DBD Plasma Actuators

An Experimental Study

G.N.Desouza

TUDelft

Model-Based Control of Tollmien-Schlichting Waves using DBD Plasma Actuators

An Experimental Study

by

G.N.Desouza

to obtain the degree of Master of Science
at the Delft University of Technology,
to be defended publicly on Thursday, 26 April 2018 at 9.00 AM.

An electronic version of this thesis is available at `http://repository.tudelft.nl/`.

TUDelft

Preface

This document is written in order to fulfil the requirements for obtaining the degree of Masters in Aerospace Engineering. This thesis also marks the end of two and a half years of studies at TU Delft, which has been such an adventure and an incredible learning experience, both academically and personally. No work is performed in isolation, and needless to say, the research presented here is a culmination of efforts, ideas and insights by a number of people.

First of all, I am incredibly grateful to my parents for instilling a sense of curiosity and ambition in me. If it weren't for their constant support, I doubt I would be where I am right now. I am especially thankful to my mother, who sacrificed and saved a lot so we would have enough to pursue what we wanted.

I am also very thankful to my two supervisors, Marios Kotsonis and Henry Tol, for the opportunity to work on such an exciting project in experimental aerodynamics. Marios has a way of making complicated concepts seem simple and was always available whenever I had (sometimes even trivial) questions. Henry, for teaching me the value of being rigorous and independent in carrying out my work, I am very grateful.

I cannot fail to mention two very special people who have been vital in helping me complete my studies in Delft. Nitant, for pulling me out of a very dark place and showing me the light at the end of the tunnel and Bram, for keeping me alive and healthy and dealing with my lack of cleanliness. I am so glad to have met you both.

And finally, I would like to also thank Leo Molewijk and Stefan Bernardy for their assistance in making the experiments run smoothly at the Low-Speed Laboratory as well as their coffee-table conversations.

G.N.Desouza
Delft, March 2018

Summary

The ability of laminar flow control to damp the onset of laminar-to-turbulent transition is an appealing tool for both researchers and aircraft companies, as this means a reduction in skin-friction drag. Over unswept wings, the leading cause of this transition is the growth of linear instabilities called Tollmien-Schlichting (TS) waves. Studies have shown that attenuating the strength of these waves can delay the onset of transition. One of the techniques, called active flow control, seeks to target the specific modes of TS waves by using certain control techniques. Over the years, researchers have attemped to use various model-free (control systems that do not use knowledge of the physical system) and model-based techniques (those that do use knowledge of the physical system) with the objective of targeting these linear instabilities, with much success.

One such model-based technique, called the Linear Quadratic Gaussian (LQG) compensator, was designed by Tol et al. (2017) with a white-box approach to estimate the perturbations in the flow by using the discretized form of the 2-dimensional linear Navier-Stokes equations. Rather than using any form of system identitification or data from prior experiments or simulations (such as DNS), these equations were directly used to formulate the state-space system and to create reduced-order models (ROM), which are used for designing the controllers. This is a unique approach in controller design. Motivated by the ability of this designed compensator to effectively estimate, target, and thus reduce the TS modes in a numerical setting, the feasibility and performance of this actuator remained to be tested in a wind-tunnel. The research objective of this thesis is thus to test the validity of such a controller and investigate its performance. In order to do this, two experimental campaigns were carried out.

In the first experimental campaign, Tollmien-Schlichting waves were sought to be created, observed and quantified. For this an existing wind-tunnel setup was modified such that an adverse pressure gradient over a flat plate would cause said TS waves to grow in the boundary layer. This pressure gradient was measured using existing pressure-tabs present along the length of the plate. Sensitive microphones embedded at fixed positions within the wall of the flat-plate measured the minute pressure fluctuations which are caused due to the flow-perturbations. Particle Image Velocimetry (PIV) was then used to study the fluctuation statistics while Proper Orthogonal Decomposition (POD) was used to isolate and quantify the most dominant TS modes. A series of six free-stream velocities (U_∞=6.2, 6.6, 7, 9, 9.4 and 9.8 m/s) was selected as the test range.

Results of the first experiment showed that clear Tollmien-Schlichting waves were observable at two positions: for the case of U_∞=6.4, 6.6 and 7 m/s, they were visible between Microphones 3 (at x=400 mm) and 4 (x=500 mm) and for the case of U_∞=9, 9.4 and 9.8 m/s, between Microphones 2 (at x=300 mm) and 3 (x=400 mm). However, in order to perform control, it was important that these waves are not only linear between at least two microphones, but also sufficiently strong at both. The higher velocity range (U_∞=9, 9.4 and 9.8 m/s) fulfilled both requirements. For this case, C_p measurements showed that transition occured at around x=420 mm. Power-Spectral Density (PSD) analysis of the filtered microphone signals demonstrated that the TS waves were strong and amplified: the spectral energy of the peak frequencies had grown by two orders of magnitude (from -60 dB at Microphone 2 to -20dB at Microphone 3).

Analysis of the boundary layer profiles also showed the presence of an inflection point within the boundary layer, which indicated the presence of inviscid instabilities. The analysis of the fluctuation statistics (RMS profiles, Reynolds stress profiles and Turbulent Kinetic Energy) tell a similar story, with the double-peaks in the RMS profiles starting to become more visible closer to the position of the downstream microphone (at x=400 mm), a clear TS wave footprint. The case U_∞ = 9.4 m/s was thus selected as the nominal design condition for which the compensator used for control was designed.

The second experimental campaign of the thesis was carried out with the objective of studying the validity of the controller and investigating its performance. The two microphones between which sufficiently strong TS were observable (Microphone 2 and 3) from the first campaign, were chosen as the upstream and downstream sensors in the control domain. A dielectric-barrier discharge (DBD) plasma actuator was placed at a distance of 1 cm downstream of the upstream sensor. The control signal was executed using a Field-Programmable Gate Array (FPGA) in a CompactRio device, which fed the output voltage signal to the high-voltage amplifier which in turn was used to drive the plasma actuator.

The performance of the controller was investigated at its nominal design conditions (U_∞= 9.4 m/s and V_{pp}=9kV) and for its robustness (at off-design conditions U_∞= 8.6, 9, 9.8 and 10.2 m/s). The conclusions were

drawn by studying the PSD of the downstream microphone signal without control (uncontrolled case), with constant forcing (open-loop case) and LQG control (closed-loop case). At the nominal design conditions, the PSD plots showed a reduction of energy of two orders of magnitude of the peak frequency for the open loop case. The closed loop performed even better, demonstrating a reduction of four orders of magnitude of the peak frequency. However, for the closed-loop control it was observed that there was control spillover at the lower TS frequencies (<130Hz). In order to see the effect of the controller on the whole signal, the RMS of the downstream pressure signal was studied. This showed a maximum additional reduction of 55% in the RMS of the pressure fluctuations, compared to the open loop case.

At the off-design conditions, the effect of the peak-to-peak voltage (V_{pp}) and the free-stream velocity were analysed. For both cases, LQG control performed better than open-loop control, with reductions of the energy of the peak-frequencies by one to four orders of magnitude. An overall reduction in the RMS of the downstream pressure signals of 30-60% was achieved compared to the open-loop case. Another observation was made. Although $9kV_{pp}$ performs better in damping the flow perturbations at the design conditions, $8kV_{pp}$ is more robust over a wider range of off-design velocities.

In conclusion, it can be stated that the designed LQG controller is feasible and is more effective at damping TS waves than if constant forcing were directly applied. The controller works best at the conditions it is designed for, and is more robust for a lower peak-to-peak voltage.

This study is the first time that a white-box approach of a model-based LQG controller is used to successfully damp naturally occuring TS waves experimentally. However, in order to ascertain whether this controller is better at damping TS waves compared to other model-based techniques, remains to be further investigated. Furthermore, although this study demonstrates a substantial reduction of the peak TS amplitudes, it is still unclear whether this is enough to show a considerable delay in transition, let alone one that is commercially beneficial.

Contents

List of Figures

List of Tables

Nomenclature

Latin Symbols

A	System-Matrix of the linearized discretizd reduced 2D Navier Stokes equations	[-]
B	Input-matrrix containing discretized body forces	[-]
C	Output-matrix	[-]
C_p	Coefficient of Pressure	[-]
D	Feed-forward/Feedthrough matrix	[-]
F	Feedback Gain Matrix	[-]
f	Body Forces	[N/m^3]
f_{ac}	Carrier-frequency of the plasma actuator signal	[Hz]
H	Shape factor	[-]
k	Online Tuning factor	[-]
L	Kalman-gain matrix	[-]
N	Number of snapshots	[-]
p	Presssure	[Pa]
R_{uu}	u - Normal Reynolds stress	[1/(m.s^2)]
R_{vv}	v - Normal Reynolds stress	[1/(m.s^2)]
R_{uv}	Shear Reynolds Stress	[1/(m.s^2)]
t	Time	[s]
u, U	Wall-parallel velocity component	[m/s]
v	Wall-normal velocity component	[m/s]
V_{pp}	Peak-to-peak voltage	[V]
V_{app}	Total Voltage Signal	[V]
w	Spanwise - velocity component	[m/s]
w_d	Disturbance Noise	[-]
w_n	Sensor noise	[-]
x	Cartesian coorinate parallel to the wall/flat plate , normal to the leading edge	[m]
y	Cartesian Coordinate normal to the wall	[m]
z	Cartesian coordinate in spanwise direction, parallel to the leading edge	[m]

Greek Symbols

α	Wave-number of disturbance	[1/m]
$\alpha^{(k)}$	Temporal coefficients of POD mode, k	[-]
δ	Boundary Layer Thickness	[m]
δ^*	Displacement Thickness	[m]
ε	Error in quantity	[-]
θ	Momentum Thickness	[m]
λ	Eigen-vector	[-]
λ	Wavelength	[m]
μ	Dynamic Viscosity	[kg/(m.s)]
ρ	Density	[kg/m^3]
σ	Standard deviation	[-]
ϕ	Modulated signal from Controller	[V]
$\phi^{(k)}$	Spatial Eigen Function of POD mode,k	[-]
ϕ	Stream-function	[m^2/s]
ω	Angular-frequency	[rad/s]

Subscripts

∞	Quantity in the Free-stream
99	Quantity at the 99% Boundary layer
RMS	Root-Mean Square of the Quantity
dom	Dominant Quantity
unc	Uncontrolled mode (Control off)
con	Controlled mode (with and without LQG)
ol	Open-Loop (Constant Forcing)
r	Real
i	Imaginary
re	Reconstructed

Abbreviations

AWC	Active Wave Cancellation
DBD	Dielectric Barrier Discharge
DNS	Direct Numerical Simulation
FFT	Fast Fourier Transform
FOV	Field of View
FPGA	Field Programmable Gate Array
FXLMS	Filtered-x Least Mean Squares
LMS	Least Mean Squares
LQG	Linear-Quadratic Gaussian
MPC	Model Predictive Control
NS	Navier-Stokes
PIV	Particle Image Velocimetry
POD	Proper Orthogonal Decomposition
PSD	Power Spectral Density
RMS	Root Mean Square
ROM	Reduced Order Models
TKE	Turbulent-Kinetic Energy
TS	Tollmien-Schlichting

Accent

$\bullet'$	Fluctuating component
$\bar{\bullet}$	Mean component
$\hat{\bullet}$	Estimated Quantity

<div style="text-align: right;">1</div>

Introduction

Ever since the aviation boom in the second half of the 20th century, a tremendous amount of research (and funding) has gone into trying to make aircraft more fuel-efficient. With the rising cost of fuel, there is an extra incentive for Aerospace giants such as Lockheed Martin, Boeing and Airbus to actively look for more efficient methods by which they can lower the cost of maintenance, improve flight speeds as well as make airplanes more environment-friendly. In fact, Airbus projects that the next 20 years will see the production of over 35,000 new jets at a market value of US \$5.3 trillion, a sizeable investment. [4]

It is well agreed upon, both by the scientific community and by companies alike, that skin-friction is a major source of drag which needs to be reduced to create more efficient designs. This is the drag caused due to the viscosity of the fluid interacting with the wall surface. More specifically, it becomes larger when the flow has transitioned to turbulent from its laminar state. In fact, over a flat plate, the mean skin-friction is an entire order of magnitude larger for a turbulent boundary layer than that for a laminar boundary layer ((Fabbiane et al.(2014)) Thus, one of the goals over the years has been to delay the onset of laminar to turbulent transition.

The mechanism of transition is fairly well understood. The most widely accepted theory is that external perturbations such as noise and free-stream turbulence enter the boundary layer through a process known as receptivity (Morkovin(1994)).These perturbations grow as the boundary layer thickens, even more so if the pressure gradient is adverse. At some point, the disturbances and the energy in them become large enough that the flow is no longer laminar, and small turbulent spots begin to form, which disintegrate to form fully turbulent flow. When this occurs, transition is said to be achieved. For low free-stream disturbances over unswept wings, the dominant mechanism by which transition occurs is through the growth of Tollmien-Schlichting (TS) waves (Schmid and Henningson(2012)).

Cancellation of TS Waves

Over the years, many experimental studies have been performed with the sole objective of controlling the growth of TS waves. The idea is that since Tollmien-Schlichting waves in their initial stages are inherently linear in nature, the principles of superposition of waves should apply. This means that, if appropriately timed, a counter-wave of opposing magnitude should, in principle, be able to cancel the TS waves. Although simple in theory, this is a lot harder to implement due to a variety of reasons. One, TS waves are not single frequency waves. They often occur as a bundle of frequencies. Two, the very nature of the viscous boundary layer causes the amplitudes of the disturbances within it to grow, often meaning that some frequencies get amplified and eventually cause transition while others simply die out. All these reasons have ,however, still not deterred serious experimental efforts in this regard.

Early attempts at damping Tollmien-Schlichting(TS) waves involved superimposing mono-frequency waves of opposite phase and amplitude (Milling(1981),Liepmann and Nosenchuck (1982)) linearly upon artificial disturbances generated in a water-tunnel. Other studies involved damping naturally occuring disturbances (Ladd(1990)) as well as the introduction of classic control elements such as reference sensors and actuators.

More recently, Herbert et al. (1996) demonstrated a thorough cancellation of TS waves using neural networks to adapt the output signal based on the disturbances. In 2003, Sturzebecher and Nitsche managed to successfully damp natural TS waves over an airfoil using a combination of slot and membrane actuators. They

---

[4]Technical Report: Airbus Global Market Forecast 2017-2036 Growing Horizons, D14029465, Issue 4. April, 2017.

observed that a reduction in amplitude of the disturbances of 94% could be obtained by using an adaptive control mechanism. With the rising interest in the use of plasma actuators as a forcing tool, Grundmann and Tropea(2008) managed to also demonstrate considerable cancellation of TS waves over a flat plate(and also observe a delay in transition). They operated the actuators in steady and pulsed modes, with an operating frequency equal to that of the most-dominant TS frequency. Kotsonis et al. (2015) took this a step further by combining the use of Dielectric Barrier Discharge (DBD) plasma actuators and the FXLMS (a type of adaptive feedback mechanism) logic to cancel TS waves over an airfoil.

While the goals have remained the same, the techniques over the method of control have differed. Broadly categorized, the type of control strategies employed are either model-free (which does not require any knowledge of the underlying physics of the system) or model-based (which utilizes the knowledge of the underlying physical mechanisms). Each has its own benefits and challenges. While model-free methods are often quite robust in experiments, they are simply made with the objective of minimizing the error signal. In this regard, they lack a strong theoretical basis and are criticized as being "ad-hoc" and "fine-tuned". Model-based methods, conversely, have a strong physical basis, but are often very hard to model effectively without making assumptions, linearization and reduction. For example, the Navier-Stokes (NS) equation, the famous equation which physically describes a flow, can require upto 10^6 to 10^8 degrees of freedom in order to be modelled fully-resolved. Another challenge in model-based methods is the modelling of physical disturbances into the flow regimes (Bagheri and Henningson(2011)).

Linear Control Theory as a Tool for Flow Control

Control theorists over the past two decades realized that there is some overlap between the principles that govern linear control theory and those of hydrodynamic stability. The fact that disturbances within wall-bounded flows are inherently linear in their initial stages, sensitive to amplification and have a convective time-delay are three salient features which exist in many linear control systems. The behaviour of such systems can be easily manipulated using knowledge of already existing optimal and robust controllers (Bagheri and Henningson(2011)). The application of such control techniques to the equations governing linear instabilities and their amplification in laminar flows, means that these disturbances too can be modelled and controlled (Bewley and Liu(1998)). Such "white-box" model-based techniques provided a solid physical and control foundation which, if modelled correctly, could be used as a base for controlling TS waves. Many researchers jumped at this idea. Joshi et al.(1997) was one of the first to institute linear control theory into small disturbance flows numerically. They found the controllers to be robust over a wide range of Reynolds numbers. More recently, Dadfar and Hanifi(2015) employed two model-based methods, the Linear Quadratic Gaussian (LQG) controller an the Model-Predictive Controller (MPC) to actively damp Tollmien-Schlichting instabilities over an airfoil numerically. They used reduced-order models (ROM) to model the sensors and actuators and the linearised NS equation to model the physical dynamics of the system. Interesting review articles on the research efforts of using model-based approaches in cancelling flow-disturbances numerically can be found in Bagheri and Henningson(2011) (for wall-bounded flows) and Sipp and Schmid (2016) (for a broader range of flows).

A considerable number of experimental efforts with regards to using model-based approaches to cancel flow-disturbances were also performed over the years. Juillet et al.(2014) used a combination of system-identification and feed-forward control design to damp flow perturbations in channel flow. The mode of actuation was blowing and suction. Goldin et al.(2013) utilized the model-predictive control (MPC) to damp Tollmien-Schliching waves over an unswept wing. Gautier and Aider (2014) performed closed-loop control of amplifier flows using a feed-forward auto-regressive moving-average exogenous (ARMAX) for backward facing step flows. Kurz et al. (2013) was one of the first to experiment with a hybrid transition control approach using DBD plasma actuators to damp TS waves in a wind-tunnel setting. They combined the use of having a wall-parallel momentum addition (through constant forcing) for the mean boundary layer stabilization with an active wave cancellation (AWC) technique for actively damping the flow-perturbations. This modulated signal is obtained by using an improved extremum seeking controller and is based on the extended Kalman-filter. They observed that the combined use of the hybrid signal was more effective at damping TS waves (and achieving transition delay) that each individual approach employed in isolation.

Fabbiane et al.(2015) were the first to experimentally test the use of a Linear Quadratic Gaussian (or LQG, a type of linear model-based controller that uses Gaussian noise as input) compensator based on a white-box model to damp (artificially generated) TS waves in a wind-tunnel. The disturbances and plasma actuators were modelled by volume forcings (and the results of Kriegseis et al.(2013)) while the compensator was de-

signed based on the state-space model (Glad and Ljung(2000)). A low-order approximation of the flow is constructed using the compensator and the upstream flow measurements.

Based on similar principles, Tol et al.(2017) developed a tool for the modelling and control of convective instabilities in wall-bounded flows using an LQG compensator. They demonstrated the use of a new perturbation modelling approach that effectively balances spatio-temporal resolution with respect to external disturbances and model order. In order to reduce the complexity of the system, the controller is synthesized by discretizing a localized control domain which contains the sensors and actuators, rather than taking the complete physical domain. The state-space system is derived from the linearized, discretized and reduced form of the incompressible Navier-Stokes equation. One of the unique benefits of their approach is that the reduced-order model (or ROM, which is used for designing the controllers) is derived directly from the linearized NS equations rather than using information from prior experiments,which may not always be available or numerical simulations (CFD or DNS), which are usually computationally expensive.

They observed that for a single frequency disturbance, nearly full cancellation is possible and for a stochastic disturbance of sensor and external noise, a wall shear stress reduction of 96% is seen. Thus it is very promising numerically and the natural next step is to investigate its performance in a wind-tunnel experiment. This thesis places itself in this very context, and based on this, the research question presented in the next section is formulated.

1.1. Research Question

As seen in the previous section, there is much potential in the use of white-box model based LQG techniques (such as that developed by Tol et al.(2017)) as a control mechanism to effectively damp Tollmien-Schichting waves. However, although this is numerically promising it needs to be validated in an experimental setting. Herein lies the motivation for this thesis. With that in mind, the following research question is formulated:

"Can LQG Model-Based Control be used to attenuate TS waves using DBD Plasma Actuators, in an experimental setting?"

In order to answer the question, an experimental approach is employed. The experiments are split in two campaigns,each with its own objective:(1) The characterization of the TS waves and (2)the Validation of the Controller. The purpose of the first campaign is to be able to obtain a system that is able to measure and quantify Tollmien-Schlichting waves in their linear stage. The purpose of the second campaign is to study the effect of the controller on the Tollmien-Schlichting waves using DBD plasma actuators. The performance of the controller is investigated for its design conditions and its robustness (at off-design conditions).

1.2. Research Scope

This study thus aims to add to the body of knowledge of judging whether controllers designed using a white/gray box approach (specifically, the Linear Quadratic Gaussian algorithm) are effective at damping linear flow-perturbations such as Tollmien-Schlichting waves. Furthermore, this study only investigates the effect of the controller on the TS waves, and not whether a significant delay in transition is achieved. Since the developed controller is novel and is being tested for the first time in a wind-tunnel, this study is not a comparative study. That is to say, it does not indicate if it is a better or worse technique to damp TS waves compared to existing model-free or model-based approaches.

1.3. Research Objective

From the Research Question as in Section 1.1 and Research Scope as in Section 1.2, the following research objective follows:

"To perform an experimental investigation on the feasibility of using LQG Model-Based Control for damping Tollmien-Schlichting waves with DBD Plasma Actuators"

As stated in Section 1.1, the objectives of the thesis were split with each experiment. For both campaigns, the following experimental wind-tunnel model was used.

A flat plate geometry is acquired and mounted in a wind-tunnel. A flexible wall placed opposite and parallel to it is used to adjust the degree of the adverse pressure gradient along the flat plate. Pressure tabs along the span of the plate are used to measure the pressure gradient and calculate the C_p distribution. Sensitive microphones with the ability to pick up TS amplitudes with a good resolution are embedded in the wall at specific locations. Finally, for the characterization of the TS waves and its statistics, flow quantification is performed using low-speed particle Image Velocimetry (PIV).

For the second part of the campaign, the same setup from the first campaign was used. Using the fitted pressure tabs,the same pressure gradient was recreated. Dielectric barrier Discharge (DBD) Plasma actuators were manufactured and placed between two microphones that demonstrated the most clear,strong and measurable TS waves from the first experiment. The controller designed by Tol et al. (2017) was implemented on a CompactRIO Field-Programmable Gate Array(FPGA) by National Instruments, in a Labview framework. Microphones were used to study the effect of the actuator on flow-disturbances. Performance at design conditions as well as robustness studies (performance at off-design conditions) were carried out.

Explicitly,the following sub-objectives are thus laid out:

- Acquire and Modify an Experimental Wind Tunnel Model : The flat plate within this model will form the main body over which the flow-perturbations within the boundary layer will be quantified, measured and later, controlled. The minute pressure fluctuations of the Tollmien-Schlichting waves are picked up using microphones which are embedded into the flat plate. A flexible wall is attached opposite to the flat plate which allows one to control the adversity of the pressure gradient.

- Calibration and Positioning of Microphones: Each microphone, due to its own internal construction, needs to be calibrated independently. This was done using an acoustic Pistonphone (which produces a signal of a given amplitude and frequency) against which each microphone is calibrated. The type and position of the microphones was chosen keeping in mind the region of the flow that is linear as well as the possible location of transition (which was estimated from literature).

- Experiment 1- Characterization of Tollmien-Schlichting waves : Before the controller can be applied, it is first important to be able to quantify and characterize the TS waves. The flexible wall is adjusted in such a way that clean TS waves are observable over at least two streamwise microphones for a range of free-stream velocities.

- Analysis of Data : The Power-Spectral Density of each of the microphone gives the first idea of the spectral distribution and strength of the TS waves. The properties of the boundary layer and quantification of the flow and its fluctuations is performed using low-speed planar Particle Image Velocimetry (PIV). Furthermore, Proper Orthogonal Decomposition (POD) isolated the different energy modes present in the flow and allows one to view the most dominant ones. These can then be used to reconstruct the flow, using only the dominant modes.

- Experiment 2 - Validation of the Controller : This experiment utilizes the setup from the first experiment, with the only difference being the addition of a plasma actuator which will be used to control the TS waves and the system-setup used to generate the control signal (using a CompactRio Field-Programmable Gate Array (FPGA) device). Based on the results of the first experiment and the control design, the actuator is positioned between two microphones such that the upstream microphone acts as the sensor. The downstream microphone records the downstream signal.

- Investigation of Controller Performance: By analysing the Power Spectral Density and the Root-Mean-Square (RMS) of the microphone signals at different free-stream velocities and base-voltages, the performance is studied for its design and off-design conditions (also known as robustness). The effect of the plasma actuator is examined for both the open-loop case (constant forcing) and the closed-loop case (LQG modulated forcing) as well as the benefit of using the modulated signal over constant forcing.

1.4. Thesis Outline
The structure of the thesis is outlined as follows.

Chapter 2 describes some preliminary theories about the boundary layer, ways to quantify it as well as the theories on the growth of TS waves, their prediction using Linear Stability Theory and the e^N Method.

Chapter 3 provides a literature study into the attenuation of Tollmien-Schlichting waves over the years, using different types of actuators, in experimental settings. The second part lays out some of the stategies employed for active flow control using linear-control theory, both numerical and experimental. The section further distinguishes between two such popular techniques : model-free and model-based approaches.

Chapter 4 explains the Methodology used in this thesis for carrying out and fulfilling the research objectives. This includes descriptions of the Power Spectral Density, Particle Image Velocimetry, Plasma Actuators as well as the structure of the LQG controller.

Chapter 5 describes the Experimental Setup that was used for both the experimental campaigns along with the test-matrices for the range of velocities and voltages.

Chapter 6 presents and analyses the results obtained from both Experimental campaigns

Chapter 7 outlines the main conclusions drawn from the results in Chapter 6 as well as recommendations and scope for future experiments.

2

Theoretical Models of the Boundary Layer

This chapter is aimed at providing the reader an introduction to the concepts related to boundary layer phenomenon. Section 2.1 presents the boundary layer theory as first introduced by Prandtl, along with the equations and the various parameters used to characterize it. Section 2.2 discusses the most well known theories used to explain the phenomenon of laminar to turbulence transition, along with Tollmien-Schlichting(TS) Waves. Section 2.3 describes the Linear Stability theory and how it can be used to study linear effects in a viscous flow.

2.1. Boundary Layer Theory

First proposed by Prandtl in 1904, this theory is one of the most well known to date that explains the viscous behaviour of flows over a surface. He claimed that the wall over which a fluid is flowing experiences a certain friction due to it (also called skin-friction), thereby causing the fluid in contact to behave as if it were stuck to it (the no-slip boundary condition). The velocity within the boundary layer then increases in the wall-normal direction until it eventually reaches the external inviscid flow velocity. Although it is nearly impossible to find the exact point at which this local velocity becomes equal to the free stream velocity, there are a number of ways in which the "boundary-layer" can be defined, and this region has certain properties which are of great interest in fluid dynamics.
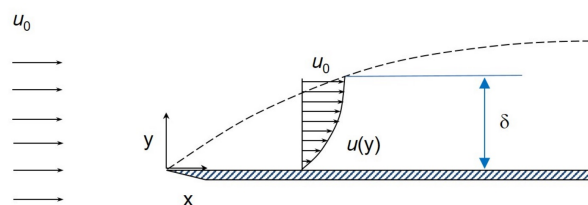
Figure 2.1: Velocity profile within the boundary layer over a flat plate

The boundary layer thickness(δ) is a function of a number of things, the chief of them being the fluid velocity, the fluid viscosity and the shape of the body – collectively termed the Reynolds number. The thickness of the boundary layer is still relatively small compared to the length of the surface(the order of a few millimeter for low speed flows). As the flow progresses, the thickness of the boundary layer increases. After a certain point, the fluid particles start to leave the boundary layer and the flow is no longer attached to the wall, a phenomenon known as separation.

2.1.1. Boundary Layer Equations

Prandtl derived the boundary layer equations doing an order of magnitude analysis of the governing Navier-Stokes equations. The 2D Incompressible Navier Stokes Equations (Schlichting (1968)) are given by Equation 2.1 and 2.2, x being the wall-parallel direction and y being the wall normal direction. For a full derivation, the reader is referred to White(1974).

$$\rho \left(\frac{\partial}{\partial t} + u.\nabla \right) u = f - \nabla p + \mu \nabla^2 u \tag{2.1}$$

$$\frac{\partial u}{\partial x} + \frac{\partial v}{\partial y} = 0 \tag{2.2}$$

In these equations u is the velocity vector, f is the body-force vector, ∇p is the pressure-gradient vector, μ is the dynamic-viscosity (constant) and ρ is the density (constant).

For the boundary layer, Prandtl found that the components and velocity gradients along the wall are often orders of magnitude larger than those in the wall-normal direction. In order to simplify the above equations, an order-of-magnitude or scaling analysis is done. If u and v are the streamwise and wall-normal component of velocity respectively, the simplified Boundary layer equations are given by Equation 2.3, Equation 2.4 and Equation 2.5, obtained from the x- momentum, y-momentum and continuity equations respectively.

$$u \frac{\partial u}{\partial x} + v \frac{\partial u}{\partial y} = -\frac{1}{\rho} \frac{\partial p}{\partial x} + v \frac{\partial^2 u}{\partial y^2} \tag{2.3}$$

$$\frac{1}{\rho} \frac{\partial p}{\partial y} = 0 \tag{2.4}$$

$$\frac{\partial u}{\partial x} = -\frac{\partial v}{\partial y} \tag{2.5}$$

The above equations reveal a few things for the case of a viscous boundary layer. One, the pressure does not vary in the wall-normal direction, for all given x positions. This means that the pressure in the inviscid far stream is assumed to to be the same as that within the boundary layer. Since in the far-stream, the pressure is uniform and we assume no vortices to be present (streamlines are mostly straight), the Bernoulli equation is applicable.

$$\frac{p}{\rho} + \frac{1}{2} U^2 = 0 \tag{2.6}$$

For the special case of flow when U(x)= constant or dU/dx=0, over a semi-infinite flat plate, Blasius (1908) noted that self-similar solutions existed under certain transformations, thus deriving the popular Blasius solution. It should be noted that for a Blasius boundary layer, the pressure gradient is zero. If an adverse pressure gradient exists, the flow is termed Falkner-Skan, such as in this thesis.

2.1.2. Boundary Layer Parameters
In order to quantify the boundary layer, it is standard practice to analyse the bounary layer thickness (δ_{99}), displacement thickness (δ^*), momentum thickness (θ) and the shape factor(H).

99 % Boundary Layer Thickness
This is regarded as the best approximation of the boundary layer thickness and is the point from the wall at which the velocity of a particle within the boundary layer is equal to 99% of the free-stream velocity U_∞. Thus

$$u(\delta_{99}) = 0.99 U_\infty \tag{2.7}$$

Displacement Thickness
Displacement thickness(δ^*) is a measure of the displacement caused by the boundary layer to the external flow field. It is thus a measure of the shift that needs to be made to the wall when inviscid flow is considered , given that the total mass flow remains the same. For an incompressible flow (White(1974)),

$$\delta^* = \int_0^\infty \left(1 - \frac{u(y)}{U_\infty} \right) dy \tag{2.8}$$

Momentum Thickness

It is the distance by which the wall would have to be moved in the wall normal-direction for an inviscid velocity (U_∞), in order to give the same momentum flux in the given region for a real viscous fluid. For an incompressible flow(White(1974)),

$$\theta = \int_0^\infty \frac{u(y)}{U_\infty}\left(1 - \frac{u(y)}{U_\infty}\right)dy \qquad (2.9)$$

Shape Factor

The ratio of the displacement thickness(δ^*) to the momentum thickness(θ) gives the shape factor(H) . The value of this term indicates nature of the flow.

$$H = \frac{\delta^*}{\theta} \qquad (2.10)$$

A higher value of H indicates the presence of a strong adverse pressure gradient. A higher shape factor means that for a given flow condition, the mass flux is larger than the momentum flux i.e. more fluid is flowing with lesser momentum , which corresponds to laminar flows. A lower shape factor corresponds to more turbulent flows. Typically, the value of H for laminar flows (in a Blasius boundary layer) is greater than 2.59 and that for turbulent flows is lesser than 1.4 (Schlichting (1968)). The shape factor is also a measure of the fullness of the velocity profile. Within a laminar boundary layer, an increasing value of H means that as the flow starts to become increasingly non-linear, the velocity-profile starts to become less and less full.

2.2. Laminar to Turbulence Transition

The phenomenon of transition was first demonstrated by Osborne Reynolds in his famous water-dye experiment in 1883 at the University of Manchester. It was through this experiment that the dimensionless constant i.e. the Reynolds number was introduced. Furthermore, he proposed the idea that a fluid flow can be expressed as a sum of its mean and fluctuating components - a concept that later came to be known as Reynolds-decomposition. His proposed theoretical model and mathematical framework form the basis of most fluid dynamics models.

To this day, however, the entire process of transition is not completely understood. A a number of stages within this process have been identified over the years and studied in order to understand and control it – which will be discussed in this section.

2.2.1. Receptivity

Morkovin (1994) described the process of receptivity as the process when external acoustic or vortical disturbances enter the boundary layer, causing minute perturbations within it. There is a transfer of energy from these external perturbations to the particles present within the boundary layer. The amplification and degree of receiving (or receptivity) of these unsteady disturbances depends largely on the type of flow and the surface in question – higher disturbances will cause more perturbations to enter the boundary layer. These then amplify as the boundary layer grows and cause the flow to transition into the turbulent regime. Saric et al. (2002) showed that that acoustic disturbances tend to develop Tollmien-Schlichting waves on unswept wings while vortices tend to lead to cross-flow instabilities on swept wings.
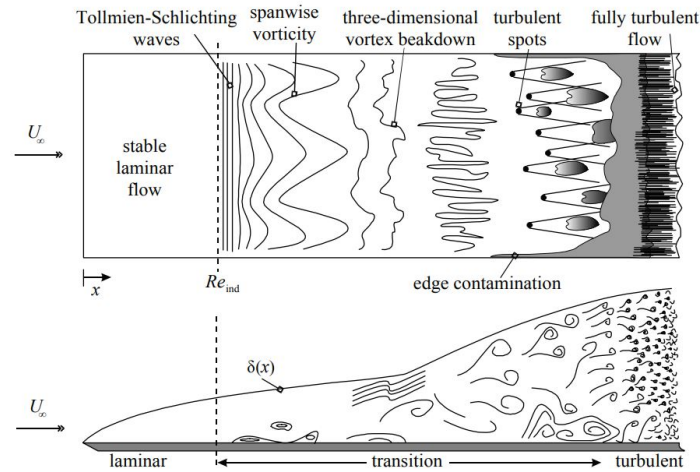
Figure 2.2: Growth of the Boundary Layer. Figure taken from Schlichting and Gersten (2000)

Figure 2.3 describes some of the known ways in which a flow may transition. On moving from left to right in the figure, the environmental disturbances are increasing i.e. for the left most path (A), the external disturbances are the lowest and for the right most path, they are higher. For path A, the initial perturbations are taken up by the boundary layer and grow to form primary instabilities. These waves are linear and are primarily the reason why there is the greatest potential to control the flow at this stage. Tollmien (1929) and Schlichting (1933), former students of Prantl, effectively studied these linear waves and in their honour, these waves were called Tollmien-Schlichting waves. As the flow further progresses, the flow starts to distort in three-dimensions, leading to secondary disturbances. These disturbances often amplify very fast making control at this point almost impossible. Klebanoff et al. (1962) called these secondary distortions as Λ -vortices (sometimes called hairpin vortices (Theodorsen (1952)) , also because they look like an inverted-V. These Λ-vortices then decay (breakdown) and lead to the formation of random turbulent spots which eventually lead to transition. (Kachanov(1994); Schlichting and Gersten (2000)).
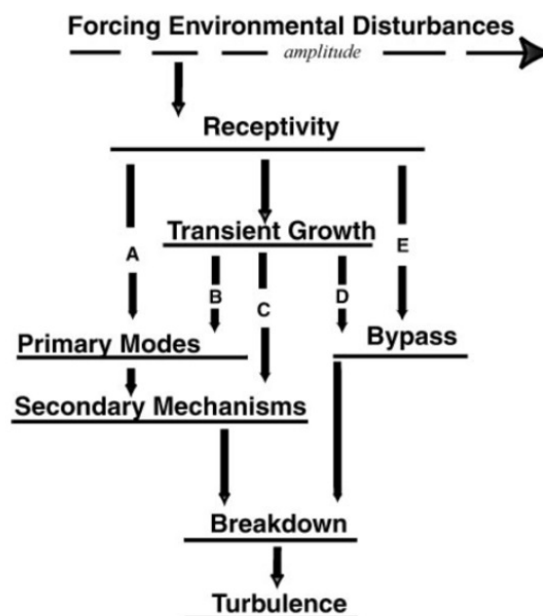
Figure 2.3: Transition mechanisms. Reproduced from Saric et al. (2002)

When the external disturbances are slightly higher, the fluid directly demonstrates transient properties. Here, depending on the amplitude and Reynolds number, it can develop primary instabilities (Path B), sec-

ondary instabilities (path C) or completely bypass the linear phase and transition into turbulence (bypass transition) (Reshotko (1976)).

Amongst all the stages of laminar to turbulence transition, the non-linear stage is less well understood or quantified. The linear amplification stage is more researched and known to be one of the slowest to grow compared to the other steps in the transition process. Thus modifications made to the flow at this stage have a significant effect on the transition Reynolds number. Thus the factors that determine this linear amplification eventually also determine the value of the transition Reynolds number (Gad-el Hak (1989)). This fact will be exploited in this thesis.

2.2.2. Tollmien-Schlichting Waves

Tollmien (1929) and Schlichting (1933) were the first to introduce the idea of the destabilizing effects of viscosity in fluid flows, by using asymptotic solutions to the Orr-Sommerfeld Equations. Only 15 years later, Schubauer and Skramstad (1948) demonstrated experimentally that indeed TS waves arose due to these "laminar boundary layer oscillations" .

Figure 2.4 shows an experiment conducted by Werle (1980) [1] on the visualization of TS waves at ONERA institute, France. The linear instabilities can be very well recognized as the waves in their growth stages before they start to become non-linear and eventually breakdown.
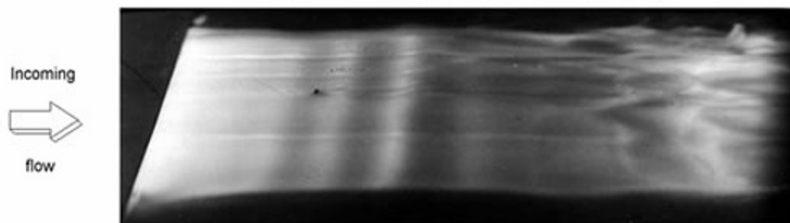
Figure 2.4: Visualization of TS waves, growth and breakdown. Experiment performed by Henry Werle (1980), Onera photographs [1]

One of the remarkable properties of TS waves, as mentioned earlier, is that they are linear instabilities. This means that if timed properly, in principle, an anti-wave of equal magnitude can be superimposed on the existing wave and it should be able to cancel it. Although theoretically promising, in practice this has proved to be a bit harder for a number of reasons. Firstly, Tollmien-Schlichting waves are not single frequency waves. They exist as a band of frequencies which grow as the boundary layer thickens. A single-frequency wave will not be able to cancel all these frequencies. Furthermore, among these frequencies, some get amplified and lead to transition while others die out. Secondly, there is no method that can damp TS waves to their entirety since, even effective damping leaves small perturbations in the flow which get amplified as the boundary layer grows. Sturzebecher and Nitsche (2003) tried to tackle this problem by installing multiple actuator-sensor systems downstream. They managed to successfully reduce the tridimensionalization of the TS waves by using active-control feedback mechanisms. Kotsonis et al (2015) also demonstrated the damping of TS waves using the same active control mechanism.
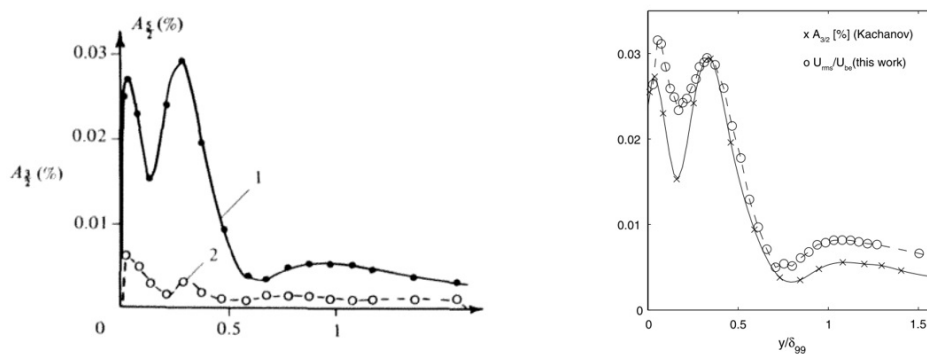
Figure 2.5: Typical y-profiles of amplitudes for TS waves1) Kachanov and Levchenko (1984) 2) Grundmann and Tropea (2008)

---

[1]Onera photographs: http://www.onera.fr/en/dmae/intrinsic-stability-of-flows

More recently, Grundmann and Tropea (2008) tried to demonstrate the occurrence of TS waves in their experiments and compared the typical turbulence level profiles characteristic of TS waves: the presence of a small peak at roughly δ_{99} with a minima just before it and an increase of turbulence near the wall. The double peaks observed before x=0.5 are another clear sign of the presence of TS waves. However, their experiment consisted of artificially exciting the boundary layer. The drawback of this is that, this could also amplify existing disturbances apart from adding new ones to the existing flow that were already growing naturally. Thus, although they do observe a substantial cancellation of the growing TS waves, these are not naturally occurring and their boundary layer contains extra disturbances than the 2-D TS waves generated by the excitation of the actuator. Chapter 3 will talk about more of the existing techniques used to damp TS waves in detail, their advantages and drawbacks.

2.2.3. Breakdown

Schubauer and Skramstad (1948) explained transition as the starting point when the boundary layer gets separated from the wall due to the presence of an adverse pressure gradient. Klebanoff et al. (1962) called the tridimensionalization of the TS waves as Λ-vortices. They showed that there are three types of Λ-vortices, the K-type, the H-type and the C-type, each a very small percentage of U. As the boundary layer grows, these 3D vortices start morphing into 3 dimensional fluctuations which grow into turbulent spots. The spots grow entraining the fluid around it and eventually coalescing together until the energy is dissipated into the entire boundary layer and the flow becomes entirely turbulent.

2.3. Linear Stability Theory

One of the most popular theories used by fluid-dynamicists to model According to Arnal (1992) ,for the case of a viscous flow over a flat-plate, 75% of the flow between the location of the leading edge and the point of transition can be considered as linear. Linear stability theory can be used to understand the initial growth in the disturbances in this linear part of a boundary layer flow. The idea is that by superimposing a fluctuating component on the mean flow, the growth or decay of these disturbances can be calculated. This is also the principle of the famous Orr-Sommerfeld equation.

2.3.1. The Orr-Sommerfeld Equation

Independently discovered by Orr(1907) and Sommerfeld(1908) ,this equation is obtained when a disturbance is applied to the base flow and then substituted into the 2-D incompressible Navier-Stokes equation. The derivation is briefly described below.

The 2D incompressible Navier-Stokes Equation can be written as

$$\frac{\partial u}{\partial t} + u.\nabla u = -\nabla p + \frac{1}{\text{Re}}\nabla^2 u \tag{2.11}$$

Any flow can be represented as the sum of its average and fluctuating parts

$$\begin{aligned}
u &= \bar{u} + u' \\
v &= \bar{v} + v' \\
w &= \bar{w} + w'
\end{aligned} \tag{2.12}$$

where $\bar{u}, \bar{v}$ and $\bar{w}$ are the x,y and z-components of the base or averaged flow and u',v' and w' are the fluctuating components.

For pressure,

$$p = \bar{p} + p' \tag{2.13}$$

Substituting the equations 2.12 and 2.13 in equation 2.11 we see that the mean flow variables satisfy the NS equation. Subtracting this from the mean flow equation gives the equation in terms of perturbations. Since the flow is 2 dimensional, w=0 and since it is wall-bounded, $\bar{v}$=0. As the disturbance velocities are small, the term u'u' is very small and can be neglected. This gives the following set of equations

$$\frac{\partial u'}{\partial x} + \frac{\partial v'}{\partial y} = 0 \tag{2.14}$$

$$\frac{\partial u'}{\partial t} + U\frac{\partial u'}{\partial x} + v'\frac{\partial U}{\partial y} + \frac{\partial p'}{\partial x} = \frac{1}{\text{Re}}\nabla^2 u' \tag{2.15}$$

$$\frac{\partial v'}{\partial t} + U\frac{\partial v'}{\partial x} + \frac{\partial p'}{\partial y} = \frac{1}{\text{Re}}\nabla^2 v' \tag{2.16}$$

The stream function can be defined as

$$\psi(x, y, t) = \phi(y)e^{i(\alpha x - \omega t)} \tag{2.17}$$

where α is the wave-number of the disturbance and $\omega(=\alpha c)$ is the frequency in cycles per unit time. For the spatial mode of analysis, ω is real and α is complex ($\alpha = \alpha_r + i\alpha_i$), α_i representing the growth-rate or amplification.

Thus if

- α_i <0, the disturbance grows and the flow is unstable

- α_i >0, the disturbance damps and the flow is stable

- α_i =0, the disturbance neither damps nor grows and the flow is neutral

The disturbance velocity components u' and v' are

$$u' = \frac{\partial \psi}{\partial y}$$

$$v' = -\frac{\partial \psi}{\partial x}$$

and the equation

$$(\bar{u} - c)\left(\frac{\partial^2 v'}{\partial y^2} - \alpha^2 v'\right) - \frac{\partial^2 \bar{u}}{\partial y^2}v' + \frac{iv}{\alpha}\left(\frac{\partial^4 v'}{\partial y^4} - 2\alpha^2\frac{\partial^2 v'}{\partial y^2} + \alpha^4 v'\right) = 0 \tag{2.18}$$

is the well-known Orr-Sommerfeld equation, where c is the propagation speed.

Solution of the Orr-Sommerfeld equation
Writing it in dimensionless form,

$$(u^* - c^*)\left(\phi'' - \alpha_\delta^2\phi\right) - u^{*\prime\prime}\phi + \frac{i}{\alpha_\delta\text{Re}_\delta}\left(\phi'''' - 2\alpha_\delta^2\phi'' + \alpha_\delta^4\phi\right) = 0 \tag{2.19}$$

where $u^* = \frac{\bar{u}}{U_e}$, $c^* = \frac{c}{U_e}$, $\phi = \frac{v'}{U_e}$, $\alpha_\delta = \alpha\delta$ and $\text{Re}_\delta = \frac{U_e\delta}{v}$.

The above equation is a fourth order linear homogeneous equation. For a given flow profile, it can be solved for its eigen values α_δ and c^*. For a spatial instability $\alpha_{\delta i}^* < 0$ and for a temporal instability $c_i^* > 0$.

The results of the Orr-Sommerfeld equation are commonly represented in stability diagrams or 'thumb curves' as shown in Fig. 2.6
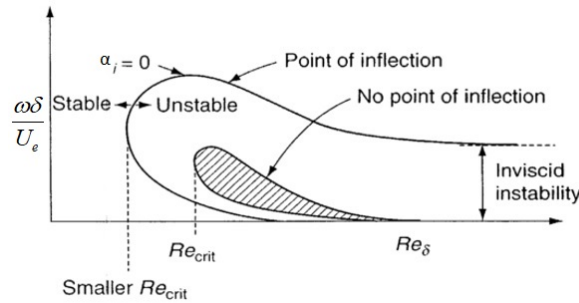
Figure 2.6: Neutral stability curve. Figured borrowed and modified from White (1974).

On the y-axis, the frequency of disturbances is increasing. The 'thumb' is the neutral curve where α_i=0 and the flow is neutral. Outside the thumb curve, all disturbances are damped. Thus α_i is positive and

the flow is considered stable. Inside the curve, $\alpha_i < 0$ and the disturbances amplify. If there is no point of inflection (usually when there is no adverse pressure gradient) the thumb seems to disappear with increasing Reynolds number. However, if there is a point of inflection in the velocity profile ($\frac{\partial^2 u}{\partial y^2} = 0$) this means that the thumb curve extends upto infinity, a necessary and sufficient condition for inviscid instabilities (Rayleigh (1879), Tollmien (1929), White (1974)). The critical Reynolds number is the smallest Reynolds number below which any linear disturbances in the flow will die out(Gad-el Hak (1989)).

2.3.2. e^N method

van Ingen (1956) and Smith and Gamberoni (1956) independently discovered a method to predict the location of transition based on the growth of the frequencies. For a particular frequency or wavelength having an initial amplitude a_o at x_o^* and an amplitude a_1 at x_1^*, the amplification factor $n(x^*)$ can be defined as

$$n(x^*) = \ln\left(\frac{a_1}{a_o}\right) = \int_{x_o^*}^{x_1^*} -\alpha_i \, dx^* \tag{2.20}$$

Thus the n-curves can be plotted for each frequency over the domain of the flow. The maximum amplification N-factor is taken as the envelope of all the n-factor curves. One such case is shown in Figure 2.7 for flow over a flat-plate.
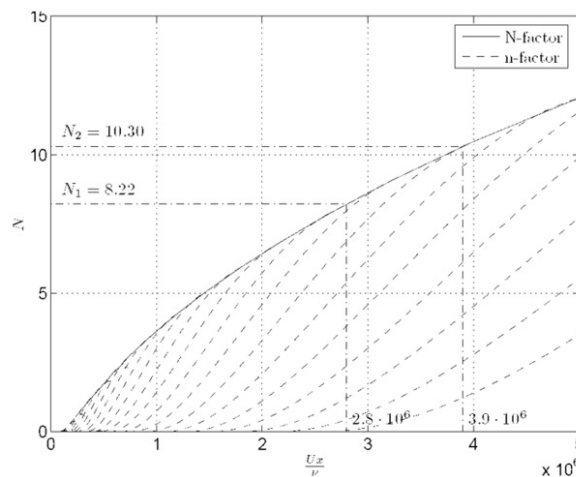
Figure 2.7: Growth of the n factors with Reynolds number for a flat plate. Taken from van Ingen(2008)

From previous experiments such as that by Schubauer and Skramstad (1948) , the Reynolds number corresponding to the location of transition is found out and from Figure 2.7, the corresponding N factor. For similar experiments under similar wind tunnel test conditions, the model can thus predict the location of transition at the known value of N. The paper of van Ingen (2008) states that for flows at low-Reynolds numbers transition is achieved when the value of N is around 8-10.

Spangler and Wells Jr (1968) argued that the turbulence of the wind tunnel plays a huge effect on the transition Reynolds number as these external "sound" disturbances often get added to the boundary layer through receptivity and cause transition earlier than if the turbulence level was lower. Mack (1977) studied the effects of turbulence of the wind tunnel on the N-factor and also proposed the following formula, where Tu is the turbulence level:

$$N = -8.43 - 2.4\ln(Tu) \tag{2.21}$$

Understanding the N-factor is very useful in predicting the location of transition as it gives not only the location of expected transition but also the values and ranges of frequencies that contribute most to the transition (using the code already developed at TU Delft). This will be useful for the purpose of this thesis as the controller will be designed to cancel these particular range of predicted frequencies.

3

State-of-the-Art

This chapter presents the attempts and developments made by various researchers in the damping of flow instabilities (primarily Tollmien-Schlichting waves), using varying methods of actuation as well as different control mechanisms.

Section 3.1 presents the state-of-the-art in the attenuation of TS waves, using mechanical and plasma actuators. Section 3.2 presents the types of control logic employed in flow-control as well as distinguishing between the two main contemporary types of control : Model free and model-based techniques.

3.1. Attenuation of TS Waves

Over a surface with zero sweep, Tollmien-Schlichting waves are one of leading types of instabilities that lead to transition in a laminar boundary layer. Damping them is therefore the next logical step required in order to delay the onset of transition. This idea is not new. A number of techniques using vibrating membranes, ribbons , flaps, wires and more lately plasma have been used to damp these instabilities by providing a forcing to the particles in the boundary layer. Such a force or disturbance producing body is termed an actuator. Cattafesta & Sheplak (2011) provide a robust classification of actuators based on function. In this section, however, only the mechanical and plasma actuators as well as their use in controlling flow instabilities will be discussed in detail.

3.1.1. Mechanical Actuators

Unlike fluidic actuators whose purpose is to inject or suck fluid out of the boundary layer (eg. suction and blowing), mechanical or moving object/surface actuators induce motion in the fluid. For example,Schubauer and Skramstad (1948) used the electrodynamic ribbon oscillator for their flat-plate boundary experiments. Katz et al. (1989), Seifert et al. (1998) used vibrating flaps, Viets et al. (1981) used rotating surface elements and Thill et al. (2008) used morphing surfaces to control the flow.

Sturzebecher and Nitsche (2003) used a series of sensors and actuators (slot and membrane) to successfully show a delay of transition by the cancellation of artificially induced TS waves, in an adverse pressure gradient.
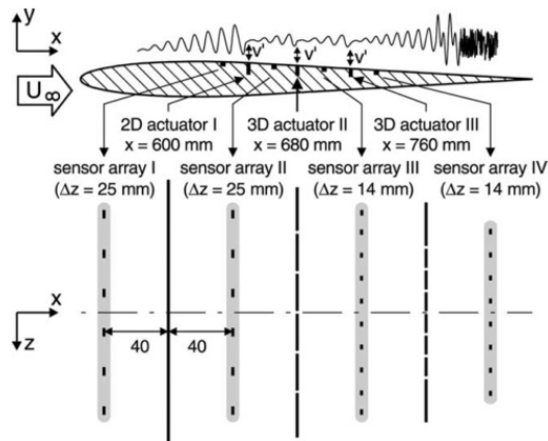
Figure 3.1: Series and spanwise actuator and sensor placement for the experiment of Sturzebecher and Nitsche (2003)

The idea was that in order to show a significant delay of transition it is important to vary the type and density of the actuators. In an adverse pressure gradient, the delay of transition caused due to one row of actuators can be very tiny since TS waves are rather sensitive and unstable. They quickly transition from linear to non-linear. By using a streamwise cascade of control and by varying the type of control and number of actuators per strip, they were able to have better control of the flow. Flush-mounted and membrane actuators to introduce anti-waves into the flow. These waves would be introduced at a phase of 180° so that the waves can be superimposed onto linear TS waves.

Their control was based on the following principle. The sensor generates a reference signal based on the flow above it. This is then sent to an actuator through a linear transfer function, equipped with FIR filters. This also known as a Filtered-x Least Mean Squares (FXLMS) algorithm. This function continuously adapts based on the error signal generated by the subsequent row of sensors, such as to minimize the error signal. Hence, this type of control it is also called 'adaptive control'. It is also a closed- loop feed forward type algorithm . They observed TS frequencies of 200-400 Hz. A reduction of 94% of natural and artificial TS waves (along with oblique waves) was found.

3.1.2. Plasma Actuators

The use of plasma actuators as a flow-control technique is gaining much attention amongst the scientific community. Their appeal of having almost none of the problems posed by mechanical actuators – lack of moving parts, robustness, fast response time and low power consumption make them a very viable candidate for effective flow control. They operate under a rather simple principle. By passing a high voltage through two conducting electrodes separated by a non-conducting medium,an electric field is generated. As the magnitude of the voltage and thus the electric field increases, a certain breakdown electric field(E_b) can be reached. When this happens, electrons in the surrounding air get ionized. More electrons move towards the anode, thus creating an 'electric wind' or plasma (Corke et al. (2010)). This plasma is known to have a local forcing effect on the surrounding region. Although the exact mechanism by which the plasma produces these forces is not yet fully understood, this does not mean that it's effects on fluid flow cannot be exploited.
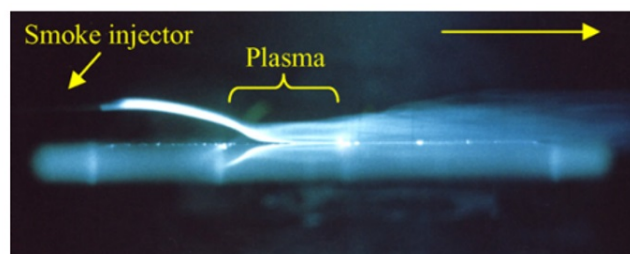
Figure 3.2: Effect of Plasma on a flow. Notice how the plasma also draws flow from above it ,making it bend. Picture borrowed from Moreau (2007).

Depending on the shape of the non-conducting medium, the direction of the forcing can be varied. When

employed within a boundary layer, this "body-force" can be used to exploit the properties of the boundary layer and manipulate the disturbances within it ,for example,by inducing counter-waves on existing Tollmien-Schlichting waves and also control cross-flow instabilities by damping sub-critical modes.

For the quantification of body forces due to DBD Plasma Actuators, Kotsonis et al. (2011) developed a method to calculate the thrust produced by DBD plasma actuators. In this method two assumptions are made. First, the body force is assumed to be quasi steady over the high-voltage cycles and second, prior to plasma actuation, the pressure gradient is taken to be zero. This was then used to estimate the input body-force matrix in the controller design. Quantification of these body forces is important in order to model the controller (Section 4.4.1).

3.1.3. Using Plasma Actuators to Damp TS Waves Experimentally

Grundmann and Tropea (2009) managed to demonstrate a delay of transition using plasma actuators operated in steady and pulsed mode. They showed that TS waves are cancelled considerably (by almost 20-30% amplitude) if the control actuator is operated at the same frequency as the most dominant mode(110Hz). An interesting thing to note is that the actuator does not distort the mean velocity profile in any way, only the RMS fluctuations. This shows that plasma actuators do not control transition by changing the characteristics of the flow, only the disturbances within it.(Reshotko (1976))

The PSD spectra (Figure 3.3) show that the first mode (at 110Hz) is damped considerably. Also the fourth and fifth harmonics seem to be damped, while the second and third don't seem to be affected. They also found that the power consumed by pulsed-mode operated actuators for active wave cancellation is only 12% of that used for steady-perturbation attenuation. However, the turbulence in the boundary layer remains the same for both actuation principles. This is another benefit of using plasma actuators in their pulsed mode.

(a) Mean and RMS Boundary layer profiles   (b) PSD spectra with and without control
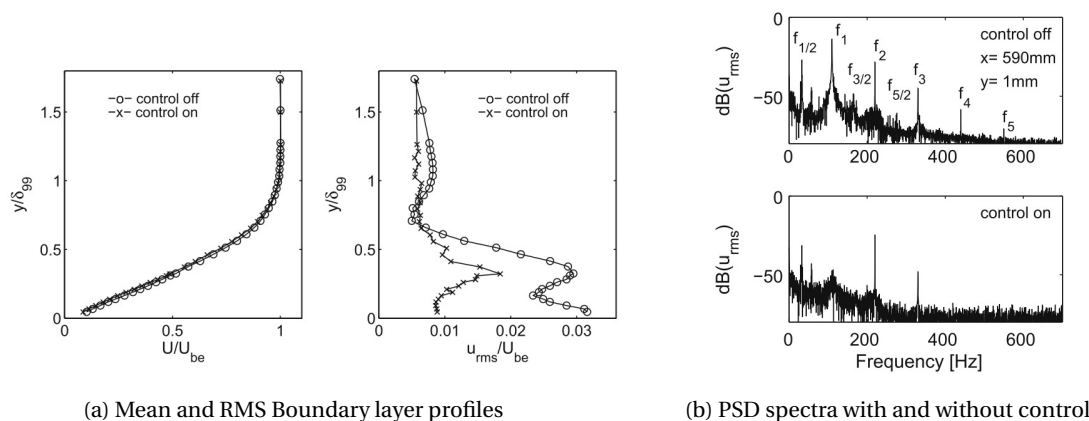
Figure 3.3: Results of the experiments conducted by Grundman and Tropea(2009). All measurements are taken 90mm downstream of the actuator

A criticism of their technique is that they only used a single frequency of actuation to damp TS waves, namely that of the dominant TS frequency at 110Hz. The problem with this is that there is the possibility of resonance between the actuation frequency and the frequencies in the disturbances. Furthermore, their study also shows that for an actuation frequency around the dominant TS wave range there is the possibility of beats (whose frequency is equal the difference of the frequencies). A possible solution to this is modulating the carrier frequency with a lower frequency, a technique which will be used in this thesis.

Kotsonis et al. (2015) also demonstrated the successful damping of naturally occurring TS waves over a NACA 0012 airfoil for low freestream velocities (17 to 25 m/s). They used adaptive filtered least-mean squared (FXLMS) control with Finite Impulse Response (FIR) filters, both using closed and open loop approaches (see next Section). A chordwise series of microphones were used at the midspan of the air-foil , to measure the surface pressure fluctuations. Control was done using DBD plasma actuators at a range of carrier frequencies and an amplitude of 10kV.

It was observed that there is a 50% reduction in amplitude for the case v=17m/s. Furthermore, the open-loop case seems to show a growth of the discrete instability modes, when the actuation frequency is in the instability region. Harmonics of this actuation frequency are also seen to grow in the flow. What they also observed was the "stretching effect" on the TS waves due to the directional plasma body forces.

3.2. Active Flow Control Techniques

Systems and control is a well-established discipline that utilizes important concepts for a wide variety of applications. For example, it is used to maintain the attitude of an airplane in auto-pilot, the temperature of a room using a thermostat, amongst many others. Its utilization in flow control however, is quite recent and especially with the improvement of the response time of many systems, is gaining acclaim among both the control and fluid-dynamics community.

This section first gives a broad overview of the different types of control used in active flow control (Section 3.2.1 and Section 3.2.2)). Section 3.2.3 talks about the numerical studies performed in damping flow instabilities using linear control theory followed by some experimental attempts (Section 3.2.4), including a short discussion of the differences in model-free and model-based techniques.
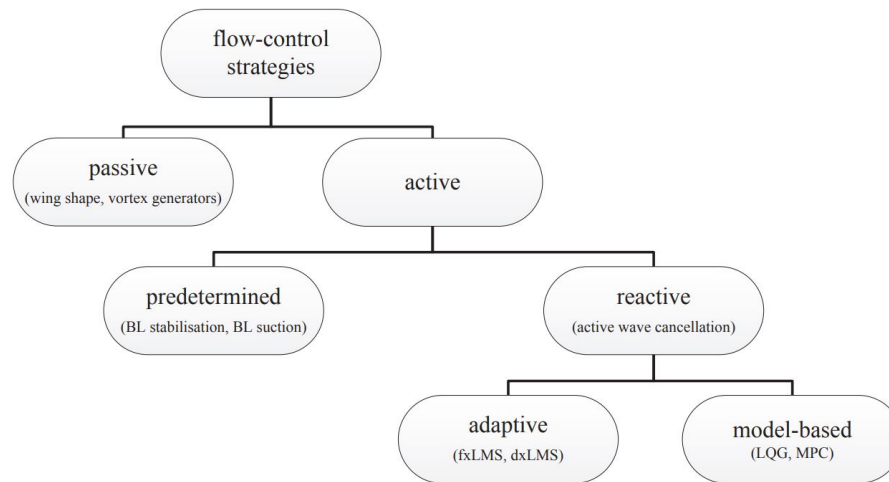
Figure 3.4: Classification of flow control strategies. Picture borrowed from Gad-el Hak (1989)

3.2.1. Adaptive Control

Adaptive control is a model-*free* technique which essentially uses a system through which the input signal is continuously adapted based on a feedback loop. This feedback loop often consists of an error signal which is then fed back to the control algorithm which seeks to minimize it. The adaptive algorithm used for flow-control applications is the Filtered-X Least Mean Squares (FXLMS) algorithm and is a popular model-free technique for the cancellation of TS waves (Sturzebecher and Nitsche (2003), Kotsonis et al. (2015)). Delayed-xLMS is another type of model-free technique used by Simon (2017).

Adaptive control is contrasted with model-based control in the sense that that it does not need a-priori information about the system (its model or physics in any sort) or any bounds on the uncertain parameters. It is simply used (often with system identification techniques) to statistically quantify the dynamic behaviour of a system, and seeks to optimize the problem by minimizing the error. Such modelling approaches are often 'black-box' in nature ,since these models are built purely on input-output data and are almost blind to the physics of the fluid system as it is virtually impossible to understand what goes on inside it (Brunton and Noack(2015)). This type of technique can be useful in cases where the model for the physical process is very complex.

3.2.2. Model-Based Control

Model-*based* control refers to the type of control system that utilizes a known existing physical model to describe the properties of the system. Here a certain quantity is estimated based on a known physical model, which is incorporated into the control algorithm. Thus information about the system is known a-priori and is used to estimate the unknown parameters. Depending upon the amount of system identification, this type of control can be termed either 'white-box' (no system identification) or 'grey-box'(some parameters found from system identification).

In active flow control, this effectively means that there is an upstream sensor which samples a given quan-

tity (say, pressure), feeds it into an algorithm that computes an output signal based on a prior defined model. The output signal from the algorithm (also called compensator) is then used to run the actuator present at a downstream location. Common forms of model-based control are H-infinity Loop shaping, Linear Quadratic Gaussian(LQG) control and Model-Predictive Control (MPC). In this thesis, LQG control will be performed.

LQG control is most popular for linear systems with incomplete state information i.e. the information for some state variables may not be available or measurable and needs to be estimated. In this regard, it considers that the system is disturbed by white Gaussian noise and seeks to minimise a predefined cost function (optimal control) which describe the features that need to be controlled. For further details on the principles of the LQG controller the reader is referred to the work of Athans (1971) and Schmid and Sipp(2016).

In this thesis, a reduced order model of the linearized and discretized Navier-Stokes Equations are used since the full equations have a large number of degrees of freedom and would not be practically implementable. The white Gaussian noise is assumed to be both disturbance noise (w_d) and sensor noise (w_n). The control objective is the minimization of the wall-shear stress. For specifics about the controller design utilized in this thesis, the reader is redirected to Section 4.4.1 or the paper by Tol et al. (2017).

Open Loop Control

Open loop control refers to the type of control where the signal is not manipulated by a controller. In the context of this thesis, it refers to the case in which constant forcing is applied. That is to say, no modulation of the signal is performed. Open loop active flow control is actually not new, with techniques such as suction being used as early as Prandtl. It works by stabilizing the mean-flow of the velocity profile, essentially, trying to "straighten-out" the inflection point in the velocity profile rather than affecting the disturbances in the flow. For plasma actuators, numerous studies (Grundmann and Tropea(2008), Seraudie et al.(2011)) have shown that a delay in transition is achieved by simply applying constant forcing.

Closed Loop Control

Closed loop control refers to the modification of the signal (used to drive the actuator) based on the controller output. In this thesis, it refers to the control applied with modulation or some form of addition to the base-signal. Experiments that utilize a control model to determine the output signal are generally closed-loop control systems. Kurz et al.(2013) tried to achieve transition control by utllizing plasma actuators in hybrid mode to cancel TS waves. They combined wall-parallel momentum addition (continuous mode or constant forcing) with active-wave cancellation using linear superposition (or modulated momentum injection). Widmann et al.(2013) characterized the interaction of the hybrid-mode operated plasma actuators with the TS waves, performed in Kurz et al.(2013), using Phase-Locked PIV. Simon (2017) performed in-flight experiments on a laminar-wing glove of a glider and demonstrated the cancellation of TS waves using plasma actuators with active-wave cancellation.

In this thesis, the intended control signal will be generated by the LQG model-based controller which will be added to an existing base-voltage. While the base-signal only stabilizes the mean-flow, the LQG control works by actively targeting the instabilities within the flow and trying to damp their amplitudes (without affecting the mean flow).

3.2.3. Numerical Studies that use Linear Control Theory to Damp Flow Instabilities

Bagheri and Henningson(2011) reviewed research efforts on the delay of laminar-turbulent transition using numerical simulations with a linear control approach. Their focus was mainly on flow over a flat plate and relied on the assumption that if the flow in the initial stages is indeed linear, it provides a suitable domain over which linear-control can be applied. They observed that for flow control of small amplitude disturbances, three things were in common for most physical systems and linear control theory: (1) For small upstream disturbances, the initial stages in the amplification process are inherently linear and can be modelled with known existing linear physical models (2) these disturbances often grow by several orders of magnitude and usually propogate downstream allowing a feed-forward system to be employed and (3) perhaps most significant for applied control design, is the time delay in observing the effects of the upstream external perturbations at a downstream location. This has implications on the way the controller is designed since it limits the degrees of freedom by which control can be applied. One of the main challenges is the the modelling of disturbance-specific statistics in both space and time, for which a number of approaches have been tried.

Dadfar and Hanifi(2015) employed two types of active control strategies - the Linear Quadratic Gaussian (LQG) and the Model-Predictive Controller (MPC) to attenuate TS disturbances within the boundary layer of an airfoil. The control strategies are based on reduced-order models of the sensors and actuators. Linearized

models of the Navier-Stokes (NS) equations are used to model the dynamics of the system and the body-forces of plasma actuators are modelled using volume forcings. The designed controller requires the use of upstream estimation sensor . For the LQG case, they even employed different strategies - the unconstrained controller, constrained controller and two adjacent controllers to see which control technique gave the best reduction of TS waves.

The interested reader is also referred to the review article by Sipp and Schmid (2016) which focuses on the developments in model-based approaches and the techniques most suitable for different types of flows.

3.2.4. Experimental Studies that use Linear Control Theory to Damp Flow Instabilities

Juillet et al.(2014) performed an experimental study to control natural flow-perturbations in channel flow for very low Reynolds numbers. They utilized simple blowing and suction technique as the method of actuation. The control approach involved the use of system-identification and feed-forward control design. The model assumes a linear relation between input and output variables. Rathnasingham and Breuer (2003) performed similar experiments using similar control techniques, for higher Reynolds numbers.

Goldin et al.(2013) utilized a model-predictive control(MPC) algorithm, a type of model-based technique to control Tollmien-Schlichting instabilities over an unswept wing. They used a type of flexible membrane actuator and compared the effects of using the linear negative superposition method to a biomimetic approach (an actively displacable wall that mimics a compliant wall). They were thus able to use different actuator setups and compare the efficiency of each.

Gautier and Aider (2014) performed experimental closed-loop control of an amplifier flow using a feed-forward auto-regressive moving-average exogenous (ARMAX) model for perturbed backward-facing step flows. The control algorithm, based on the principle as described by Hervé et al.(2012), uses system-identification to make up for the shortcomings of the model-based techniques to predict the external disturbances (such as noise) and their influences to the flow.

In a more closely related study, Kurz et al. (2013) developed a hybrid transition control tool to delay transition on an airfoil in a wind-tunnel setting using DBD plasma actuators. They combined two techniques of actuation traditionally employed separately for control: boundary layer stabilization using wall-parallel momentum addition and active-wave cancellation (AWC) using linear negative superposition. The modulated forcing is controlled using a modified extremum seeking controller which is based on an extended Kalman filter(EKF).
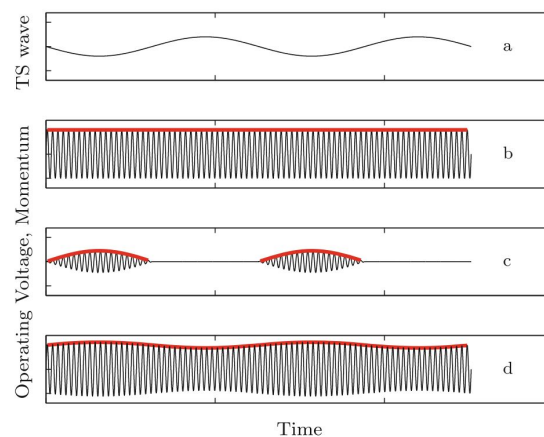
Figure 3.5: a) TS wave signal (b)Constant forcing open-loop control of the plasma actuator (c)Active-wave cancellation and (d)Modulated signal with the red-line showing the momentum-production (red-line) and the operating volatge(black-line). Figure borrowed from Kurz et al.(2013)

Although the frequency of the operating AC voltage to the plasma actuator is high (few kHz), a quasi-steady momentum addition to the boundary layer can be assumed (Kotsonis et al.(2011)). Thus the plasma actuator produces constant forcing which is utilized for the mean boundary layer stabilization. On top of that, the control algorithm generates a signal of the same frequency with the correct phase, but opposite amplitude which is added to the base-signal. This actively affects the flow perturbations present in the flow, without modifying the mean flow. The final modulated signal looks like that in Figure 3.5(d), with the red-line indicating the total momentum forcing.

Model-Free vs Model-Based Control

Fabbiane et al.(2015) were the first to experimentally compare the robustness of the Linear Quadratic Gaussian (LQG)(a model-based method) and the adaptive filtered-X least-mean-squares (FXLMS) techniques (a model-free method) by trying to delay transition through the attenuation of Tollmien-Schlichting waves. For the LQG control, the disturbances and the actuators were based on the forcings by Kriegseis et al.(2013)). A low-order approximation of the flow is computed using the compensator (based on the state space model from Glad and Ljung(2000)).
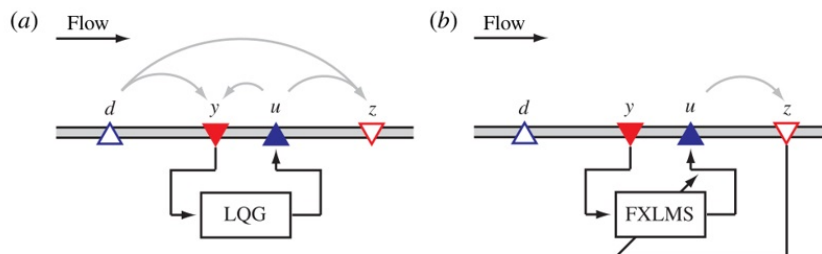
Figure 3.6: Schematic of the compensator for a) an LQG controller and b) an adaptive FXLMS controller (Fabbiane et al.(2015)

They found a number of things:

- Under the conditions it is designed for, the LQG controller shows the best performance when simulated numerically. However, when implemented practically, it was found that for a small change in the Reynolds number, its performance deteriorates linearly. As a result of this, an entire order-of-magnitude loss of performance is seen.

- The adaptive filtered-X least mean squares (FXLMS) has a more consistent performance even for significant deviations of the Reynolds number. Thus FXLMS adaptive control shows more robustness.

Although showing more promise experimentally (Kotsonis et al.(2015), Fabbiane et al.(2015)), adaptive control does possess a few drawbacks. One criticism is that it is not designed for the system in question and this is regarded as a "black-box " and "ad-hoc" model. Åström and Wittenmark(2013) argue that for control of flows using closed loop FXLMS control, stability of the closed loop system is not guaranteed and the energy of the disturbances is not reduced optimally.

Fabbiane et al. (2014)reviewed model-based versus model-free techniques using a single framework. They demonstrated some advantages of model-based techniques(LQG,LQR,MPC and Kalman filter) over model-free techniques(LMS and X-filtered LMS).

- Theoretically, model-based techniques are supported by a powerful and elegant basis. The instabilities can be addressed in a straight forward manner using controllability and observability, which model-free techniques lack. It also provides great optimality and physical insight into damping linear disturbances in a flow.

- Under certain restrictions, model-based techniques are known to provide stability guarantees and show good performances. Since they are designed to operate within certain voltage range, there is a lesser chance of short-circuit or breakdown of the actuator.

- There are a large number of free parameters used in the modelling of adaptive FIR filters and are often chosen in an ad-hoc manner. That is to say, they are chosen specifically for this purpose and cannot be generalized.

They also pointed out a few drawbacks of the model-based techniques :

- When tested experimentally,LQG lacks robustness and cannot account for changes in Reynolds numbers over the flow.

- For convectively unstable systems, the configuration choice of actuator and sensor placement for LQG control results in a feed forward system.

- Plasma actuators and disturbances such as free-stream turbulence and are difficult to model realistically using model-based control

Either way, both techniques have their pros and cons. More research is required using LQG controllers to study their effect on damping of naturally occurring TS waves, hence the motivation for this experimental thesis.

According to them, future research might move in the direction of hybrid-control techniques such as that performed by Kurz et al.(2013), where control is partially model-based for simplicity and optimality and adaptive control is used for experimental robustness.

4

Methodology

This section describes the methods and tools used to fulfil the objectives of this thesis - the characterization of the TS waves and their control using plasma actuators. Section 4.1 discusses the concept of Power Spectral Densities and how they can be used to understand the spectral energy of the frequencies of the flow-perturbations. Section 4.2 describes the technique used to quantify the flow, Particle Image Velocimetry (PIV), which is used to study the fluctuation statistics. Proper Orthogonal Decomposition(POD) (Section 4.3) is used to isolate the most dominant modes of energy in the flow. Finally, Section 4.4 gives a detailed description of the Linear Quadratic Gaussian (LQG) controller, its structure as well as the method of implementation in the wind-tunnel setting.

4.1. Measuring Instabilities: Power Spectral Density

Signals picked up by the microphones are in the time domain. Before the frequencies in these signals can be identified, they need to be converted into the frequency domain. A number of methods are available for these purposes. A commonly used technique, the Fourier analysis of a signal (also called Fast Fourier transforms or FFT) decomposes the signals.

A similar method is by performing a spectral density analysis of the signals using the method introduced by Welch(1967). Essentially this method takes a time sample of the signal and estimates the power of the different frequencies present in the signal. The power of a given signal in the frequency band $[f_1 f_2]$ is given by

$$P_{band} = 2 \int_{f_1}^{f_2} S_{xx}(2\pi f) df \qquad (4.1)$$

where S_{xx} is the power spectral density given by

$$S_{xx} = \int_{-\infty}^{\infty} \gamma(\tau) e^{-i\omega t} d\tau \qquad (4.2)$$

The number 2 appears in Equation 4.1 due to the fact that the power is distributed to both positive and negative frequencies.

The advantage of using the pwelch over the FFT method is the flexibility it affords in terms of defining the overlap windowsize , or the Hamming window. By being able to change the size of the overlap window one can vary the frequency resolution. A larger window means more data points are considered, giving a higher resolution and vice versa. Another advantage is that it reduces noise from the spectra. This may happen if the size of the sample is not large enough or the data is imperfect in some way.

To avoid these issues, we take a large number of sample points ($1.8x10^6$) which is measured by the microphones placed along the span of the flat plate. (See Section 5.2.3). The noise is also filtered out using a fourth order Butterworth filter with a band pass of 10 and 10,000Hz.The Matlab function *pwelch* then performes the spectral density estimation using a window size of 10,000 and and a window overlap of 50%.

4.2. Flow Quantification

In order to study the statistics of the boundary layer and the flow in general, Particle Image Velocimetry (PIV) is used. It is a technique which uses snapshots from a high-resolution camera and analyses them to obtain the movement of the particles, i.e., the velocity vectors in the field-of-view (FOV). One of the biggest advantages of this technique over other conventional imaging techniques is that it is non-intrusive. Thus, it does not affect the flow due to any physical presence. Furthermore, based on the requirement, the field of view can be made as large or small as possible (being limited by the camera system), allowing the user to flexibly adjust the system to his requirements.

This thesis utilizes low-speed planar PIV since 1)the flow-disturbances (TS waves) can be assumed to be two-dimensional 2)the velocity is less than 10 m/s and 3) only the time-averaged and fluctuation quantification profiles are of interest. This section presents the working principle, the sub-systems and the method of post-processing. For the specific details of the PIV sub-systems used for the experiment, the reader is directed to Section 5.4.

4.2.1. Principle

The main idea behind Particle Image Velocimetry (PIV) is to be able to measure the velocity of the flow in a certain region by measuring the movement of illuminated particles. These are captured by a camera at the same position on two subsequent images, separated by a small-time difference. The so called seeding or tracer particles are the ones whose movement help in determining the local flow velocity. Usually these are around the order of $1\mu m$ for gas/air flows and are small enough that they do not interfere with the flow in any way, physically or chemically. Typically, the concentration of seeding particles is in the order of 10^9 to 10^{12} particles/m^3 (Scarano (2013)). Thus, the particles are chosen in such a way that they are small enough not to interfere with the flow but large enough to scatter a sufficient quantity of light in order to be picked up by the camera. The seeding also has to be uniform, for which atomizers such as fog-generators are used.
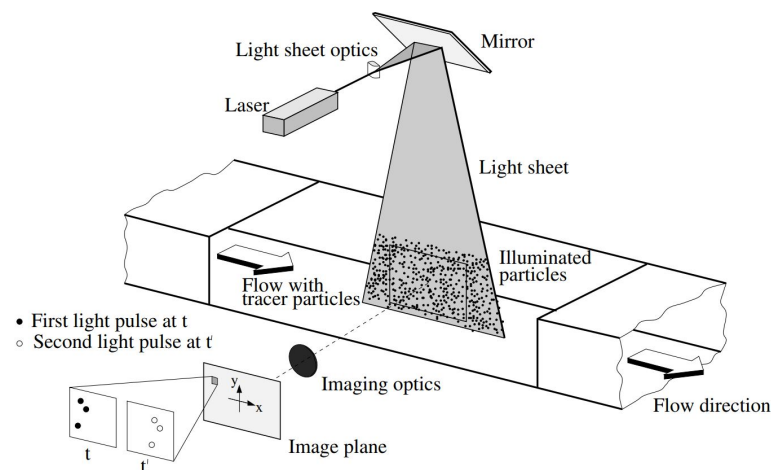
Figure 4.1: Working Principle of PIV. Figure borrowed from Raffel et al. (2013)

Typically, the execution of PIV requires the use of several sub-systems. This mainly involves the laser-lens system, the flow-section to be quantified, the acquisition camera and lastly, the computer-system using which the entire system is controlled, the images stored and later processed.

The particles are illuminated using a pulsed laser, usually Nd:YAG, a type of solid-state laser. This is because they produce a strong pulsed, collimated and monochromatic beam which can be shaped into a thin-light sheet with the help of a cylindrical lens and focused using a spherical lens. The wavelength of light produced is 532 nm and a pulse energy of around 10mJ. Since it is able to shoot two consecutive pulses with a very short pulse duration (in the range of μs or even nano-seconds) they are ideal for quantifying low-speed flows.

The images taken at both pulses of the laser are captured by a charged-coupled device (CCD), in this case, a low-speed camera (acquisition frequency of a few Hertz). It is very important to adjust the camera setting and focus in such a way that the particle size is not smaller than the pixel size. This is done in order to avoid pixel-locking. A pixel is usually of the order of $10\mu m$ which is comparable to the size of a tracer particle. In

order to keep the particles well-resolved, the diameter of the particle should span about 2-3 pixels (Scarano (2013)).

After obtaining the image-pairs and storing them on the system, the images need to be processed. This is done with the help of the software DaVis 8.4, courtesy of LA Vision. The next section describes this process of evaluating the particle image motion.

4.2.2. Processing

The processing of the particle image motion can be summarized into four : windowing, cross-correlation analysis, sub-pixel interpolation and scaling. For a detailed explanation with examples the reader is referred to Raffel et al. (2013) or Wieneke (2017).

First, the entire image is divided into a specific number of windows called interrogation windows, each having a certain number of particles (usually 10). Each window-pair will give one vector. A statistical tracking operator performs the cross-correlation between each corresponding window from the two image-pairs. This means that it gives the average movement of the most (or all) particles in that window (equal to the distance of correlation peak from the origin, Figure 4.2). However,the distance obtained from the cross-correlation is in integer pixels while in reality the particle displacement is not in pixels. In order to get a more accurate value of displacement, a sub-pixel interpolation is performed, which gives a more accurate peak position and thus displacement vector.
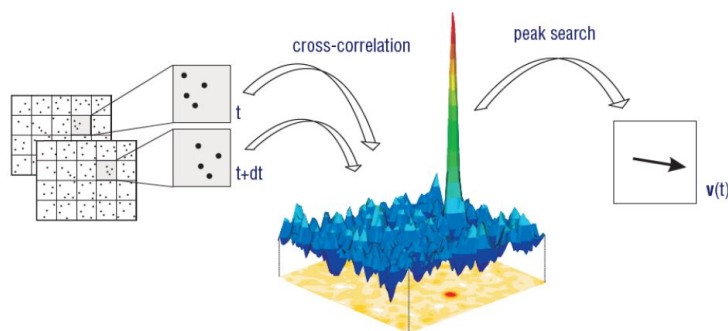
Figure 4.2: Cross Correlation of images. Figure borrowed from Wieneke (2017).

This entire process is done for each of the windows in the field of view to obtain an array of displacement vectors. In order to further improve the accuracy of the above measurements, first larger windows sizes are taken (64x64 or 48x48) to roughly estimate the value of the displacement. The process is further fine-tuned by performing the above process again using successively smaller window sizes (32x32 and 16x16) with every step (multi-pass), sometimes also taking an overlap . This is done to capture any particles that may have escaped the first window and have only moved to the beginning of the second window.

Finally, each displacement vector is divided by the time-difference(Δt) between the images and scaled with the pixel size and magnification to obtain the velocity vector for that window, and thus for the whole field. After obtaining the instantaneous velocity fields using Davis , they are converted into Matlab-readable formats, using which all the velocity field statistics (RMS, Reynolds stress, Turbulent Kinetic Energy) can be computed.

4.2.3. Fluctuation Statistics

Statistics of the fluctuations present within the flow can be qualitatively and quantitatively analysed by studying the contours of the Root-Mean-Square (RMS), Reynolds stresses (R_{uu}, R_{vv}, R_{uv}) and the Turbulent Kinetic Energy (TKE).

Root-Mean-Square Velocity

The first indication of the fluctuations can be observed in the RMS profiles (or even those of the standard deviation). The RMS for a particular x and y position is calculated as in Equation 4.3. This is then performed over the whole field-of-view to obtain the RMS profile. Here N is the number of snapshots obtained from PIV. Similarly, the RMS velocity can be found of the v' component.

$$U_{RMS} = \sqrt{\frac{1}{N}\sum_{i=1}^{N}|u_i'|^2} \tag{4.3}$$

Reynolds Stresses

After averaging the Navier-Stokes equations in order to account for the effects of turbulence, the total stress tensor (which is a non-linear term) is called the Reynolds stresses. Physically, it is the stresses (force per unit area) imposed by the turbulent component of the flow on the mean flow. For a fluid of density ρ, the normal and shear and Reynolds stresses are given by Equations 4.4a and 4.4b, respectively, where u' and v' are the fluctuating components in a 2-D incompressible flow.

$$R_{uu} = \rho\overline{u'u'}, R_{vv} = \rho\overline{v'v'} \tag{4.4a}$$

$$R_{uv} = \rho\overline{u'v'} \tag{4.4b}$$

Turbulent Kinetic Energy

Turbulent Kinetic Energy (TKE) is a measure of the kinetic energy of the eddies present in a turbulent flow. This is useful since a higher TKE value would mean the flow is more turbulent in those regions. It is defined as the mean of the root mean square of the velocity fluctuations. For 2D incompressible flows,

$$TKE = \frac{1}{2}\left(\overline{(u')^2} + \overline{(v')^2}\right) \tag{4.5}$$

4.2.4. Uncertainty Quantification

For independent uncorrelated samples , there is an uncertainty in the calculation of the averaged velocity fields. This also means that the error is propagated as one performs successive calculations on the mean and fluctuating fields, such as calculation of the Reynolds stresses and Turbulent Kinetic Energy. This is called the linear error propagation technique, studied and quantified by Sciacchitano and Wieneke(2016).

For a mean field constituted of N independent samples, the error in the mean ($\varepsilon_{\bar{u}}$) is inversely proportional to the number of samples as given by Equation 4.6 where σ_u is the standard deviation in u. In a similar way, the error in the mean v-component can be determined.

$$\varepsilon_{\bar{u}} = \frac{\sigma_u}{\sqrt{N}} \tag{4.6}$$

The error in the Reynolds stress calculation , where R_{uu} is the normal Reynolds stress field, can be calculated using Equation 4.7.

$$\varepsilon_{R_{uu}} = R_{uu}\sqrt{\frac{2}{N}} \tag{4.7}$$

Similarly, the error for the Reynolds normal stress field ($\varepsilon_{R_{vv}}$) can be obtained. Given a cross-correlation coefficient ρ_{uv} ,the error in the shear Reynolds stress($\varepsilon_{R_{uv}}$) is given by Equation 4.8.

$$\varepsilon_{R_{uv}} = \sigma_u\sigma_v\sqrt{\frac{1 + \rho_{uv}{}^2}{N-1}} \tag{4.8}$$

Furthermore, the error in the Turbulent Kinetic Energy is

$$\varepsilon_{TKE} = \frac{1}{2}\sqrt{\varepsilon_{R_{uu}}{}^2 + \varepsilon_{R_{vv}}{}^2 + \varepsilon_{R_{ww}}{}^2} \tag{4.9}$$

where $\varepsilon_{R_{ww}} = (\varepsilon_{R_{uu}} + \varepsilon_{R_{vv}})/2$, if the w-component is not present, as is the case in planar PIV.

4.3. Proper Orthogonal Decomposition

Proper Orthogonal Decomposition (POD) is a modal analysis technique that seeks to decompose a flow field into a number of modes based on the energy content. It is a method used to identify coherent structures present in the flow that may not be so easily distinguishable from PIV; since PIV often contains a lot of noise and the energy of the coherent structures is quite low to be isolated from the main flow using PIV.

For our analysis, the snapshot method as described in Sirovich(1987) will be used, while the execution in MatLab as described in Michelis (2017).

The eventual goal of POD is to be able to write the fluctuating component of the velocity field as a product of its corresponding spatial eigen function $\phi^{(k)}(x, y)$(k being the number of the mode) and temporal coefficient ($\alpha^{(k)}(t)$). They are related to the fluctuating component as

$$\mathbf{u}'(x, y, t) = \sum_{k=1}^{N} \alpha^{(k)}(t)\phi^{(k)}(x, y) \tag{4.10}$$

For this technique, the total number of modes equals the number of snapshots(N) taken.

First, a matrix is created containing the fluctuating components of u and v for all the given snapshots(1 to N),and is combined into a cell U. Here, 1 to M denotes the positions at which the velocity vectors are known.

$$U = [\mathbf{u}'^1 \mathbf{u}'^2 ... \mathbf{u}'^N] = \begin{bmatrix} u_1'^1 & u_1'^2 & ... & u_1'^N \\ \vdots & \vdots & \vdots & \vdots \\ u_M'^1 & u_M'^2 & ... & u_M'^N \\ v_1'^1 & v_1'^2 & ... & v_1'^N \\ \vdots & \vdots & \vdots & \vdots \\ v_M'^1 & v_M'^2 & ... & v_M'^N \end{bmatrix} \tag{4.11}$$

An auto-covariance matrix, R is defined as $R = U^T U$ using which an eigen-value problem ($Ra = \lambda a$) can be defined and solved to obtain the corresponding eigen-values λ and eigen-vectors a. The resulting solutions are arranged in descending order based on the size of the eigen values. Now each spatial function $\phi^{(k)}$ can be computed as

$$\phi^{(k)}(x, y) = \sum_{i=1}^{N} \Phi^{(k)}(t_i)\mathbf{u}'(x, y, t_i), \qquad k = 1, 2, ...N \tag{4.12}$$

where $\Phi^{(k)}$ is the normalized eigen vectors of R. The temporal coefficients,$\alpha^{(k)}$(t) (which gives the temporal evolution of the mode, k) are obtained by projecting the fluctuating part of the velocity field,$\mathbf{u}'(x, y, t_i)$ onto the POD modes $\Psi=[\phi^1 \phi^2 \phi^3 ... \phi^N]$ as

$$\alpha(t_i) = \Psi^T \mathbf{u}'(x, y, t_i) \tag{4.13}$$

In order to judge the energy associated with each mode, we can find the energy percentage of each mode compared to the total energy in all the modes.

$$E_{mode}(\%) = \frac{\lambda_{mode}}{\sum\limits_{i=1}^{N} \lambda_i} \tag{4.14}$$

The reconstructed flow field,u_{re} for a given number of modes can be obtained by summing the average flow field with the fluctuating part calculated for the most energetic modes (N_{re})

$$u_{re}(x, y, t) = \overline{u}(x, y) + \sum_{k=1}^{N_{re}} \alpha^{(k)}(t)\phi^{(k)}(x, y) \tag{4.15}$$

Here one is free to choose the number of modes to represent the reconstructed flow. Flows containing dominant flow structures can be reconstructed satisfactorily by considering the first few modes, which usually account for the most energetic flow structures (Meyer et al.(2007)).

4.4. The LQG Model Based Controller

In the past few decades, control theorists realized that linear theory could be applied in control design to model and even manipulate the disturbances within the laminar region of the boundary layer; since some of the principles guiding the growth of disturbances in this region (linearity of disturbances, amplification and convective time-delay) are well addressed in linear control design (Schmid and Henningson(2012)) . This meant that the same tools that were used to for linear control theory could also be used to study and model hydrodynamic stability (Fabbiane et al.(2014)).

Theoretically, the main goal then was to be able to model these disturbances and figure out a system that would be able to predict the growth of frequencies and cancel them. Experimentally, however, this proved to be more difficult to implement. It became commonplace to modify the setup .i.e. using ad-hoc techniques and fine-tuning in a very practical manner such that trial and error could be used to adjust and see which configuration worked best for cancelling disturbances. Thus the techniques became less and less transparent ,i.e. more black-box. This led to the implementation of feedback systems and other model-*free* techniques with the sole objective of reducing downstream disturbance. These techniques usually lack a sound theoretical basis. Experimentalists were hesitant to use white-box techniques as a control tool, due to their lack of robustness.

The most popular model-*based* techniques involved linear-quadratic regulators (LQG) which did have a sound elegant basis. However, things like plasma actuator forcing and disturbances such as free-stream turbulence, etc. are very difficult to mode individually. Tol et al. (2017) made the assumption that these disturbances need not be modelled individually, but instead their effects only had to be considered. They assumed that the external disturbances entered the control domain through the inflow. They introduced a new disturbance model that assumes stochastic (random) excitation of the dominant perturbation modes in the flow that contribute to transition. Using this approach, specific perturbation modes included in the control design can be selectively targeted. In this way, the most dominant modes present in the actual boundary layer that contribute to transition can be precisely controlled.

Numerically, they showed that a reduction in perturbation wall-shear stress of 96% was possible using this model. The next natural step is thus to validate the designed controller in a wind-runnel setting. This study thus places itself in the context of experimental validation of the LQG based model developed by Tol et al. (2017). The following sections explain the control logic as well as the structure of the controller ,followed by the method of implementation in a wind-tunnel setting.

4.4.1. Structure of the Controller

In control theory, the standard state-space representation of a discrete time-invariant linear system can be written as (Brogan (1982)):

$$\begin{aligned} \dot{u}(k+1) &= Au(k) + B\phi(k) \\ y(k) &= Cu(k) + D\phi(k) \end{aligned} \tag{4.16}$$

For the controller as designed by Tol et al. (2017), u is the full-order state vector(consisting of flow perturbation velocity and wall-actuation velocity) , y is called the output-vector, A is the system matrix i.e. it describes the governing equation of the system (reduced discretized linearized 2D linear Navier-Stokes equation in this case), B is the input matrix, i.e. how the input affects the system (in this case the discretized representation of the body-forces, using the data from Kotsonis et al.(2011)), C is the output matrix (relating the perturbation field to the measured quantity, y) and D is the feed-forward matrix(=0 since there is no feedthrough). The resulting system of equations can thus be written as in Equation 4.17. Here p_1 is the upstream sensor signal and w is the disturbance vector (w_d, w_n) which consists of external state disturbances and measurement sensor noise.

$$\begin{aligned} \dot{u}(k+1) &= Au(k) + B\phi(k) + B_d w(k) \\ p_1(k) &= Cu(k) + Dw(k) \end{aligned} \tag{4.17}$$

The controller (Compensator) is comprised of two parts - the State Estimator or Kalman filter which constructs a low-dimensional approximation of the flow-field using the upstream pressure measurements and the State Feedback which determines the output signal,ϕ from the estimated state and is fed to the plasma actuator.
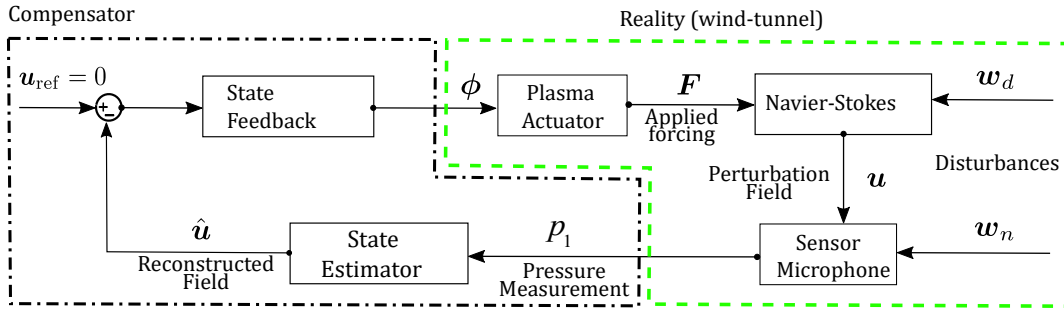
Figure 4.3: Design of the controller and its relation to the Experimental Setup

State Estimator

Tol et al. (2017) developed the control and estimation of linear instabilities in wall-bounded shear-flows using a multivariate spline state-space representation of the flow. In their design of the controller, reduced order models(ROM) of the matrices in Equation 4.17 are computed **A,B,C** and **D**. If $\hat{u}(k)$ is the reduced estimated state, p_1 the upstream pressure measurements, **L** the Kalman-gain matrix and $\phi(k)$ the output signal, the discrete-time implementation of the output feedback controller is

$$\hat{u}(k+1) = \mathbf{A}\hat{u}(k) + \mathbf{B}\phi(k) + \mathbf{L}(p_1(k) - \mathbf{C}\hat{u}(k)) \tag{4.18}$$

The Kalman-filter is based on the following principle. In order to be able to estimate an unknown variable, it combines the data obtained using a physical model with that from measurement data (which may contain statistical noise). These estimates tend to be more accurate, than if only one source was used. Firstly, an estimate of the state is made using the physical model (Reduced Linearized NS equations, which is in matrix **A**). Then the estimated values are compared to those measured from the real-time measurements in the experiment and the error is calculated. The Kalman-filter as designed in Equation 4.18 thus seeks to minimize the covariance of this estimation error in the presence of disturbances w_d and w_n, which are the external disturbances (such as freestream turbulence) and sensor noise, respectively. The estimated perturbation fields are subsequently used within a feedback control law to stabilize the perturbations.

State Feedback

The goal of the state-feedback is to minimize the wall-shear stress (thus minimizing the drag caused by the TS waves). If **F** is the feedback gain matrix, then the output control signal is given as

$$\phi(k) = -\mathbf{F}\hat{u}(k) \tag{4.19}$$

Here the unsteady modulation, $\phi(k)$ is used to compute the voltage signal which is used to drive the plasma actuator as $V_{app} = 0.5\left(V_{pp} + \phi\right)\sin(2\pi f_{ac}t)$. As explained in Secion 3.2.4, the V_{pp} is the base-voltage, giving a constant forcing which provides a mean flow-stabilization. The modulated signal is then added to the base signal and multiplied with an appropriate carrier frequency.

In order to take into account errors in controller design/body force estimations and to allow a certain "fine-tuning" of the system, an online tuning factor k allows us to adjust the magnitude of the control signal. This is multiplied with the output-signal, leading to the final output voltage signal as given in Equation 4.20, where $\tilde{\phi}$ is the controller output.

$$V_{app} = \frac{1}{2}\left(V_{pp} + k\tilde{\phi}\right)\sin(2\pi f_{ac}t) \tag{4.20}$$

4.4.2. Implementation in Wind-Tunnel

Figure 4.4 shows a schematic of the physical implementation of the controller along the flat-plate. The sensor microphone placed at x=0.3 m picks up the pressure signals ,p_1 which along with the reduced discretized matrices (**A** and **B**) and the Kalman gain, **L** compute the estimated state vector $\hat{u}(k+1)$ according to Equation 4.18. The state estimator reconstructs the entire field and multiplies it with the controller gain, **F** to give the modulated frequency signal ϕ. This happens according to Equation 4.19.
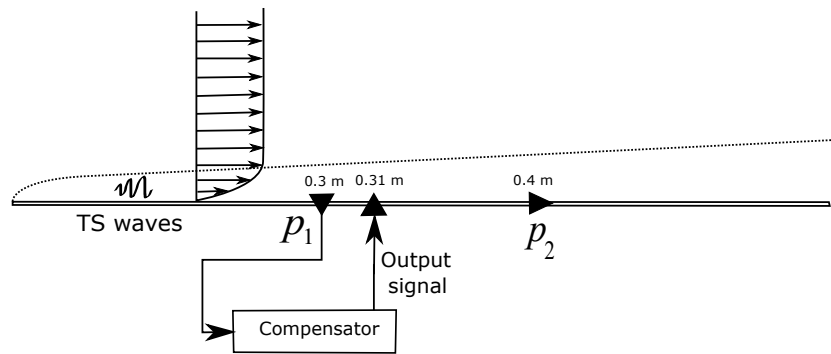
Figure 4.4: Schematic of the Feed-forward system(LQG controller)

For the open loop case (control without modulation), the magnitude of the control signal is merely the chosen peak-to-peak voltage V_{pp} in kV operating at a carrier frequency of 2kHz. This is the base frequency using which is required to generate plasma in the actuator. For the closed loop case (control with modulation), the modulated signal ϕ obtained from the state feedback is added to the base amplitude (V_{pp}) and multiplied with the carrier frequency as given in Equation 4.20 to give the total voltage signal, V_{app}.

This signal then is used to run the actuator present at x=0.31m. The downstream microphone (at x=400mm) is uncontrolled and is simply used to measure the pressure signals downstream of the actuator, which is then used to investigate the controller performance. Section 5.5 explains the test set-up used to execute this in detail.

Experimental Setup

Tollmien-Schlichting waves amplify very quickly in the presence of an adverse pressure gradient. It is therefore important to identify the location, magnitude, range of frequencies and the spread of these waves before control can be applied. Two experimental campaigns were therefore decided to be carried out. The first was done to identify and characterise the TS waves. The second campaign was employed to control the TS waves using the designed controller with the help of DBD plasma actuators.

This chapter describes the test setup used for both the experimental campaigns. Sections 5.1 and 5.2 describe the Test Section and its components viz. the flat plate, pressure tabs and microphones. Section 5.3 describes the properties of the actuator. Section 5.4 describes the setup of the flow quantification system : low-speed planar Particle Image Velocimetry. Section 5.5 describes the system setup employed for diagnostics and control. Lastly, Section 5.6 describes the test cases carried out for both experimental campaigns.

5.1. Overview of Test Setup

The experiments were carried out at the Anechoic Vertical Tunnel (AVT) located in the Low Speed Laboratory at TU Delft. One of the benefits of using this wind tunnel is the acoustic damping offered by the walls, which serve to minimize both external noises and internal reverberations. The exit section of the wind tunnel is circular with a diameter of 600mm. Velocities in the wind tunnel can be varied from 0 to 40 m/s with a maximum turbulence intensity of 0.02%. Figure 5.5 shows the test section used.
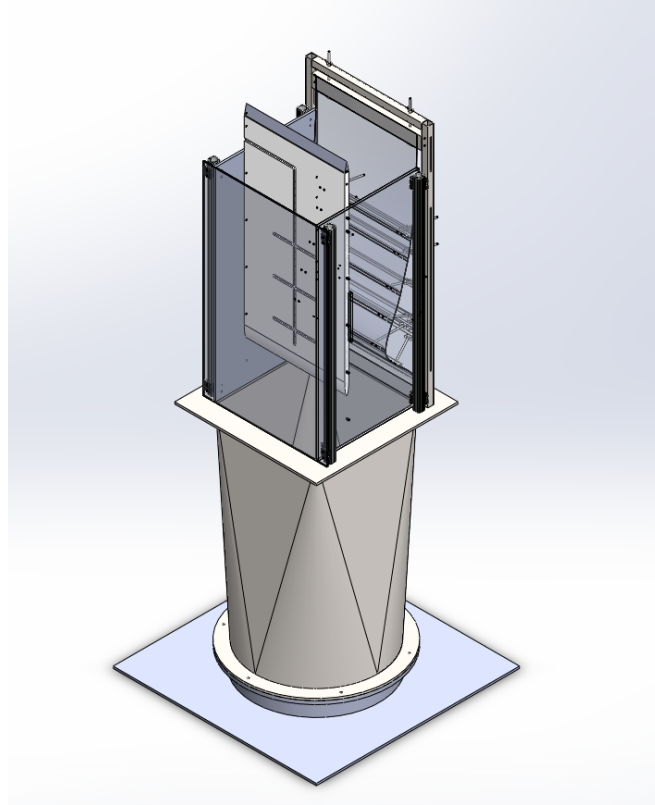
Figure 5.1: 3D CAD model of the test section and nozzle

The entire test section rests on a 'nozzle' which is used to convert the shape of the circular exit of 600 mm diameter to a square exit hole of 500 mm x 500mm. This is done to provide a uniform flow along the test section. The air enters the test section from the bottom and flows in the area between the flat plate and the flexible wall. The PIV laser was installed on the roof of the wind tunnel and shoots vertically downwards (see Figure 5.2b) . The flow speed is controlled using an external trigger. With the help of a pitot-static tube, attached just upstream of the flat plate, one can measure the freestream velocity,U_∞. The pitot static tube measures the difference in total and static pressure $(p_t - p_s)$ directly, which is equal to the dynamic pressure,q as

$$p_t - p_s = \frac{1}{2}\rho U_\infty^2 \tag{5.1}$$

Knowing the value of the local temperature and the barometric pressure, the system can calculate the local air density which is then used to calculate the free-stream velocity. A digital pressure gauge (Mensor 2400) was used for this purpose.

5.2. Test Section

The entire test-section is about 50 x 50 x 100 cm. The main components are a cuboidal case made of plexiglass (open at the top and bottom) which is attached on top of the 'nozzle' from the wind tunnel. This allows the air to flow smoothly (with minor boundary layers, of course) along the walls of the tunnels. About 150 mm from the back wall, is the main flat plate over which the flow in question is analysed (See Figure 5.2)

(a) Schematic view (not to scale)   (b) Setup of test section
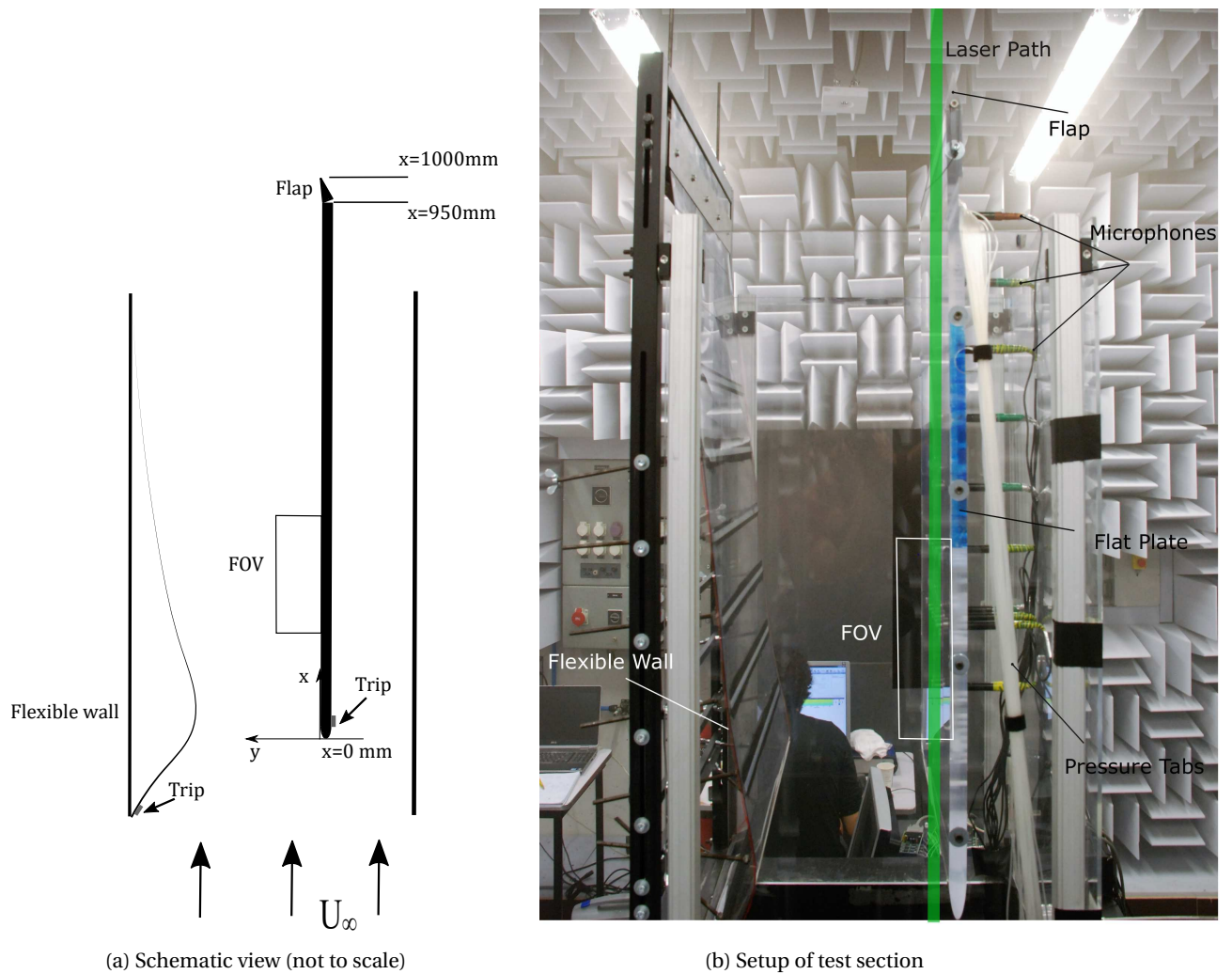
Figure 5.2: Schematic and actual test sections (side view)for the Experiment. The green line in (b) represents the path of the laser light for PIV

5.2.1. Flat Plate and Flexible Wall

A 950 mm x 450 mm x 20 mm flat plate made of plexiglass is used. The leading edge is super-elliptical in order to ensure a laminar boundary layer over the surface (Lin et al.(1992)). There is also a flap of length 50mm attached at the end of the trailing edge of the flat-plate, the movement of which controls the stagnation point. Two trip wires are used at two locations as shown in Figure 5.2. Their main purpose is to avoid a variable transition location which would be caused if there was no trip-wire. By having a trip wire, a turbulent boundary layer is maintained on both the flexible wall and the back side of the flat plate preventing any additional pressure inconsistencies due to changing flow regimes. Furthermore, the back side of the flat plate has the microphones (which may be prone to leakage) and so the lesser the interference due to changing flow properties in the back side, the more reliable the readings.

The flexible wall is used to control the slope of the adverse pressure gradient along the flat plate. By loosening and tightening the screws and the rods on the back of the flexible wall, its shape can be adjusted. During the first experimental campaign, it was observed that if the leading edge of the flat plate coincided with the leading edge of the flexible wall, there was a favourable followed by an adverse pressure gradient. This meant that transition was more likely to occur further downstream, outside our region of interest. In order to combat this, it was decided to move the leading edge of the flat plate to (roughly) the location of the maximum displacement of the flexible wall. This means that the region of interest lies somewhere between 200-400mm from the leading edge (at x=0 mm)

The FOV captured by the Low Speed Camera is as follows. For the first experimental campaign, clean TS waves were observed between microphones 1,2 and 3. In order to capture a good resolution of TS waves, it

was decided to use a field of view of 130 mmx 20 mm. The FOV starts at 285mm (the leading edge of the plate is the origin).This was focused on two microphones at a time – the first test on the region around microphones 1 (x=200 mm) and 2 (x=300mm), and the second test on the region around microphones 2 (x=200 mm) and 3 (x=300mm). See Section 5.4 for the exact values of both Field-of-Views.

5.2.2. Static Pressure Holes

Pressure tabs are used to measure the static pressure along the flat plate. They are located along the centerline (designated by small '+' symbols in Figure 5.3). Each of these tabs is connected to a module (which has a certain number of sensors) and is in turn recorded using a LabView interface. The sensors used are Honeywell TruStability ® Pressure Sensors (HSC Series - High Accuracy) with a digital output. They have a total range of ±160Pa with a total error of $\pm1.75\%$ of the total pressure range (or ±5.6 Pa, after removing sensor-bias) [2]. The system records the local pressure in the tube. In order to remove the sensor-bias (DC component for each sensor), the zero-error (measurement when flow velocity is zero) was measured before each run. This was then subtracted from the final measurements.

The first pressure tab is at a distance of 100 mm from the leading edge and ends at a distance of 790 mm with each tab at an interval of 30 mm. There are also two spanwise arms containing four equidistant pressure tabs at x= 160,340 and 520mm. It is important to note that only the pressure tabs of the centerline are used to calculate the value of the C_p along the plate. The ones in the branches are merely to check the spanwise variation of the pressure. They were found to be similar along these two rows, and the flow can be considered 2 dimensional in our region of interest.

The pressure readings are taken with a sampling frequency of 2000Hz for a duration of 10 seconds.
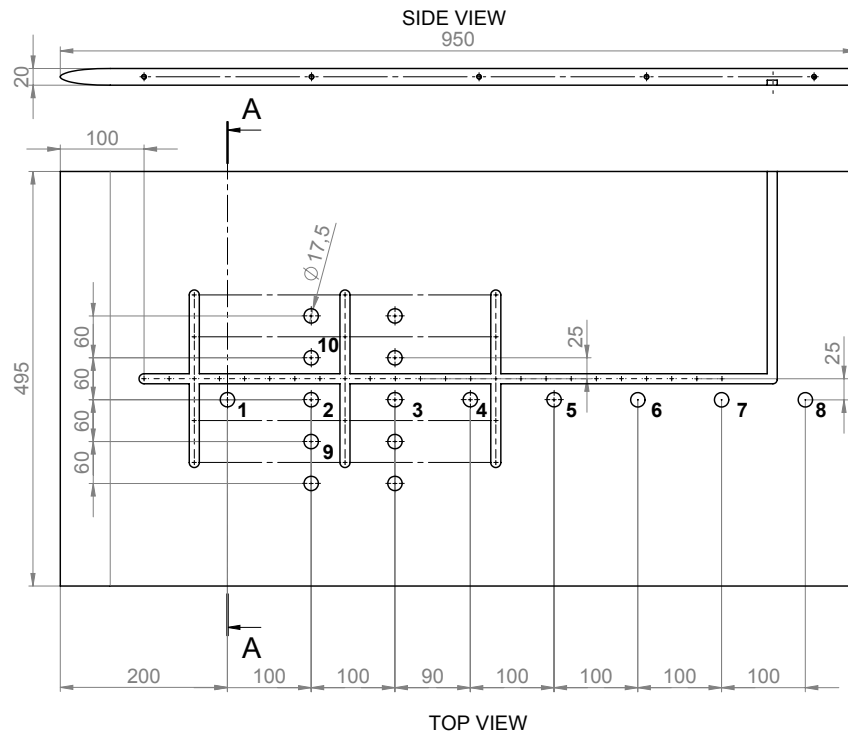
Figure 5.3: Top and Side View of the flat plate with the position of the Pressure-tabs('+' symbols along the centerline) and Microphones (in bold). All lengths are in mm.

Static Pressure Measurements

The static pressure measurements were taken at a sampling frequency of 2000Hz with a total measurement time of 10 seconds. Since the velocity is fairly low, the flow can be assumed to be incompressible and the C_p related as follows

---

[2]Datasheet: TruStability Board Mount Pressure Sensors HSC Series—High Accuracy, Honeywell International Inc., MN, USA - sensing.honeywell.com/honeywell-sensing-trustability-hsc-series-high-accuracy-board-mount-pressure-sensors-50099148-a-en.pdf

$$C_p = \frac{p - p_\infty}{\frac{1}{2}\rho U_\infty^2} \tag{5.2}$$

The term $(p - p_\infty)$ in the numerator is directly measured by the modules and the LabView system while the denominator is the free-stream dynamic pressure, which is measured by the digital pressure gauge (Mensor). It is thus possible to obtain the C_p values for the centerline along the flat plate. As mentioned earlier, the 2 dimensionality of the flow was checked by observing the spanwise variation of the pressure. Readings were performed for free-stream velocities of U_∞=6.2, 6.6, 7, 9, 9.4 and 9.8 m/s for TS wave characterization.

5.2.3. Pressure-Fluctuation Holes

In order to capture the pressure fluctuations within the flow, it is important to choose microphones sensitive enough to pick up the range of amplitudes of fluctuations that are typical of Tollmien-Schlichting waves for the given velocities. Prior studies using Linear Stability Analysis (performed by Louis Kokee, BSc. student) and literature (Sturzebecher and Nitsche(2003), Grundmann and Tropea(2008))showed that for a velocity of about 10 m/s over a flat plate , the range of frequencies was around 150-250 Hz. The range of amplitudes of these waves was around 90-100 dB(1-2 Pa). In order to capture the range of frequencies and amplitudes well, 10 microphones were attached at the given locations on the flat plate.

Microphones 1 to 5 in Figure 5.3 are Linear-X M53 microphones with a corrected frequency response of ±1dB with a range of 10Hz-40kHz,making them ideal for picking up TS frequencies since they are well within this range. The acoustic sensitivity is 140mV/94dBspl for this series [3]. This means that even for lower-SPL values, the voltage-signal will be readable, making them quite sensitive.

Microphones 6 to 10 are Linear-X M51 microphones with a response of also ±1dB within a range of 10Hz-40kHz. However, the acoustic sensitivity is 12mV/94dBspl [4], making them less sensitive compared to the M53's. The reason for putting the M53 microphones upstream and the M51 microphones downstream is because the TS waves are very weak in their linear stages and therefore can be picked up better by the more sensitive M53 microphones. The M51 microphones will still be able to pick up the location of transition and the turbulent fluctuations.

Microphone no. (streamwise)	Type	Distance from Leading Edge (mm)
1	M53	200
2	M53	300
3	M53	400
4	M53	490
5	M53	590
6	M51	690
7	M51	790
8	M51	890
Microphone no. (spanwise)	Type	Distance from Centerline (mm)
9	M51	90
10	M51	-30

Table 5.1: Positions of all the Microphones used for Experiment 1. For Experiment 2, only the first four M53 microphones are used

All microphones were attached through the back of the flat plate with the help of a mechanism as shown in Figure 6.2b.

---

[3]M53 Measurement Microphone, Linear X Systems, USA -http://www.physical-lab.com/images/pdf/M53_Mic_Brochure.pdf
[4]M51 Measurement Microphone, Linear X Systems, USA -http://www.physical-lab.com/images/pdf/M51_Mic_Brochure.pdf

(a) Dimensions of the pocket for the microphone
alongside that of the pressure-tab slot

(b) Attachment of microphone to plate
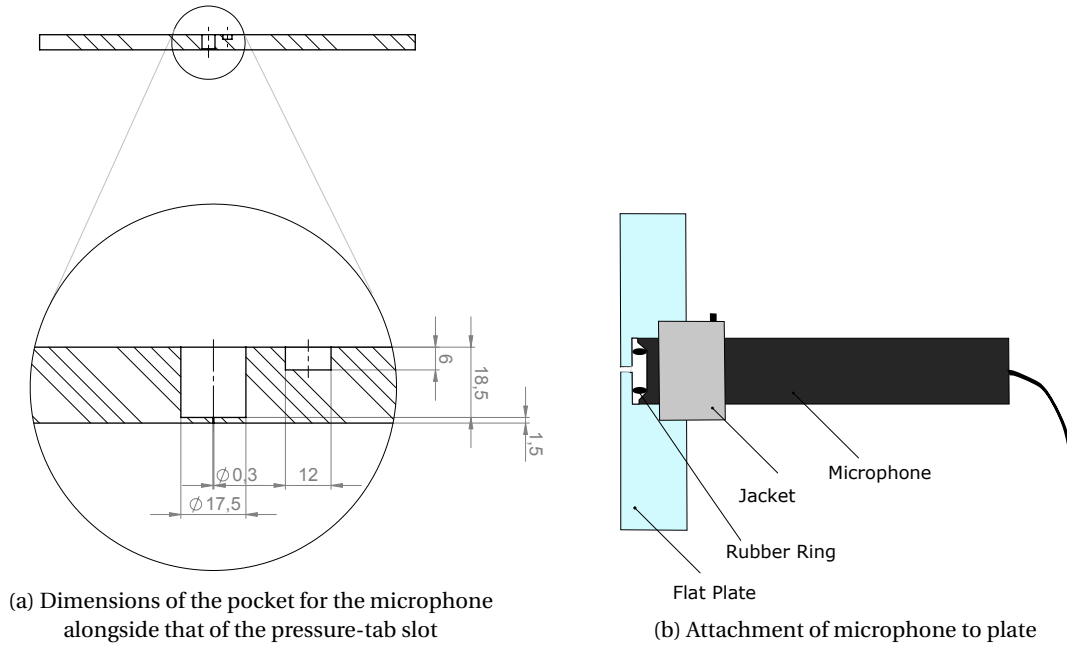
Figure 5.4: The slot for the microphone - (a)Dimensions (in mm) and (b)Schematic of the support (not to scale)

A metallic jacket held the microphone firmly in place and could be tightened with a small screw. The waves enter the microphone through a small 0.3 mm orifice on the front side of the plate (left side in Figure 6.2b). In order to make sure that there is no pressure leakage, a small rubber ring is used to make the system air tight. It should be noted that due to this small region, there is a possibility of resonant frequencies being generated. This will be elaborated in the next section.

The acquisition system was equipped with LabView which allowed a real-time viewing of the pressure measurements. A zero run was taken before every test matrix to account for any existing pressure, change in shape of the tubes or if there was any interference due to blockage etc.This was later subtracted from the measured data.

Microphone Calibration

Every microphone has its own internal calibration. Depending on how it is manufactured (even for the same series) and its usage over time, these values can somewhat change. Thus the values of the measured pressure signals might be different from the actual local pressures, and therefore cannot be trusted right away. Especially since the values of TS wave pressures are in the range of 1 Pa. In order to solve this, all microphones must be calibrated independently.

This is done with the help of a PistonPhone (GRAS Type 42AA) which gives a constant signal of frequency 250Hz and an SPL of 114 dB(or 10 Pascal) [5]. This was held in front of each microphone and measured for 10 seconds at a sampling frequency of 30kHz. It was then filtered using a Butterworth filter of order 4, the lower band pass frequency being 200 Hz and upper band pass frequency 300 Hz. This is done to remove any external noise from the signal due to the background etc. The RMS for each individual signal was then taken and divided by 10 pascals, in order to obtain the calibration factor for each microphone. Thus, these factors need to be multiplied with the final signals at all times during the measurements.

Another issue that might arise is the possibility of cavity resonance. This resonance frequency could interfere with the TS frequency , causing beats. The volume of the cavity is inversely proportional to the frequency as given by the relation in 5.3. Since the cavity in this case is minuscule (d=0.3mm), this could incur a penalty.

$$f_r = \frac{c}{2\pi}\sqrt{\frac{A}{Vl}} \tag{5.3}$$

where c is the speed of sound,A is the cross section of the cavity ,V is the total volume of the cavity and l is the length of the opening port. Calculation for this case shows a cavity frequency of 2.72kHz, much higher

---

[5]Instruction Manual- Pistonphone Type 42AA, G.R.A.S Sound and Vibration, Denmark- www.gras.dk/files/m/a/man_42AA_42AA-S1.pdf

than our desired range of frequencies. Even beats, if produced, would be very high and thus should not interfere with the measured TS values.

5.3. Actuator Properties

The actuator is the main forcing element that will produce body-forces within the flow and alter the flow dynamics. It is thus very important to choose the type, size, thickness and position of the actuator that will be used to affect flow perturbations. Furthermore, the choice of plasma actuator also depended on existing characterization of its body forces. Since the designed controller required an existing measure of the body forces (which is used for evaluating matrix B in the controller, Section 4.4.1), it was decided to used the familiar Copper-Kapton DBD plasma actuator. The data obtained from Kotsonis et al.(2011) was used in this regard.
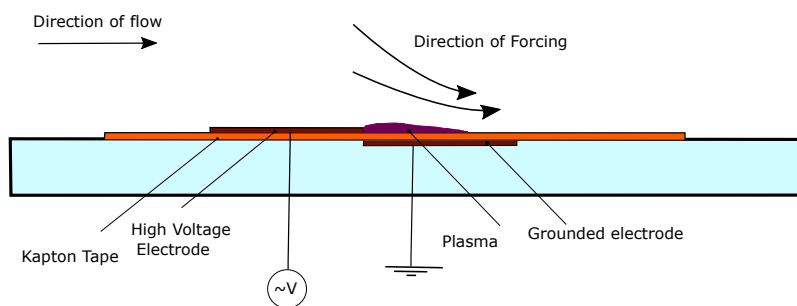
Figure 5.5: Schematic of the actuator cross-section used to generate a uni-directional body forcing

The dielectric is a polyimide called Kapton and has a thickness of $50\mu m$. Two layers were used. The covered electrode made of copper has a thickness of 30 μm, and a width of 10mm. It is grounded. The exposed electrode is connected to the High-Voltage Amplifier and has a thickness of 4mm. The gap between the two electrodes is kept almost minimal and this location (x=0.31m) is taken as the position of actuation for all the experiments. Table 5.2 summarizes these physical dimensions.

Section	Material	Thickness (μm)	Width(mm)
High Voltage Electrode	Copper Tape	30	4
Grounded Electrode	Copper Tape	30	10
Dielectric	Kapton	100	45

Table 5.2: Dimensions of components used to manuacture the plasma actuator

Prior tests were carried out to check the physical effect of the thickness of the plasma actuator on the TS waves. These were found to be almost non-existent. Also, all the tests (and results presented herein) are those corresponding to a single actuator. This was done to avoid errors in manufacturing and/or placement as much as possible.
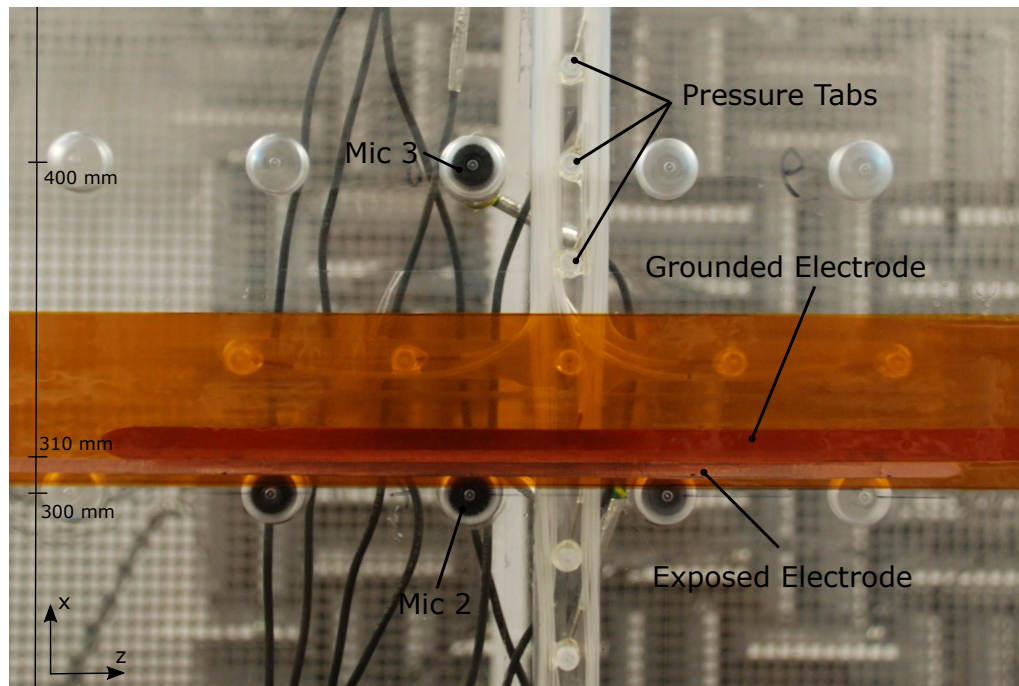
Figure 5.6: Plasma actuator at 10 mm from sensor microphone, Mic 2(at x=300mm) and 90 mm from the downstream microphone, Mic 3(x=400mm). The two side microphones are not used. The flow direction is from down to up.

In order to generate plasma, it was decided that a nominal frequency of 2kHz would be used. This will act as the carrier frequency over which the modulation generated from the controller will be added. $8kV_{pp}$ to $12kV_{pp}$ was the voltage amplitude which is sufficient to generate a stable discharge.

5.4. Particle Image Velocimetry

This section presents the settings of the sub-systems that were required in order to carry out low-speed planar Particle Image Velocimetry (PIV).The reader is referred to Section 4.2 and (Scarano (2013)) for a full description of the working principle of PIV.

Setup

Through real-time microphone readings , clean TS waves were observed between microphones 1, 2 and 3. PSD Analysis from the microphones showed that the range of wavelengths of these TS waves were on the order of 2-4 cm. Thus in order to capture a few TS waves, for the given range of velocities, the following parameters were chosen for PIV

System Parameter	Value	Unit
Aperture number, f#	5.6	-
Field of View	130x20	mm
Sensor Size	4872x3248	px
Pixel size	7.4x7.4	μm
Acquisition Frequency	2.2	Hz
Number of Frames	500	-
Magnification Factor	0.277	-

Table 5.3: Parameters of the PIV Setup

The camera used is the LaVision Imager LX Pro with a resolution of 16 Megapixels (4872x3248 pixels). This results in a magnification factor of 0.277

Flow seeding is performed using the SAFEX Fog Generator that utilises a water-glycol mixture to create particles of size $1\mu m$. These are fed into the flow of the wind tunnel and form the tracer particles which

are illuminated by a laser. The seeding concentration is usually kept between 10^9 and 10^{12} particles per m^3 (Scarano (2013)) and are considered to not afect the flow properties.

The Laser utilized is a double-head pulsed laser. The model is the Quantel Evergreen 200, an Nd:YAG laser which shoots a beam of green light (wavelength 532 nm),with a power of 200mJ per pulse. Two pulses are shot with a time interval Δt, which is calculated based on the velocity of the flow. The light is focused through a simple setup of lenses which allows the beam to be sharp and focused in the plane of view, and at the position on the flat plate. As shown in Figure 5.2, the laser was mounted in a hatch above the wind tunnel, from which it was fired downward.

Image Processing

As described in Section 4.2.2, post processing of the image files is done using Davis v 8.4. In order to quantify the velocity vectors in the field-of-view, a multi-pass filter was employed. The first pass used was 48x48 pixels, to get a first estimation of the displacement vectors. An overlap of 75% was taken for the windows. Subsequently, to fine tune the vectors window sizes of 32 x 32 and 16 x 16 were performed, respectively both with window overlaps of 75%. The last pass was performed twice.

Once the displacement vector is known, the software automatically calculates the velocity by dividing by the corresponding time-difference (Δt), multiplying by the pixel-size and dividing by the magnification to obtain the instantaneous velocity. This was performed for all 500 image-pairs, leading to 500 velocity-vector snapshots.

Vector Paramaters	Window Size (px)	Overlap (%)	No. of passes
First Pass	48x48	75	1
Second Pass	32x32	75	1
Third Pass	16x16	75	2

Table 5.4: Vector Parameters used in Davis v8.4 for the computation of the velocity vectors

Once the individual instantaneous velocity fields were obtained using Davis , they were converted into Matlab-readable formats, using which all the field and fluctuation statistics (RMS, Reynolds stress, Turbulent Kinetic Energy) were computed. An error analysis as described in Section 4.2.4 was also carried out.

5.5. System Setup for Control

For implementation of the controller as described in Section 4.4.1,can be summed up as threefold: Diagnostics, Estimation and Control.

For acquisition of data from the microphones the model NI cDAQ-9174 was used as the data acquisition system. The first module, NI 9215 ,connected the microphones to System 1 equipped with LabView is used for diagnostics. Within this system, a VI was created that could read the pressure signals, compute the FFT as well as RMS in real time. This allowed a dynamic adjustment of the settings and calibration of the microphones with ease.

A Field-Programmable Gate Array (FPGA) developed by National Instruments, called the CompactRio Real time controller (NI cRIO-9022) was used to execute the estimation and control, shown by System 2 in Figure 5.7. The control logic essentially consists of three-parallel running loops within a LabView framework. The first loop consists of a bandpass filter (50-800 Hz) which serves to filter the upstream microphone signal from the DC component, the low frequency background noise and possible high-frequency plasma actuator noise. The sampling frequency of this loop is 100 kHz. The second loop consists of the Compensator as described in Section 4.4.1 which provides the modulated signal ϕ. This loop executes at 20kHz. Here an online tuning factor,k is multiplied with the output signal ($\phi = k\tilde{\phi}$) to account for small modelling inaccuracies. The third and final loop executes at 100kHz and generates the final output signal (modulated + carrier) which is fed directly into the HV Amplifier, which is then used to run the plasma actuator.
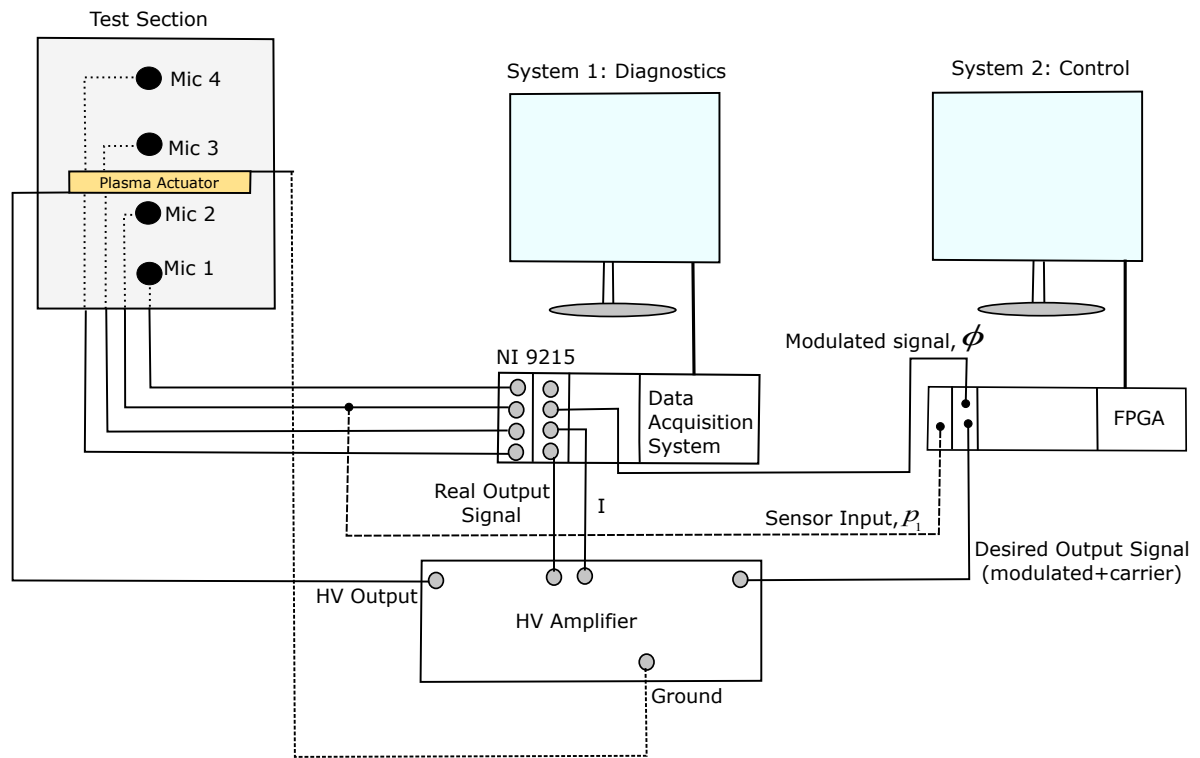
Figure 5.7: Schematic of the System Setup for Implementation of Control

It must be noted that the real output signal (signal outputted from the HV Amplifier) may not exactly be the same as the desired output signal from the FPGA. In fact is may be a bit less due to the internal mechanisms of the amplifier such as its resistance. Hence to measure the actual output signal, another connection is made to the Data-acquisition system. The current supplied to the plasma actuator (I) is also recorded.

5.6. Test Matrices

The following test-matrices were employed in the two experimental campaigns. The eventual goal is to study the feasibility of the LQG contoller on the growing TS waves. The first campaign thus involved identifying and characterizing TS waves over the flat plate. Based on these results, few test cases were selected that demonstrated the cleanest and most well-spread TS waves over two microphones.

The second campaign involved trying to control the TS waves at the design condition (U_∞=9.4 m/s, decided from First Campaign) for three base-voltages $8kV_{pp}$,$9kV_{pp}$ and $10kV_{pp}$. In order to measure the robustness and actuator performance, tests were also done for off-design conditions.

5.6.1. TS Wave Characterization

The purpose of the first campaign was to identify and characterize the TS waves – their frequencies, amplitudes, location and spread over the flat plate and thus the PIV field of View.

This was done as follows. First, a velocity sweep was carried out. The objective was to be able to identify TS waves across at least two of the M53 microphones. The velocities chosen were U_∞=5m/s to 11.6 m/s with an increment of 0.2 m/s. C_p and microphone data were measured for all. From these velocities, a set of six were selected that showed clear TS waves over at least two of the microphones. This is important since, these will be the chosen cases where one should be able to observe 1)the upstream signal and 2)the effects of control on the downstream microphones . The velocities U_∞=6.2,6.4,7,9,9.4 and 9.8 were selected as the test velocities.

For Particle Image Velocimetry, two regions of interest were chosen. 1)The Upstream Region, between microphones 2 and 3. The field of View begins at x=185mm and ends at x=315mm and 2)The Downstream Region, between microphones 3 and 4 .The field of view here starts at x=285mm and ends at x=415mm.

The separation between the pulses is determined based on the movement of particles in the FOV. Scarano (2013) states that for conventional PIV experiments, the maximum measured velocity should not exceed 10

pixels. Hence the pulse separation chosen decreases with the increasing velocity.

The test matrix for both regions is shown below:

Test Velocities (m/s)	Pulse separation, $\Delta t(\mu s)$	Sampling Frequency (Hz)	No of images
6.2	40	2.2	500
6.6	37	2.2	500
7	36	2.2	500
9	28	2.2	500
9.4	26	2.2	500
9.8	25	2.2	500

Table 5.5: PIV parameters for the both Upstream and Downstream Region

Sub-System	Sampling frequency(kHz)	Duration(s)
Microphone	30	60
Pressure Tabs	2	10

Table 5.6: Microphone (M53) and Pressure Tab parameters

5.6.2. Control Implementation

The second experimental campaign was carried out with the aim of investigating the effect of the developed LQG controller (implemented using LabView) on the growing Tollmien-Schlichting waves. The test section used for this part of the campaign is exactly the same as the first, only this time there is the presence of a Plasma actuator at x=310 mm, between Microphones 3 and 4 as seen in Figure 5.6.

For this study, the C_p was first measured. This information was then used to obtain the inviscid velocity which is then used to obtain the base boundary layer flow required for the linearization. The controller is subsequently derived from the linearized Navier-Stokes equations by Tol et al. (2017). This was then executed using a Field-Programmable Gate Array (FPGA) embedded in a CompactRIO device by National Instruments. Labview allowed the real-time controlling of the output-voltage signal from the HV generator to the plasma actuator, which in turn caused a variation in the forcing produced by the actuator. Due to experimental limitations, no PIV was performed for this part of the campaign. Only readings from the pressure tabs and microphones were carried out.

The microphone sampling frequency is 30 kHz and a sampling time of 20 seconds is chosen. A online tuning gain was incorporated into the script to allow a real time adjustment of the amplitude of the output signal (ϕ). This is done to take into account errors that may have crept in the designing and modelling of the controller. Furthermore, prior simulations showed that the actuator performed stronger than that assumed in the control design. Since a more aggressive control can actually promote transition due to possible non-linear effects and control spillover (Balas(1978), this was mitigated by introducing an online tuning factor,k. This factor taken is to be 0.35 for all the measurements analysed in this thesis.

Parameter	Value	Unit
Sampling frequency (Microphone)	30	kHz
Duration of Sampling (Microphone)	20	s
Sampling frequency (Pressure Tab)	2	kHz
Duration of Sampling (Pressure Tab)	10	s

Table 5.7: Microphone(M53) and Pressure Tab parameters

The test matrix in Table 5.8 is used for executing the controller. A number of runs were performed for actuators at different distances from the upstream microphone. The test matrix for the most optimum performance was chosen (distance from upstream microphone =1cm).Although quite close to each other, it was verified that the plasma actuator does not electromagnetically interfere with the signal of the upstream microphones.

Condition	Velocity (m/s)	Voltage (kV_{pp})	Online tuning gain,k
Off-Design	7.8	8,9	0.35
	8.2	8,9	0.35
	8.6	8,9	0.35
	9	8,9	0.35
Design	9.4	8,9,10	0.25,0.3,0.4,0.45,0.5
Off-Design	9.8	8,9	0.35
	10.2	8,9	0.35
	10.6	8,9	0.35
	11.4	8,9	0.35
	11.8	8,9	0.35

Table 5.8: Test Matrix for executing the LQG controller

The above test matrix was performed for the uncontrolled (no forcing), open loop(constant forcing) and closed loop case (LQG controlled). The online tuning gain k, is only utilized for the closed loop case.

6

Results

The results of this thesis are divided into two parts. The first part describes the results obtained from the first experimental campaign - the characterization of the Tollmien Schlichting waves and the second part discusses the control of these waves using the developed LQG controller.

Section 6.1 presents the results of the first experiment. It starts by analysing the static-pressure signals which are used to gain an idea of the C_p distribution, location of transition and the inviscid velocities (Section 6.1.1). Section 6.1.2 discusses the Power-Spectral Density of the pressure-fluctuations, the amplitudes of the TS wave frequencies as well as their growth. Section 6.1.3 presents the results of the low-speed Particle Image Velocimetry (PIV) to study the mean and fluctuations statistics (6.1.4). The results of the Proper-Orthogonal Decomposition (POD) are examined in Section 6.1.5.

Section 6.2 presents the results of the second experimental campaign : control using the Linear-Quadratic Gaussian (LQG) compensator. Section 6.2.2 investigates the performance of the controller at its nominal design conditions ($U_\infty = 9.4 m/s$) and Section 6.2.3 presents the results of the robustness study (performance at off-design conditions).

6.1. TS Wave Characterization

Before any type of measure to manipulate the boundary layer is taken, it is important to be able to characterise it and identify the instabilities present, their strength, location and spread. This section presents the results of the characterization of the boundary layer and the Tollmien-Schlichting waves therein. This includes the analysis of the signals from the pressure tabs (C_p), the Power Spectral Density(PSD) analysis of the microphone signals as well as the quantification of the mean flow and the boundary layer parameters using PIV. POD then gives a visualization of the most dominant energy modes present in the flow and allows the characterization of the size and shape of the TS waves.

It must be recognised that TS waves are not the only source of instability present in a flow. Others do exist (cross-flows, streaks etc.) and are also reasons for transition to occur and it may be better to call them 'flow perturbations'. However, for an unswept flat plate at a low Reynolds number ($6x10^5$ here), Tollmien-Schlichting waves are the most dominant. Hence from here on out in this analysis, TS waves will be used synonymously with flow-perturbations.

6.1.1. Analysis of Static Pressure Signals

It is important to have an idea of the gradient of pressure over the flat plate to be able to study the boundary layer. Since it is known that Tollmien-Schlichting waves form and grow in an adverse pressure gradient, the first step in their identification is to find a suitable shape of the flexible wall such that there is a suitable drop in the pressure. Adjusting the shape of the wall is sensitive. Too shallow and there is not enough adversity in pressure gradient to develop TS waves, too steep and a laminar separation bubble is formed. The ideal shape would be one that spreads out the TS waves over at least two microphones (so that they can be picked up by both and later be used as a sensor and receiver in control) while also not forming a separation bubble.

A measurement of the C_p also gives the location of the transition, which indicates when the flow has become turbulent. Beyond this transition point is outside our region of interest. Figure 6.1 shows the C_p spread over the flat plate for the range of selected velocities.
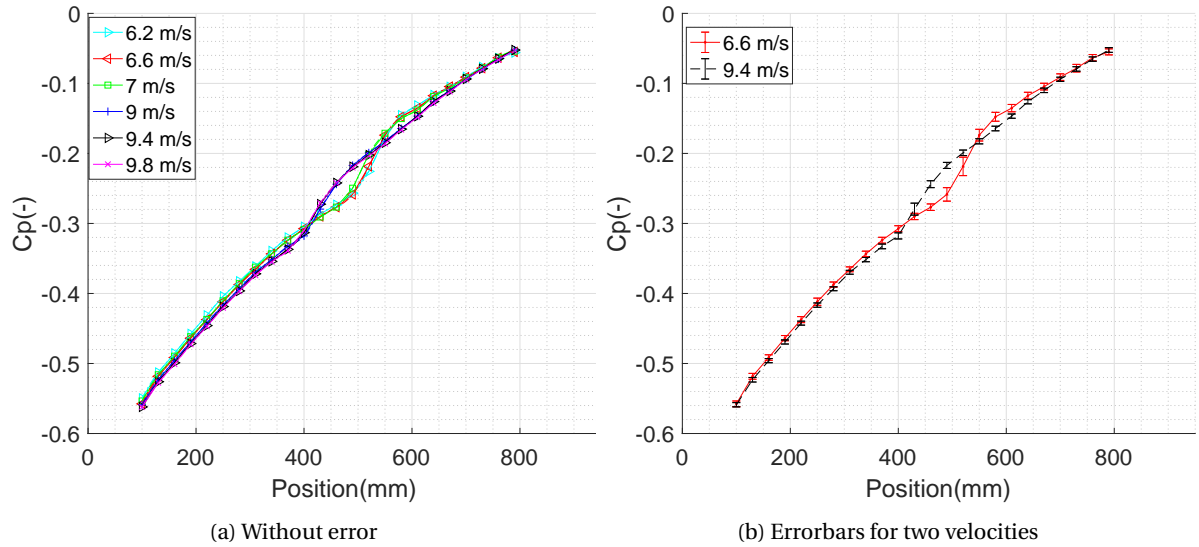
(a) Without error

(b) Errorbars for two velocities

Figure 6.1: Plots of C_p for different free-stream velocities along the flat plate (a)without and (b)with error

The first set involves lower free-stream velocities (U_∞=6.2,6.6 and 7 m/s) which show that transition occurs at around 550mm from the leading edge.The second set involves higher free-stream velocities U_∞=9, 9.4 and 9.8 m/s, which being faster, moves the transition location more upstream to around x=450mm. The bump in the curve, however, seems to be spread out and therefore isn't able to give a clear picture of the exact location of transition. One way to find a more precise location is to plot the gradient in the curve. A sudden jump in the slope will mean that transition has been achieved at that location.

The location of the transition can be further validated by plotting the amount of fluctuations (or standard deviation, σ) from the mean value for the C_p plots. Since transition is the point where the fluctuating component changes the most from the mean component, this should show up as a higher value of standard deviation compared to the laminar or turbulent regimes.

(a) Gradient of C_p
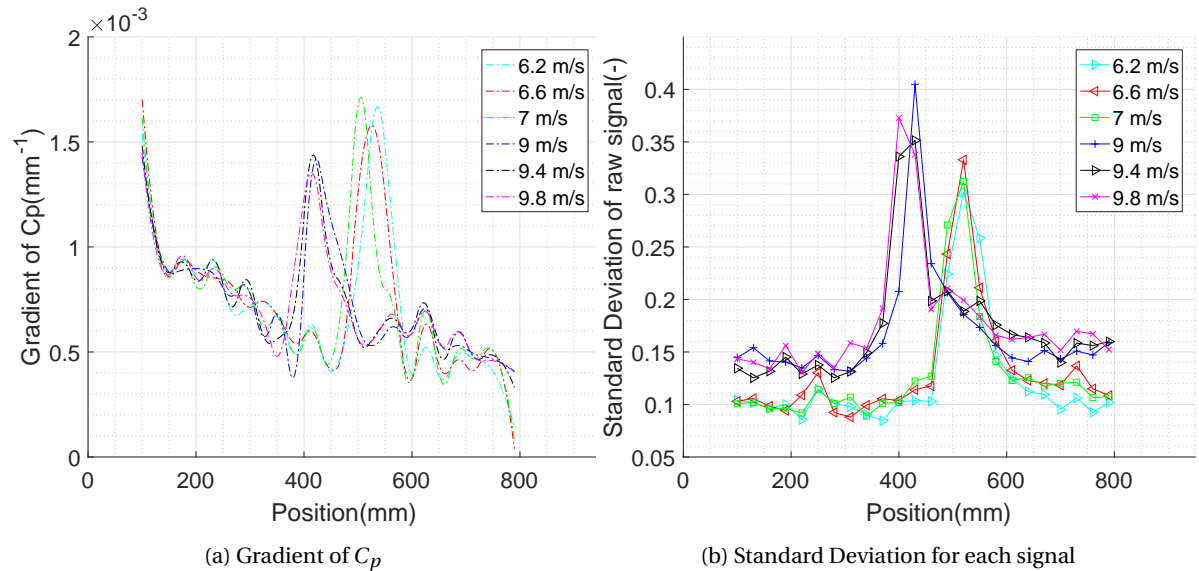
(b) Standard Deviation for each signal

Figure 6.2: Plots of gradient and standard deviation for different free-stream velocities (U_∞)

Observing both Figures in 6.2, it becomes clear that a more precise location of transition for the lower velocities (U_∞=6.2,6.4 and 7 m/s) is around x≈525mm and for the higher velocities (U_∞=9,9.4 and 9.8 m/s) it is around x≈420mm.

Inviscid Velocity

Evaluating the inviscid velocity along the flat plate serves two purposes. One, this can be used to validate the velocities in the far stream region using Particle Image Velocimetry, demonstrating an independent validation of both methods. Secondly, this information is used in designing the controller for the second phase of this thesis.

Figure 6.3 shows that the inviscid velocity is decreasing for all the cases, as it should. Also, the location of transition is visible as a tiny bump in the curves. This is so because since the location of the point of transition seems to act as a choke i.e. it effectively decreases the cross section through which the flow is flowing at that point, causing a minute increase in the inviscid velocity (seen as a bump) before decreasing again. Like before, this plot also shows that for the lower range of free-stream velocities, the transition point is around x=520 mm while for the higher velocities, it is around x=420 mm.
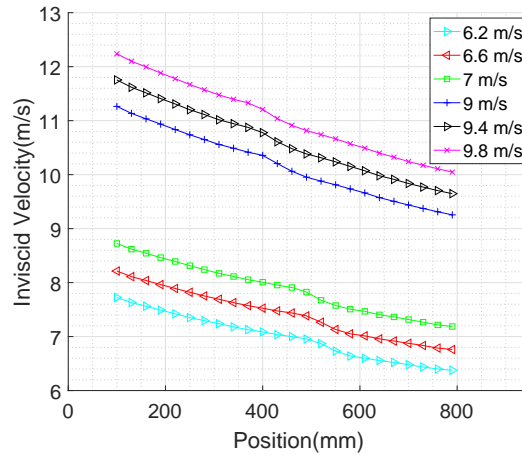

Figure 6.3: Inviscid velocity along the flat plate obtained from C_p-measurements for different free-stream velocities(U_∞)

6.1.2. Spectral Analysis of Microphone Data

The microphones used for measuring the packet of frequencies are M53 microphones from LinearX since these have the resolution to pick up the pressures and frequencies in the range that nominal Tollmien-Schlichting waves usually occur (1 Pa for free-stream velocities around 10 m/s and frequencies of 200-300 Hz, Sturzebecher and Nitsche(2003)). Figure 6.5 shows the filtered pressure signals (using a 4th order Butterworth filter between 10 and 10,000 Hz) along with the PSD plots for microphones 1 to 4.

The terms upstream and downstream merely refer to the fact that in the Upstream case, the Field of View for PIV was kept between microphones 2 (x=300 mm) and 3 (x=400 mm), while for the downstream case they were kept between 3 (x=400 mm) and 4 (x=490 mm). Before any of the runs, PSD plots of the zero runs were performed (U_∞ = 0 m/s) to check if there were frequencies due to any external disturbances in the signals. It was found that for both the Upstream and Downstream cases, a rogue frequency at 166 Hz of magnitude 100dB seems to seep in. This was probably due to external noise, which at the time of the experiment could not be identified.
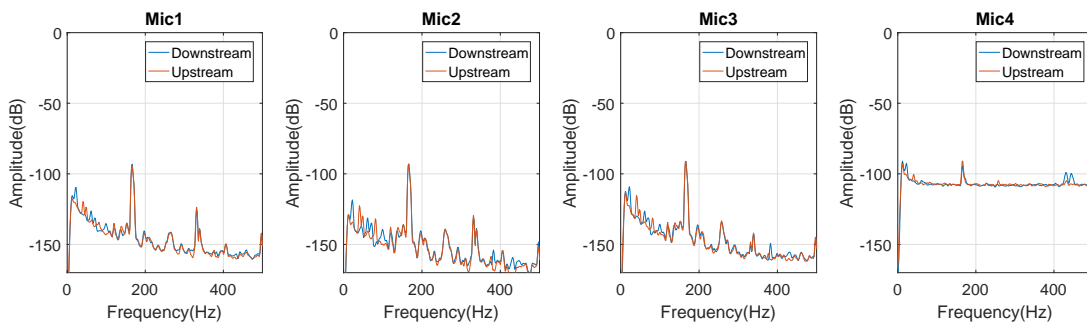
Figure 6.4: PSD of pressure signals from the first four microphones (at x=200,300,400 and 490 mm respectively) for U_∞= 0m/s
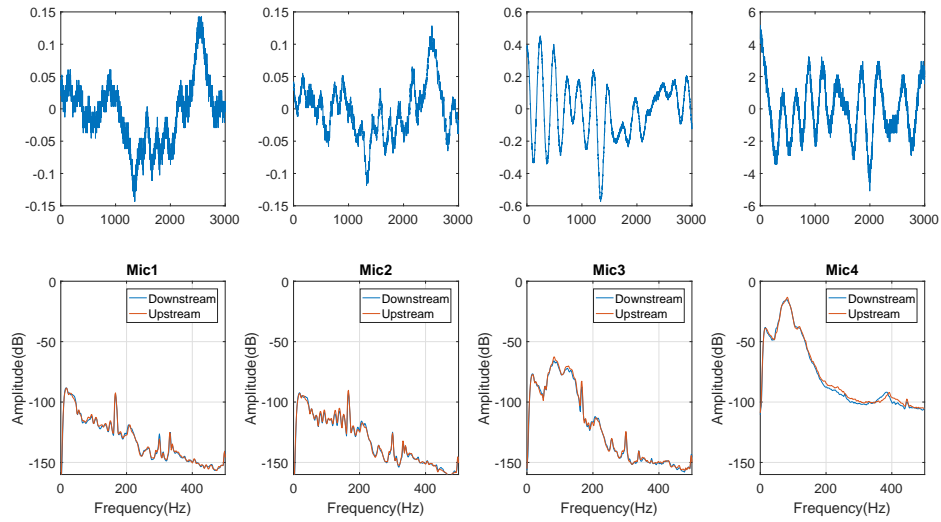
(a) U_∞=6.2m/s
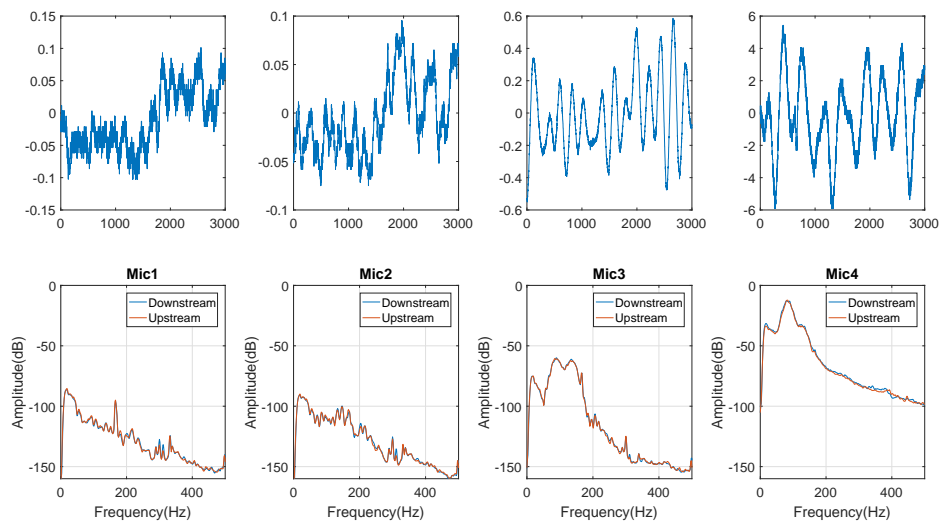
(b) U_∞=6.6m/s
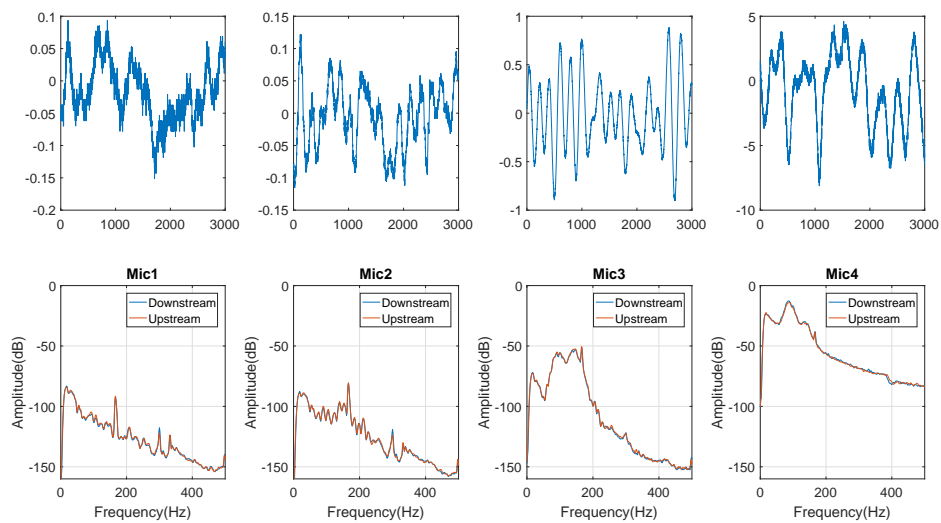
(c) U_∞=7m/s

Figure 6.5: Power Spectral Density Analysis for velocities 6,6.6 and 7 m/s. The first row corresponding to each velocity shows the pressure signals from each microphone, the second row shows the corresponding PSD plots. Upstream and Downstream refer to the PIV cases in which the field of view is at 280mm and 385mm respectively

Looking at the subsequent Figures 6.5 and 6.6 carefully,this peak is visible for all the plots, but however does not interfere majorly with our results or their interpretation. To this extent,although visible, it can be safely ignored.

Let us now analyse the PSD plots. For velocities U_∞=6.2,6.6 and 7m/s (Figure 6.5) the filtered signals are shown just above the spectral densities. It can be seen that for microphones 1 and 2 at distances x=200mm and x=300 respectively, there are some frequencies visible with a very low amplitude. However, these are not characteristic of Tollmien Schlichting waves which are a band of frequencies which is clearly distinguishable from the surrounding frequencies. Microphone 3 is where we start seeing such a bump at around 150Hz. The pressure signal also looks characteristic of TS waves, which appear as wave-packets. Microphone 4 shows an increase of the magnitude of this bump. However, upon noticing closely, even the higher frequencies have risen in magnitude, which could mean that the flow is close to becoming turbulent. This is evident from the pressure signals which start to look more jagged. As seen from the C_p measurements, transition occurs at x≈520 mm, which is very close to Microphone 4, meaning that the regime is lost likely non-linear.

For slightly higher free-stream velocities (U_∞ =6.6 and 7 m/s), it can be seen that the bump in the PSD plot for microphone 3 is expanding as well as the amplitudes are increasing. This makes sense since an increase in velocity reduces the thickness of the boundary layer and causes the flow to transition earlier. This means TS waves form sooner and grow faster too. The neutral stability curve from LST also expands with increasing velocity, meaning that the frequencies of flow-instabilities that are unstable also grow. The dominant frequency at U_∞=6.2 m/s is 80 Hz, while at U_∞=7 m/s it is 90 Hz.

Another set of cases was performed for free-stream velocities U_∞= 9,9.4 and 9.8m/s (Figure 6.6) in order to try and capture clean TS waves between Microphones 2 and 3. Like before, Microphone 1 is at a position too upstream in the flow for flow instabilities to be visible. The spectral density show some frequency fluctuations having a relatively low amplitude. The pressure signal too, seems like it contains a lot of noise and is of low amplitude. Microphone 2 starts to show a much better band of frequencies, which are definitely TS frequencies. The signals look like classic Tollmien-Schlichting wave signals. Microphone 3 also shows these signals, however, the amplitude has increased by about 10 times (one order of magnitude). This is good evidence to show that TS waves grow extremely fast (in fact, they grow exponentially). This is why characterization of the waves is so important, TS waves are very sensitive to the adverse pressure gradient and easily become non-linear.

The amplification of the magnitude of the TS band can also be seen by observing the pressure signals themselves directly. Although this does not give the whole picture, a qualitative guess can be made from these signals.Between microphones 2 and 3, for each of the velocities in Figure 6.6, the amplitude has shot up by an order of 10^1. However since the pressure signal contains all the frequencies, judging the amplitude directly can be misleading. Instead it is useful to look at amplitudes from the Power Spectral Density plots (in dB). TS frequencies grow logarithmically, and this can be seen in the change in amplitudes (in dB) on the y-axis.For the case of U_∞=9m/s, the peak at 200Hz grows from about -60dB (10^{-3} Pa) to about -20 dB (or 10^{-1} Pa), which means growth by a factor of 100. Similar exponential growth can be seen for the cases of U_∞=9.4 and 9.8m/s.

Looking back to the gradient of the C_p plots for this case (Figure 6.2), transition seems to occur just downstream of microphone 3 (x=400mm), and by the time it reaches microphone 4, it has already become turbulent. This is also visible as an amplification of all the frequencies and a pressure signal that looks very jagged and noisy. Thus, microphones 2 and 3 form a sweet-spot within which the TS waves are still linear, strong in magnitude and clearly measurable. This region will thus be our main focus for application of control and the analysis from here onwards.

(a) U_∞=9m/s

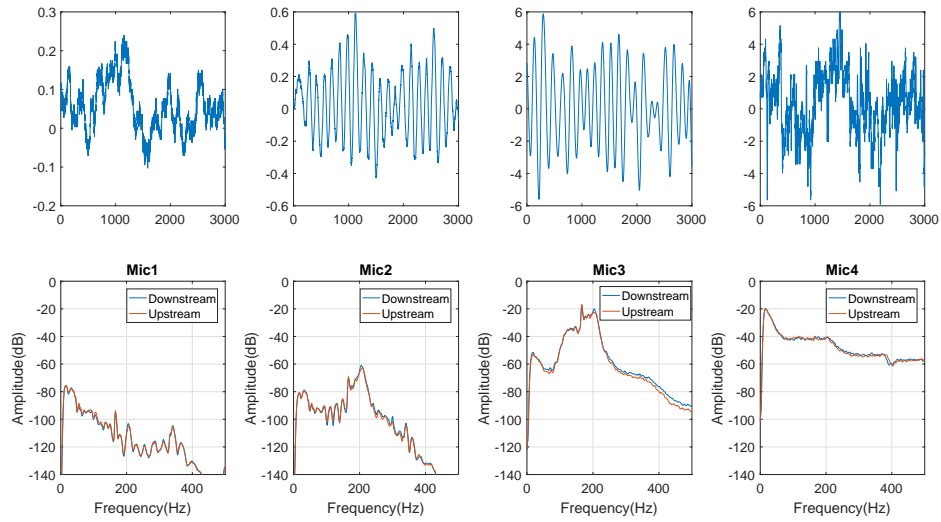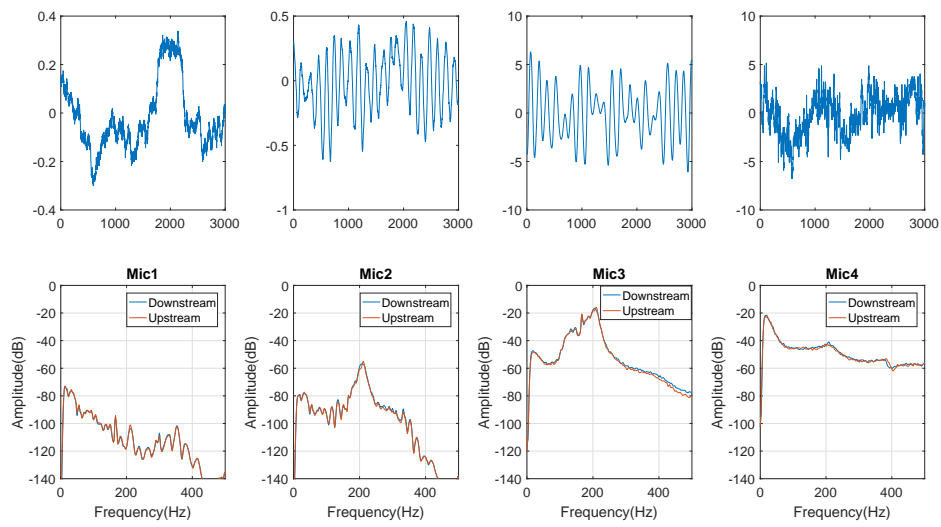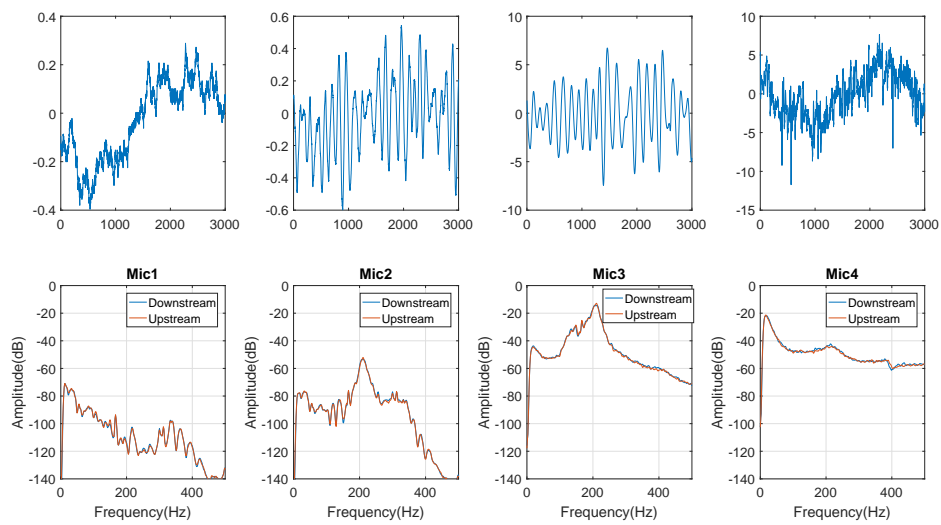(b) U_∞=9.4m/s

(c) U_∞=9.8m/s

Figure 6.6: Power Spectral Density Analysis for free-stream velocities 9,9.4 and 9.8 m/s. Upstream and Downstream refer to the PIV cases in which the field of view is at x= 280 mm and x=385 mm respectively

Growth of Disturbance Amplitudes at Microphone Locations

In order to study the variation of amplitudes of the TS disturbances present in the flow, it is worthwhile to plot the root-mean-square (RMS) of the signals for each microphone to see which the dominant frequencies are and in what region. Since the RMS is a measure of the fluctuations in the signal, this will give a good measure of the amplitude of the TS fluctuation present. To find out the RMS of each signal, it is filtered using a band-pass Butterworth filter (order 4) using a range of $\pm 5Hz$ on either side. So the RMS for a signal of 90Hz is the RMS of the signal filtered between 85 and 95Hz. This is done for a range of frequencies around the most dominant TS frequency for the first 5 microphones (which have the same sensitivity). The plots for U_∞=6.2,6.6,7,9,9.4 and 9.8 m/s are shown in Figure 6.7.

For U_∞=6.2 m/s, the amplitude of the disturbance is the highest at 80 Hz (Figure 6.7a). It can be seen that as the velocity is increased from U_∞=6.2 m/s to U_∞=6.6 m/s, the amplitude at 80 Hz increases. In fact,with increasing velocity, the frequencies above 80 Hz seem to increase in magnitude while those below 80Hz seem to decrease. Furthermore, on going from U_∞= 6.6 m/s to U_∞= 7 m/s, the 90 Hz frequency seems to become the most dominant, while the RMS corresponding to 80 Hz has fallen below. This is strong evidence of the way in which the amplitudes of the disturbances behave (Mack(1984)).

As the velocity increases from U_∞=9 to 9.8 m/s, the change in the disturbance amplitudes is again evident. The most amplified frequency in this case is around 200 Hz at U_∞=9 m/s. As U_∞ increases from 9 to 9.8 m/s, the amplitude corresponding to 200 Hz tends to reduce while that corresponding to 210 Hz increases in amplitude, becoming the most-dominant at 9.8 m/s.

It must be noted that the most dominant frequency using this method may not necessarily be the same as the actual most dominant frequency. This is because this method chooses a limited resolution of frequencies. This means that 210Hz in Figure 6.7e may not necessarily be the highest, and probably 205Hz or even 215Hz may be dominating here. However due to the fact that the next frequency is only 220 Hz, one cannot tell the exact leading frequency. Nevertheless, this method is able to provide a decent idea of the growth of the TS frequencies with velocity and distance, and for the purposes of the characterization, is sufficiently resolved. For a more detailed growth of disturbances with a higher frequency-resolution one is referred to the PSD plots in Figures 6.5 and 6.6.

Growth of Disturbance Amplitudes per Frequency

Another way of investigating the shift in the TS frequency band is to plot the RMS of the filtered signal with the frequency for the specific microphone positions. This is quite similar to the previous analysis, however, here one can see the band shifting. It is, in a way, a zoomed-in version of the PSD plots from Section 6.1.2, only instead of the SPL on the y-axis , it is the RMS values.

Like before, it can be seen that for a given position of the microphone, as the velocity increases the dominating frequency becomes higher. For example, for Mic 4, the dominant frequency increases from 80 Hz at U_∞=6.2 m/s to 90 Hz at U_∞=7m/s. This is also seen for Mic 3 and Mic 5, where the dominant frequencies are also growing.

Figure 6.8a,6.8b and 6.8c also indicate that for the lower range of velocities (U_∞=6,6.6 and 7 m/s), the largest amplitudes are at the position of Microphone 4 (x=490mm). The second largest are at Mic 5, however, this is because the flow has already become turbulent at this point. Mic 3 also has considerable disturbance amplitudes and so the area between Mic 3 and 4 show developing TS waves well, for this range of velocities.

For the higher range of velocities U_∞=9,9.4 and 9.8 m/s (see Figures 6.8d, 6.8e and 6.8f), the highest amplitude occurs at the position of Microphone 3 (x=400mm). For Microphone 2 (x=300 mm) the amplitudes of the TS frequencies are also considerable indicating that the dominant TS modes are between Microphone 2 and 3 for these velocities. Furthermore, the shift in the frequency band (from 200 to 210Hz) is visible at both positions of Mic 2 and Mic 3. At the positions of Mic 4 and 5, the flow has already become turbulent as shown by the relatively constant values of the RMS values.

Upon looking closer at Figure 6.8d, one sees that the the highest amplitude at Mic 3 corresponds to a frequency of not just 200 Hz but also 170Hz. This is because from the zero-run (Section 6.1.2) it was shown that the rogue frequency of 166 Hz is present in the flow, which gets amplifies due to the flow-instabilities in the boundary layer and appears to have almost equal magnitude as that of the dominant TS frequency (200 Hz).

Another interesting observation can be made. An increase in the velocity at higher ranges of free stream causes the band to shift to at almost the same rate as that at lower ranges of freestream. For example, for the same jump in velocity of 0.8 m/s, the dominant frequency moves from 80Hz at U_∞=6.2m/s to 90Hz at U_∞=7 m/s (for the position Mic 4: x=490 mm), an increase of 10Hz of TS frequencies. For the same jump in velocity
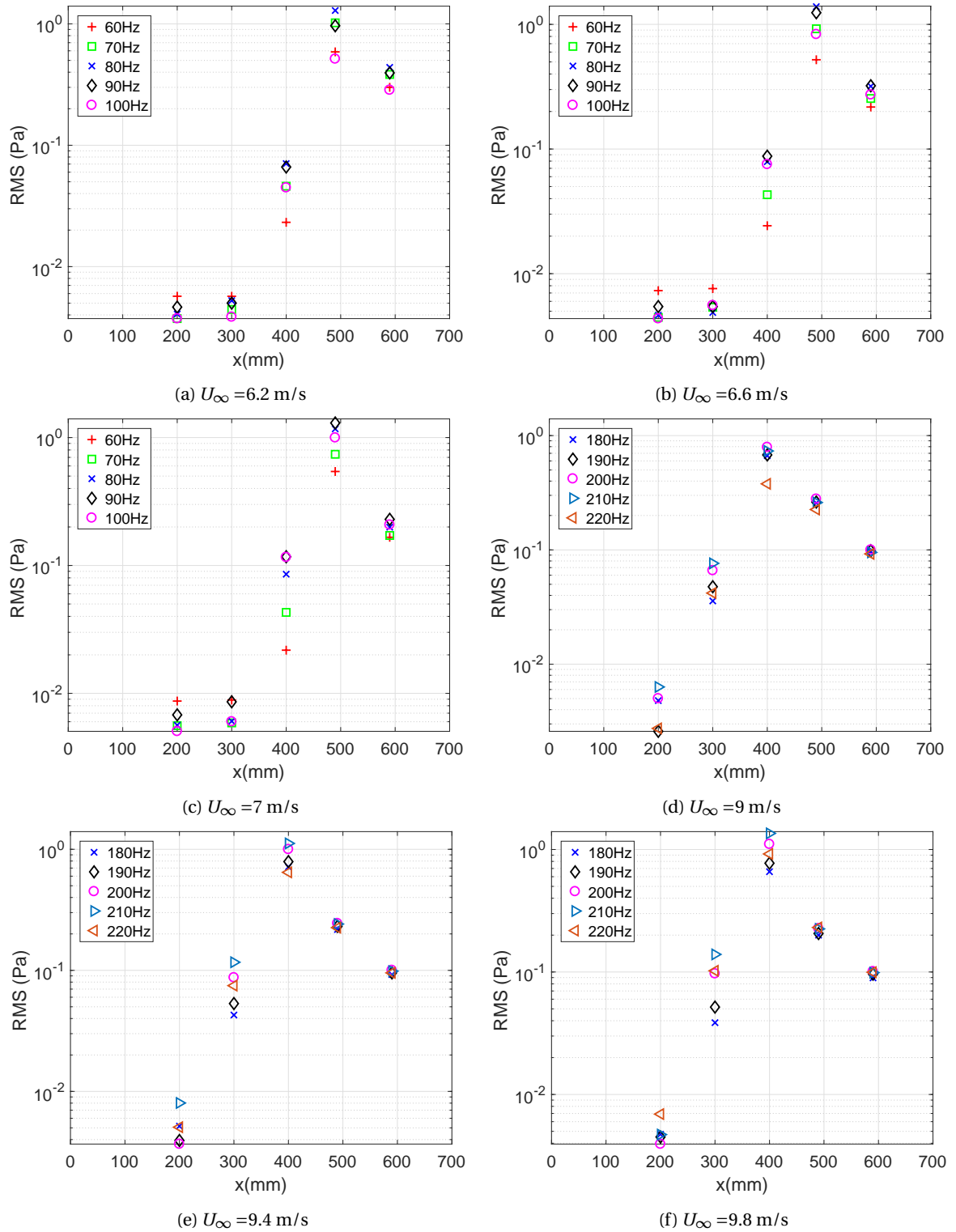
Figure 6.7: RMS value of each signal filtered at ±5Hz around each chosen frequency, with the position of the first five microphones (x=200,300,400, 490 and 590 mm) . For the free-stream velocities U_∞=6,6.6 and 7 m/s the frequencies analysed are 60-100 Hz (with steps of 10Hz) while for U_∞=9,9.4 and 9.8 m/s, the chosen frequencies are 180-220Hz (steps of 10 Hz)
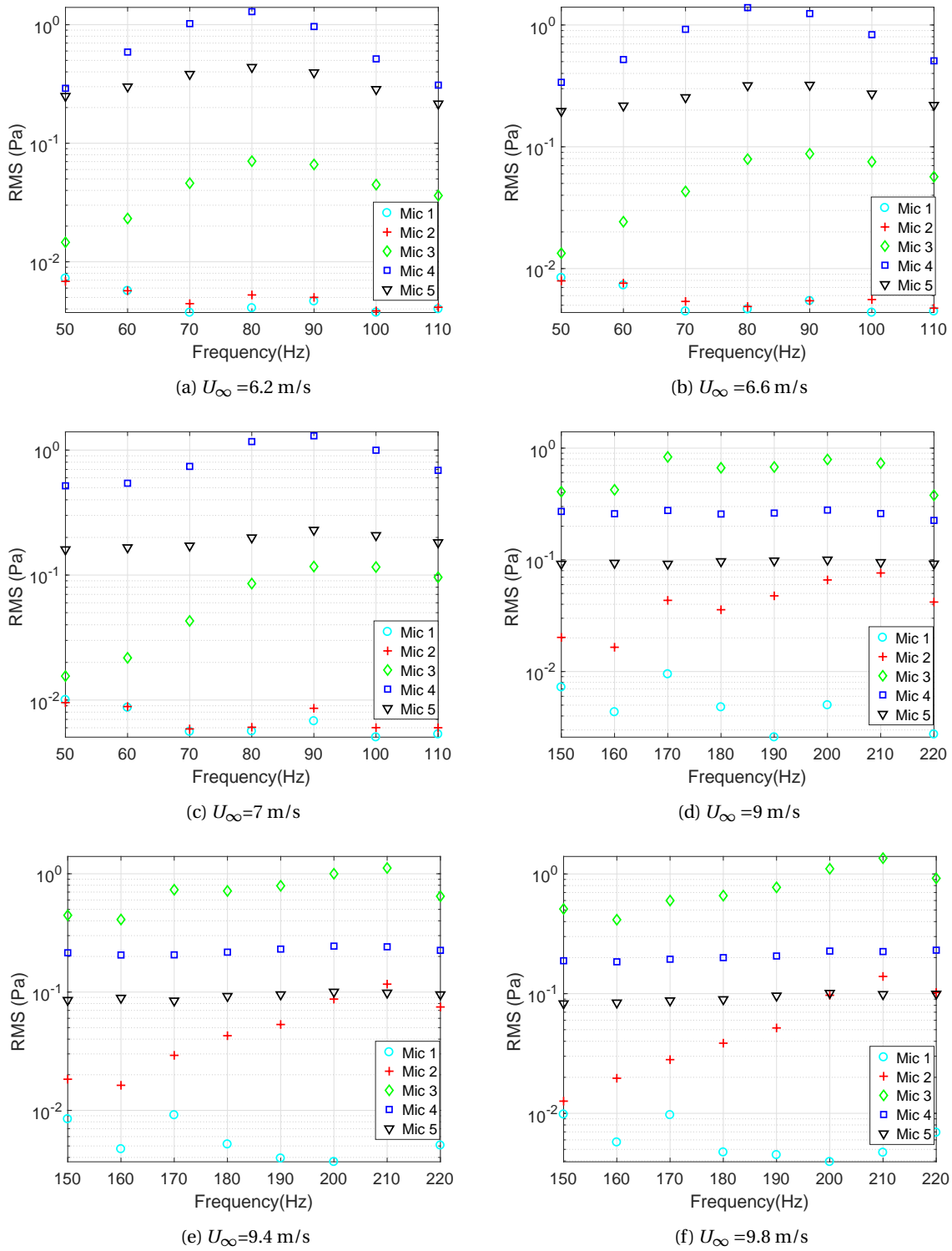
Figure 6.8: Growth of amplitudes of the disturbance frequencies in the TS wave packet for Microphones 1,2,3,4 and 5 (x=200,300,400,490 and 590 mm respectively). For the first three velocities, U_∞= 6,6.6 and 7 m/s, the analysed frequency range is 50-110Hz while for U_∞=9,9.4 and 9.8 m/s the analysed frequency range is 150-220Hz

at the higher ranges, the dominant frequency moves from 200 Hz at U_∞=9m/s to 210 Hz at U_∞=9.8m/s (for the position of Mic 3: x=400 mm), a shift in the dominant frequency of also 10Hz.

In order to find the wavelength corresponding to the dominating frequencies (λ_{dom}) the following formula is used

$$\lambda_{dom} = \frac{v_{conv}}{f_{dom}} \tag{6.1}$$

Here v_{conv} is actualy half the free stream velocity (=0.5U_∞). (Dovgal et al.(1994)) The following table summarizes the dominating TS wave frequency at the the different locations as well as its wavelengths.

$U_\infty(m/s)$	f_{dom} (Hz)	λ_{dom} (m)
6.2	80	0.0388
6.6	80	0.0412
7	90	0.0389
9	200	0.0225
9.4	210	0.0224
9.8	210	0.0233

Table 6.1: Wavelengths of the dominant frequencies, λ_{dom} for the range of free-stream velocities

Thus, as the free stream velocity increases, so does the dominating frequency. The above table also shows that the average wavelength of the TS waves is about 2.2 to 4.1 cm. Thus, in order to capture a few TS waves, say 4, within a single PIV window, a size of about 8.8 cm to 16 cm is acceptable. For this experiment, a FOV of 13 cm was chosen.

Two- Dimensionality of TS Waves

In order to assess the two-dimensional nature of the flow, the PSD of the signals from two of the spanwise microphones at x=300 mm were taken (Mic 2 and 10 in Figure 5.3). They are both at a distance of 30mm from the centerline.

(a) Mic 10, z=-30 mm   (b) Mic 2, z=30 mm
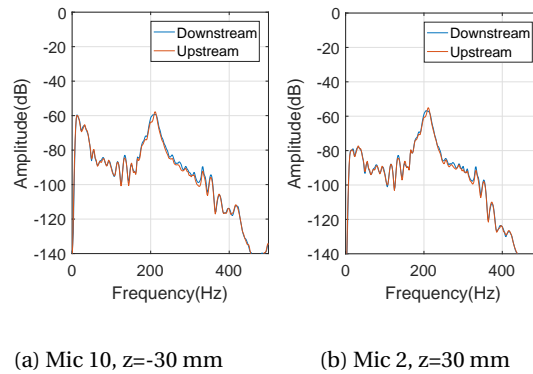
Figure 6.9: PSD plots of two spanwise microphones for U_∞=9.4m/s. Mic 2 is at a distance of 30mm to the right of the centerline while Mic 10 is to the left of it (See Figure 5.3)

The above figure shows that for the two microphones the frequency-bands are almost the same, which means that the TS wave strength must be the same at these two locations. Furthermore, C_p measurements were taken at the three spanwise branches of the pressure tabs, the first at x=160 mm, second at x=340 mm and third at x=520 mm. There were a total of five spanwise pressure tabs, each with a distance of 50mm from each other.
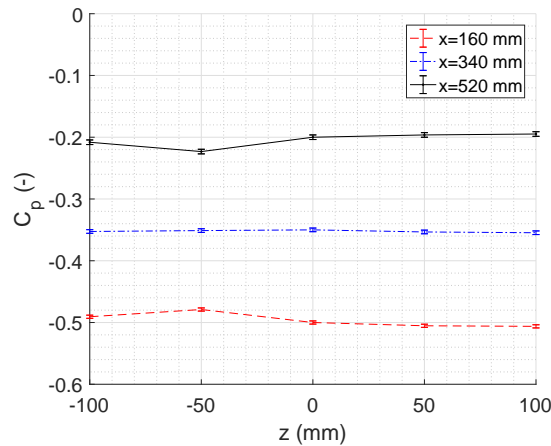
Figure 6.10: Spanwise variation of C_p for three locations along the plate. U_∞=9.4 m/s

It seems that the pressure is more or less equal across the spanwise tabs, for a given x location. The standard deviation too , for a particular x location was found to be about the same (0.01 units on either side), meaning that the C_p fluctuations are also almost equal spanwise. Thus, it can be safely concluded that the TS waves, at least close to the centerline, are two dimensional. For sure, as one goes further away from the centerline, the TS waves will be different (in fact more in magnitude) due to the interference of the side-walls and the boundary layers formed around them.

6.1.3. Velocity Field Statistics

This section presents the velocity field profiles for the first experimental campaign (with which PIV was carried out). This will help in characterizing the type of boundary layer, the type of flow and the location of transition. In this analysis, only the profiles for the velocities U_∞= 9,9.4 and 9.8 m/s are presented since these are the regions with strong clearly discernible Tollmien-Schlichting waves. More importantly,these are the range of velocities where control was performed in the second experimental campaign.

The mean velocity profiles ($\bar{u}$ and $\bar{v}$) are analysed here to get a quantitative estimate of the flow inside and outside th boundary layer. Also calculated here are commonly used parameters to describe the shape of the boundary layer, type of flow and location of transition : displacement thickness (δ^*),99 % boundary layer thickness(δ_{99}),momentum thickness (θ) and the shape factor (H).

Mean Profiles

The mean velocity profiles provide the first insight into the velocities within the boundary layer and the far stream velocity. Figure 6.11 shows the mean velocity profile ($\bar{u}$) for the case 9.4 m/s. Figure 6.12 shows the streamwise evolution of the velocity profile at three x-positions, x=300, 350 and 400 mm for U_∞=9,9.4 and 9.8 m/s

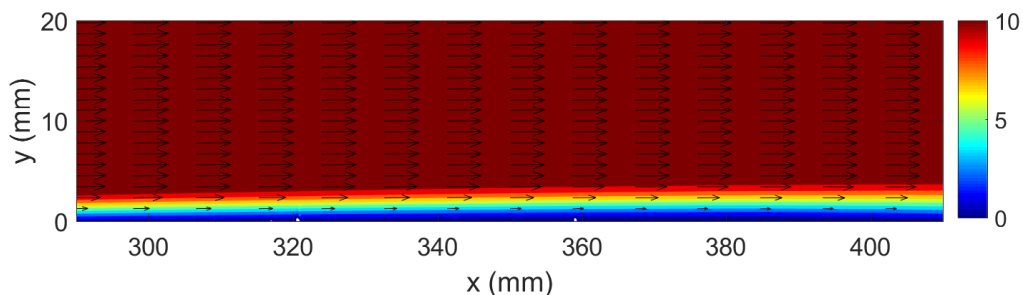Figure 6.11: Contour plot of the mean velocity profile ($\bar{u}$), along with vectors for the free stream velocity,U_∞=9.4 m/s
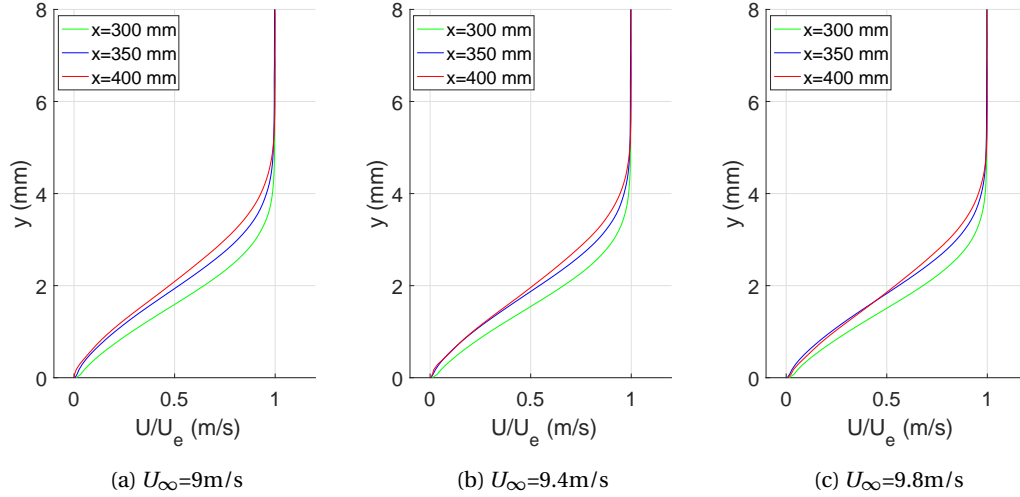
(a) U_∞=9m/s   (b) U_∞=9.4m/s   (c) U_∞=9.8m/s

Figure 6.12: Evolution of the mean velocity-profiles (normalized) at x=300,350 and 400mm for U_∞=9,9.4 and 9.8 m/s

One can clearly see that for all the velocity cases there is an inflection point in the velocity-profiles. This is a clear indication of the existence of an adverse pressure-gradient. Furthermore, the presence of an inflection point is also a necessary and sufficient condition for the existence of inviscid instabilities for wall-bounded flows (also called Reynold's inflecion-point theorem, Gad-el Hak (1989)). These will manifest as Tollmien-Schlichting fluctuations in the boundary layer. It is observable that for a given free-stream velocity, as one moves downstream, the inflection becomes more prominent and the profile less full, meaning that the instabilities are stronger at the downstream position (x=400 mm) compared to the upstream position (x=300 mm). Furthermore, with increasing free-stream velocity, one can observe the boundary layer thickness reducing (see next section for values of the boundary layer parameters).

An error analysis in the measurement of the mean-velocity (for U_∞=9.4 m/s) is performed using Equation 4.6, from the paper of Sciacchitano and Wieneke(2016). The error obtained in the domain is shown in Figure 6.13. Two points are chosen to be analysed: Point 1 is outside the boundary layer in the far stream at x=290mm and y=18mm while Point 2 is inside the boundary layer at x=410mm and y=2mm.
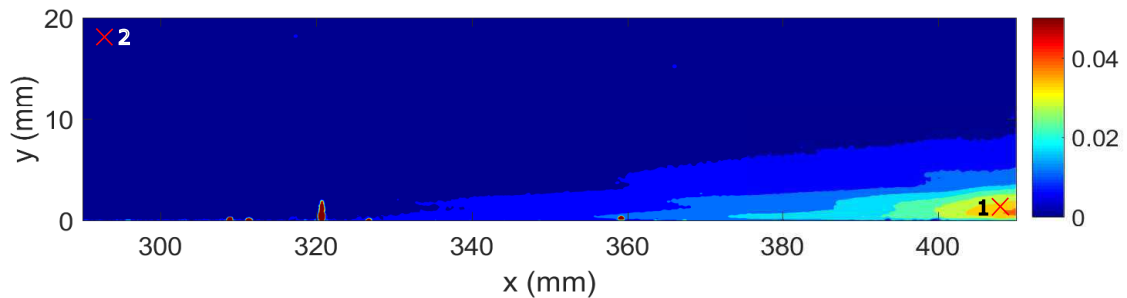
Figure 6.13: Error in the estimation of the mean velocity profile ($\varepsilon_{\bar{u}}$) for the entire domain as computed using the technique in Sciacchitano and Wieneke(2016). Two points are quantitatively analysed.

For point 1, the error in calculating the mean velocity is 0.04 m/s while that for point 2 is 0.0022 m/s. This makes sense since Point 1 is in the position of strong flow-instabilities thus the fluctuations are larger, meaning that there is a larger error in the computation of the velocity. Point 2 being far from any boundary layer instabilities, shows a much lower error in estimation of velocity.

Furthermore, one can validate the measurements of the PIV by comparing them with the inviscid velocities calculated from the C_p measurements from the pressure tabs. Table 6.2 compares the inviscid velocities (obtained from Figure 6.3) with those from PIV for the case U_∞=9.4 m/s. The error in the computation is less than ±0.04 m/s for all positions, showing that both techniques independently give almost the same results.

Measurement Type	Position (mm)	Velocity (m/s)
PIV	300	11.08
	350	10.91
	400	10.80
Pressure tabs (Inviscid Velocity)	300	11.12
	350	10.94
	400	10.82

Table 6.2: Comparison of velocities in the far-stream (y=18 mm) using PIV and pressure tabs, for different streamwise positions. U_∞=9.4 m/s

Boundary Layer Parameters

Investigating the thicknesses of the boundary layer (BL) also gives a measure of the behaviour of the flow. As described in Section 2.1.2, three parameters are commonly studied to understand the behaviour of the boundary layer along the wall : the displacement thickness (δ^*), the 99% Boundary Layer Thickness (δ_{99}) and the momentum thickness (θ). A fourth parameter, the shape factor (H) gives an idea of whether the flow is laminar or turbulent and where transition may be occurring.

(a) 99% Boundary Layer Thickness

(b) Displacement Thickness
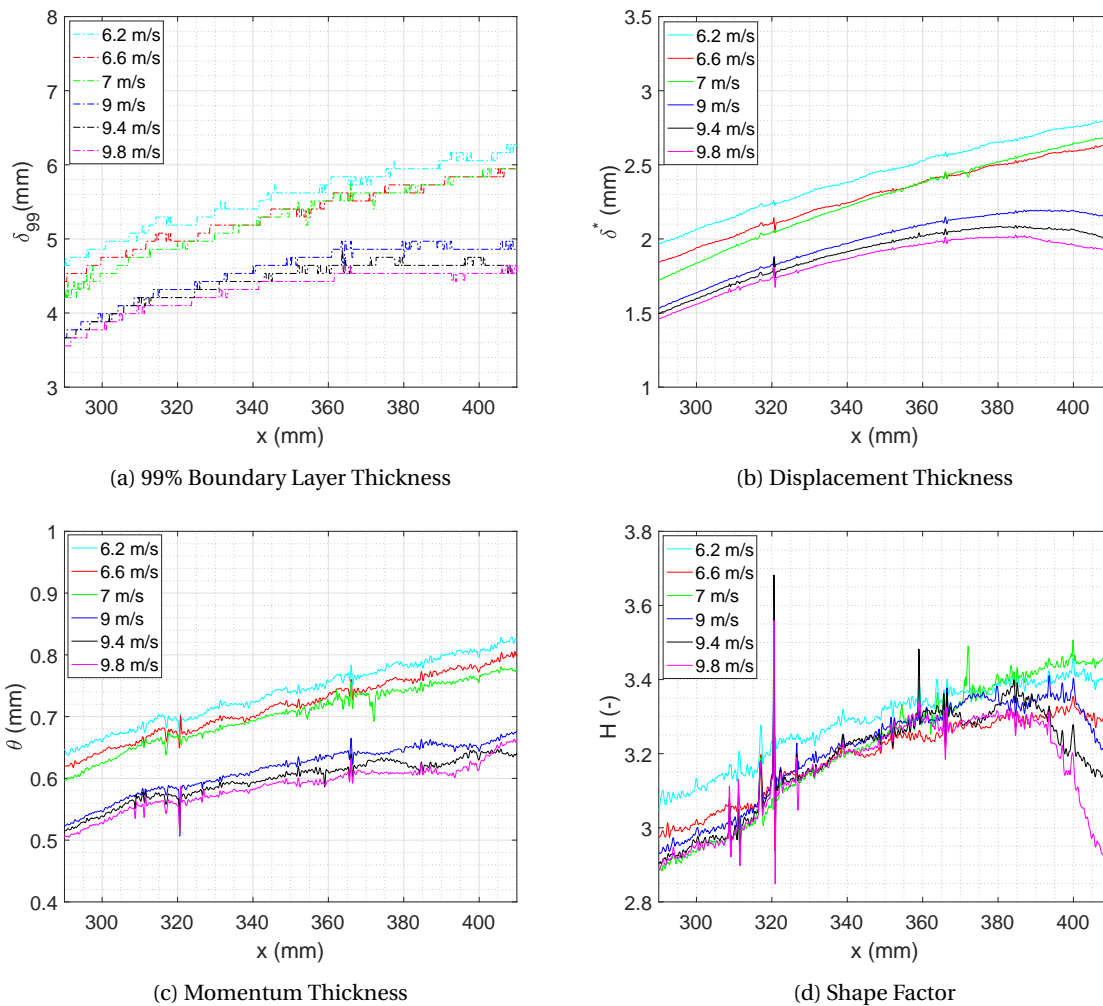
(c) Momentum Thickness

(d) Shape Factor

Figure 6.14: Comparison of the boundary layer parameters for the free-stream velocities U_∞=6.2, 6.6, 7, 9, 9.4 and 9.8m/s

The 99% BL thickness is the first measure of the thickness of the boundary layer. For lower velocities (U_∞=6.2,6.6 and 7 m/s), the frictional forces of the wall act upon the fluid particles stronger, leading to a

thicker boundary layer. Increasing the velocity causes lesser of the far stream fluid particles to be "stuck" to the wall, causing a decrease in the value of δ_{99} for the U_∞=9,9.4 and 9.8 m/s cases.

A similar logic applies in understanding the change in the value of δ^*. Since δ^* is the measure of the movement of the wall surface to keep the flow rate the same for the real viscous case as compared to the inviscid case, a higher velocity means a thinner boundary layer which means a reduction in the wall displacement needed to maintain the same flow rate. Hence, just like the value of δ_{99}, δ^* varies in the same way. It is thicker for lower velocities and thinner for higher velocities. Furthermore, the momentum thickness θ evaluates the wall displacement in the same manner as the displacement thickness, only in this case it is the total momentum instead of the flow rate. Just like δ^*, θ too reduces with increasing free-stream velocities.

Figure 6.14 shows these parameters for the whole range of velocities. For the case of θ and H, some spikes can be observed. This is owed to the PIV measurements where, as seen in the field profiles earlier, wall reflections cause the processing software to read it as a region of higher velocity. One such distortion is at x=320mm, while a few other minor reflections show up at x=360mm and x=365mm.

The shape factor also hints at the nature of the flow. For the lower range of velocities, the value of H is in the range of 3- 3.5, suggesting clear laminar flow (for the Blasius boundary layer , H=2.6 for laminar flow) (Schlichting et al.(1955)). The increase in the shape factor as one moves downstream is also an indication of the velocity-profiles becoming less full and more inflected. This is because the flow-instabilities start to become stronger as the boundary layer grows. For the higher range of free-stream velocities, namely, U_∞= 9 to 9.8 m/s, the value of H drops rapidly. This is an indication of the beginning of the transitional regime, where non-linear effects are starting to dominate. For turbulent flows, the value of H roughly is in the range of 1.3-1.4 for Blasius flows (Schlichting et al.(1955)). However, this lies outside the field of view of our PIV setup, and thus cannot be measured.

6.1.4. Fluctuation Statistics

This section presents a quantitative analysis of the fluctuations present in the flow by considering three quantities : RMS profiles (U_{rms}, V_{rms}), Reynolds stresses ($\rho\overline{u'u'}$,$\rho\overline{u'v'}$,$\rho\overline{v'v'}$)and Turbulent Kinetic Energy.

RMS Profiles

The Root-Mean-Square (RMS) of a quantity simply gives the magnitude of the fluctuations present in that domain. A higher value means that the value fluctuates more from the mean. Figure 6.15 shows the value of these fluctuations increasing in magnitude as one moves downstream. TS waves cause the shape of the RMS fluctuation profiles to appear as a double-crested peaks (Grundmann and Tropea(2008),Schubauer and Skramstad(1948)). Stronger the magnitude of these TS waves, the stronger the fluctuations and the more pronounced the crests and peaks in the RMS velocity profiles.

According to Grundmann and Tropea(2008) , the sure sign of a TS wave is by observing the ratio of the standard deviation of the velocity,U_{rms} normalized with the free stream velocity. If there is a small maximum near one boundary layer thickness δ_{99} and a minimum just below it, along with an increase in fluctuations near the wall, this is a TS wave footprint. Clean TS waves of a single certain fundamental frequency would mean that only one crest is visible. The δ_{99} of for the higher velocity cases was found to be about y=4mm (see next section). Double and triple crested peaks (near x=400 mm) are observed, meaning that the disturbances possibly have more than one fundamental frequency (Kachanov and Levchenko (1984)). This could mean that there are more disturbances in the flow apart from the TS disturbances. Possible causes could be geometrical imperfections in the setup, minor three-dimensional effects, resonant interactions or the rogue-frequency of 166 Hz as observed before.
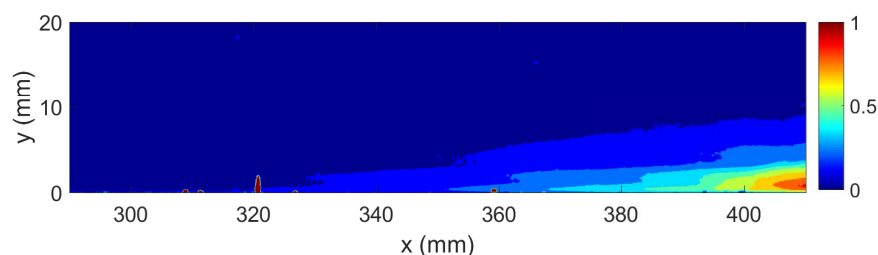

Figure 6.15: The RMS velocity of the U-component for U_∞=9.4 m/s

In order to further analyse the regions seen in the RMS plots, it is standard practice to plot the rms-velocity profiles against the height of the boundary layer. Figure 6.16 compares the rms profiles for three velocities U_∞=9,9.4 and 9.8 m/s, at three streamwise locations.
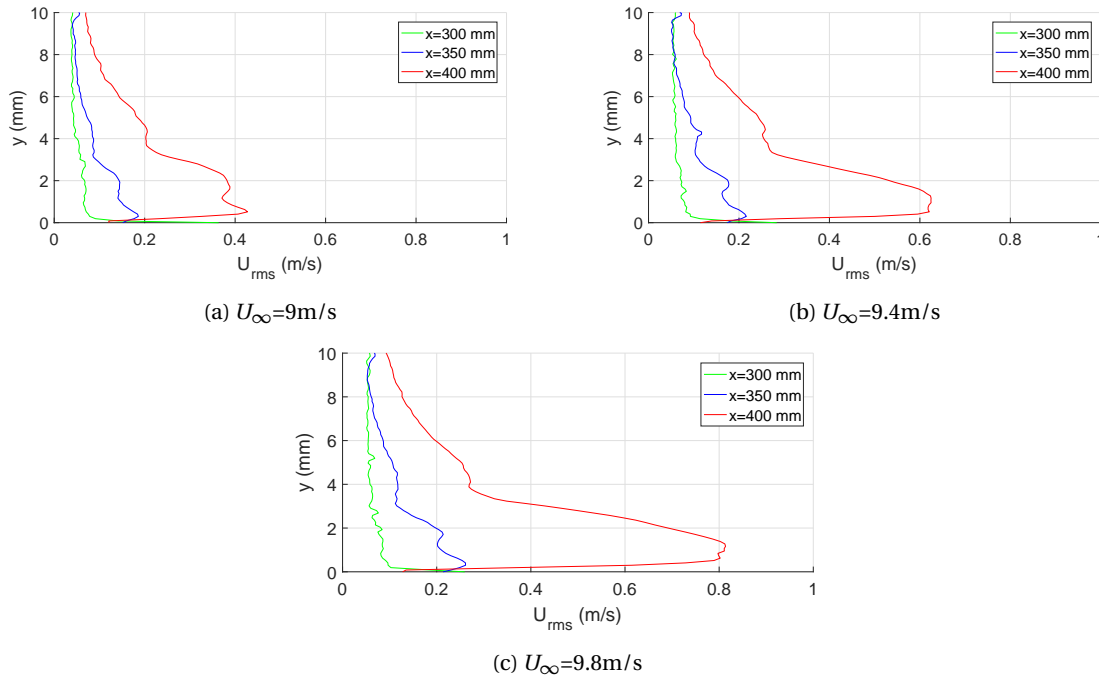

(a) U_∞=9m/s

(b) U_∞=9.4m/s

(c) U_∞=9.8m/s

Figure 6.16: Plots of the U_{rms} velocity profiles at x=300,350 and 400mm

A number of things can be observed here. For the case of U_∞=9 m/s (at x=400mm), a bump in the curve is visible at the position of one-boundary layer thickness($\delta_{99} \approx$4.2mm; see Figure 6.14). There is also a minima just below δ_{99}. As stated earlier, this a clear TS wave footprint (Grundmann and Tropea(2008)). Furthermore, a clearly discernible double peak curve is visible for this case. The first peak is at about y=0.5mm and the second at y=1.7mm respectively. For x=350mm, a similar shape is observed - with both the minima at roughly one δ_{99} and a double peak close to the wall. For x=300mm, the bump is much harder to observe due to the low energy of the TS wave, in its early growth stages.

As the velocity increases, it can be noticed that the strength of the U_{rms} values to increase. This is expected. It seems like for the U_{rms}=9.8 m/s case, that there is a single peak , however, as seen before, this is because the flow is almost nearing turbulence which is why the fluctuations and hence the RMS value increases rapidly.

A similar trend is observed for the RMS of the y-component of the velocity (V_{rms}). For plots of the V_{rms}, refer to Appendix A, under the section RMS Profiles.

Reynolds Stresses

The Reynolds-stresses are obtained after the Reynolds-averaging of the continuity and momentum equations (incompressible Navier-Stokes equations). A term on the right hand remains $\rho u_i' u_j'$, (alongside the viscous stresses), and is termed the Reynolds stress. It is the apparent stress due to the fluctuations in the velocity field. Expanding the notation, we get three types of stress- two normal ($\overline{u'u'}$ and $\overline{v'v'}$) and one shear ($\overline{u'v'}$).

Analysing the Reynolds stresses provides another measure to characterize the growth of the Tollmien-Schlichting waves. It is important to recognise that Reynolds stresses are not , in the traditional sense of the word, stresses. The effect of unsteady fluctuations in a turbulent flow cause additional momentum fluxes, which appear as "stresses" (White(1974)). Nevertheless, a stronger value of these perceived stresses means that there are more momentum fluxes due to the unsteady perturbations, meaning that there are stronger TS waves in that region.
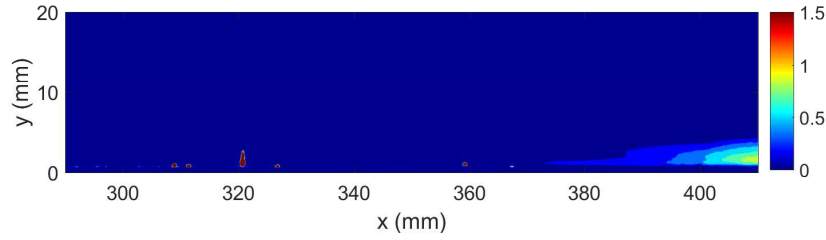
Figure 6.17: The normal Reynolds stress $\rho \overline{u'u'}$ for U_∞=9.4 m/s

Looking at the Reynolds stress profiles, it is quite evident that the value of the stresses is higher downstream compared to upstream. This means the fluctuations present in the flow cause more momentum to enter the fluid layer increasing the mixing and contributing more to the Reynolds-stress term. Furthermore, increasing the velocity also has the effect of allowing more momentum fluxes into the boundary layer due to stronger viscous effects (higher Reynolds number). This means that perturbations now grow faster and become stronger that their low velocity counterparts. More evidence can be obtained by looking at the profiles at positions over the flat plate (Figure 6.18).

For the U_∞=9 m/s case it is observed that the Reynolds stress increases from a value of 0.0058 at x=300mm to 0.21 at x=400mm, an increase by a factor of 40. For the U_∞=9.8m/s case, it can be seen that the Reynolds stresses increases from a value of about 0.0083 at x=300mm to 0.77 at x=400 mm, an increase of a factor of 90. This means that at higher velocities, for the same distance, TS waves seem to grow faster compared to lower velocities for all the same laboratory conditions.

(a) U_∞=9m/s

(b) U_∞=9.4m/s

(c) U_∞=9.8m/s
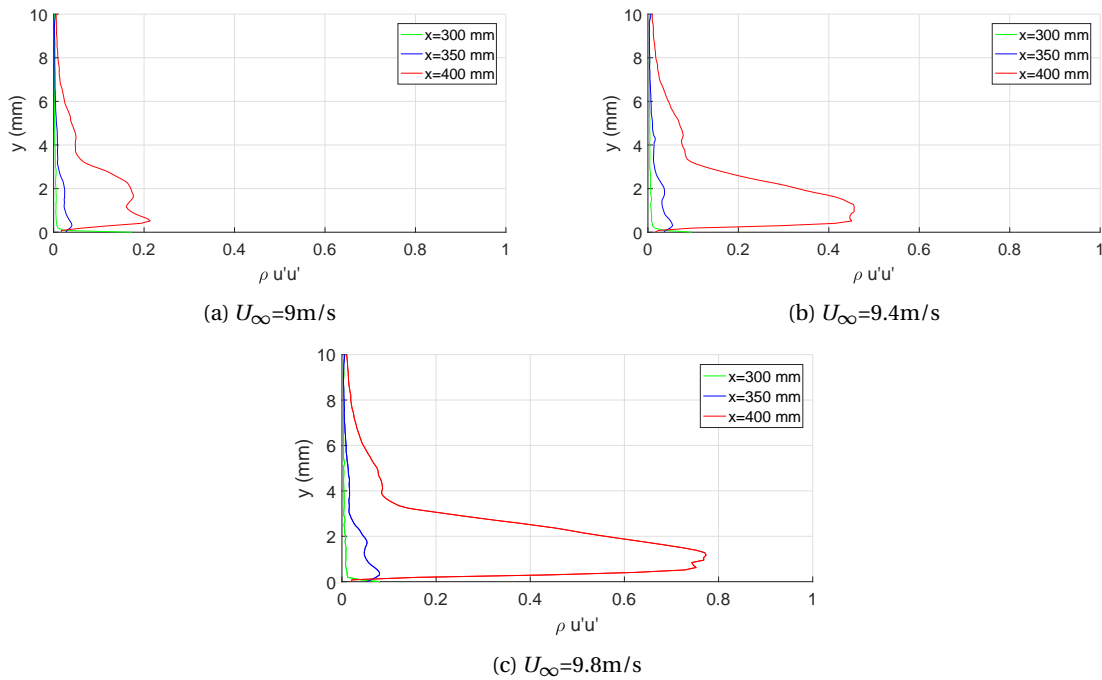
Figure 6.18: Profiles of the normal Reynolds stress $\rho \overline{u'u'}$ at x=300,350 and 400mm

The error analysis for the Reynolds stress profiles was computed using Equation 4.7. As before, Point 1 is the downstream point close to the boundary layer. At this point, the error for U_∞=9.4 m/s is ±0.057 m/s while that at Point 2 is about 1.8×10^{-4} m/s. This is reasoned once again as before, since Point 1 has higher fluctuations than Point 2.

Analysing the field profiles for the $\overline{v'v'}$ and $\overline{u'v'}$ also shows a similar trend an can be found in Appendix A under the section Reynolds Stresses.

Turbulent Kinetic Energy

In turbulence modelling, the term Turbulent Kinetic Energy (TKE) measures the mean value of the kinetic energy per unit mass due to the fluctuations present in the flow. Although a term normally used to characterise eddies in turbulent flows, here the value of this quantity can also give us an indication of the strength of the dominant perturbations in the flow, and thus the strength of the Tollmien-Schlichting waves. It is calculated as in Equation 4.5. A higher value of Turbulent Kinetic Energy means that those regions have a higher value of energy associated with the fluctuations present within the flow.
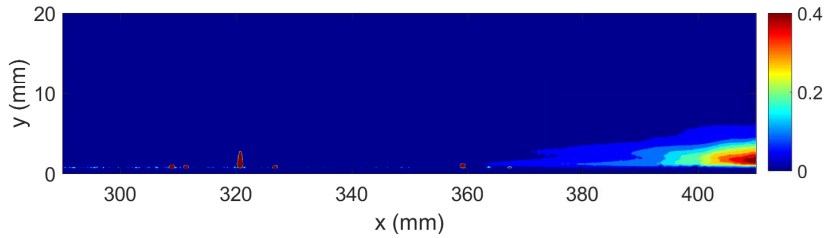
Figure 6.19: The Turbulent Kinetic Energy fields $1/2(\overline{u'^2} + \overline{v'^2})$ for U_∞=9.4 m/s

Looking at the contour plot of the TKE field for the case of U_∞=9.4 m/s, it is seen that the energy of the downstream regions is higher than that of the upstream regions. This is due to more energy present in the fluctuating regions as compared to the other regions.

Figure 6.20 compares the Turbulent Kinetic Energy profiles for three free-stream velocities U_∞=9,9.4 and 9.8 m/s. For U_∞=9 m/s, the maximum value of the TKE increases from a value of 0.0028 at x=300mm to 0.09 at x=400mm, a factor of 34. For the case of U_∞=9.8 m/s , turbulent fluctuations of as high as 0.35 can be observed at the position x=400mm compared to only 0.0042 at x=300mm. That is a growth in energy of a factor of about 83. This again, sheds light on the fact that flow instabilities tend to grow faster at a higher velocity for all the same given flow conditions.

The uncertainity in the calculation of the Turbulent Kinetic Energy is done using Equation 4.9 for the case U_∞=9.4 m/s. For the downstream (and inside the boundary layer) point 1, the error is ±0.034. For the Point 2 (away from the boundary layer) the error in the computation of Turbulent Kinetic Energy is around the order of 10^{-4}.

(a) U_∞=9m/s

(b) U_∞=9.4m/s

(c) U_∞=9.8m/s

Figure 6.20: Profiles of the Turbulent Kinetic Energy, $1/2(\overline{u'^2} + \overline{v'^2})$ at x=300,350 and 400mm

6.1.5. Modal Analysis

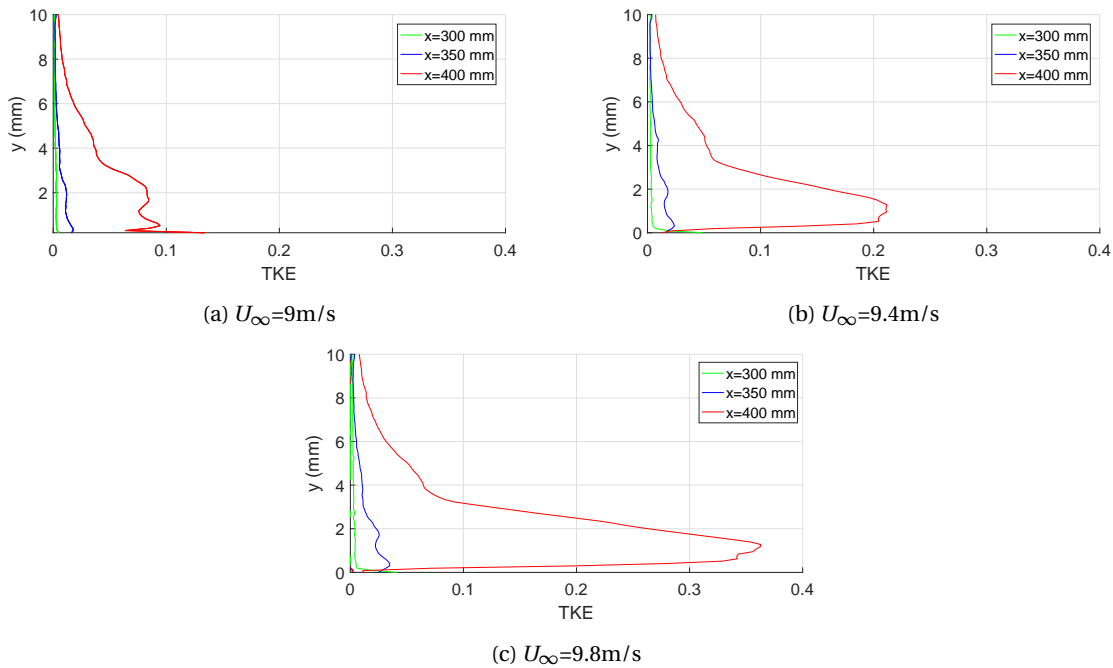Particle Image Velocimetry (PIV) has some limitations when it comes to being able to capture fluctuations like TS waves. This is because the energy of these fluctuations are too low compared to the mean flow to be singled out in an instantaneous frame . PIV analysis of the flow field, in this case, gets clouded out by noise. In order to tackle this, another technique called Proper Orthogonal Decomposition(POD) can be employed. The principle and methodology used in this thesis is outlined in Section 4.3. This section presents the results of the decomposition of the PIV data into its various modes, based on their energies.

From the data obtained, there is a total of 500 snapshots. This means, that based on the principle of the snapshot technique, there are corresponding 500 modes of energy. Each mode has a spatial function $\phi^{(k)}(x, y)$, its corresponding temporal coefficients $\alpha^{(k)}(t)$, and an associated energy, E_{mode}. In order to find the most energetic modes , it is useful to plot the energy of each mode as a percentage of the total energy as shown in Figure 6.21
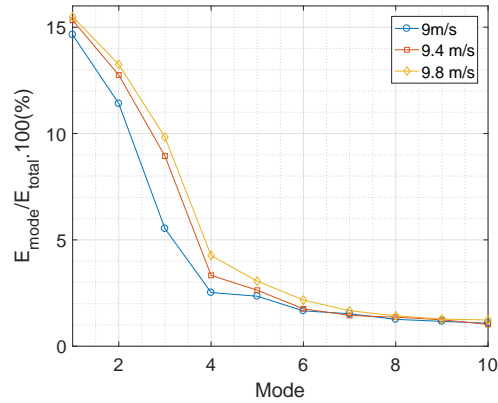
Figure 6.21: Energy percentage of each mode for the first 10 modes in the flow

It is observed that the first few modes (modes 1 to 4) capture most of the energy present in the flow, accounting for about 42% of the total energy. Beyond mode 6, as seen in Figure 6.21, contribute to less than 1% of the energy and therefore need not be considered. The corresponding Eigen functions $\phi^{(k)}$ for the u and v-components of the velocity for the first 4 modes are shown in Figure 6.22. These are for U_∞=9.4 m/s.
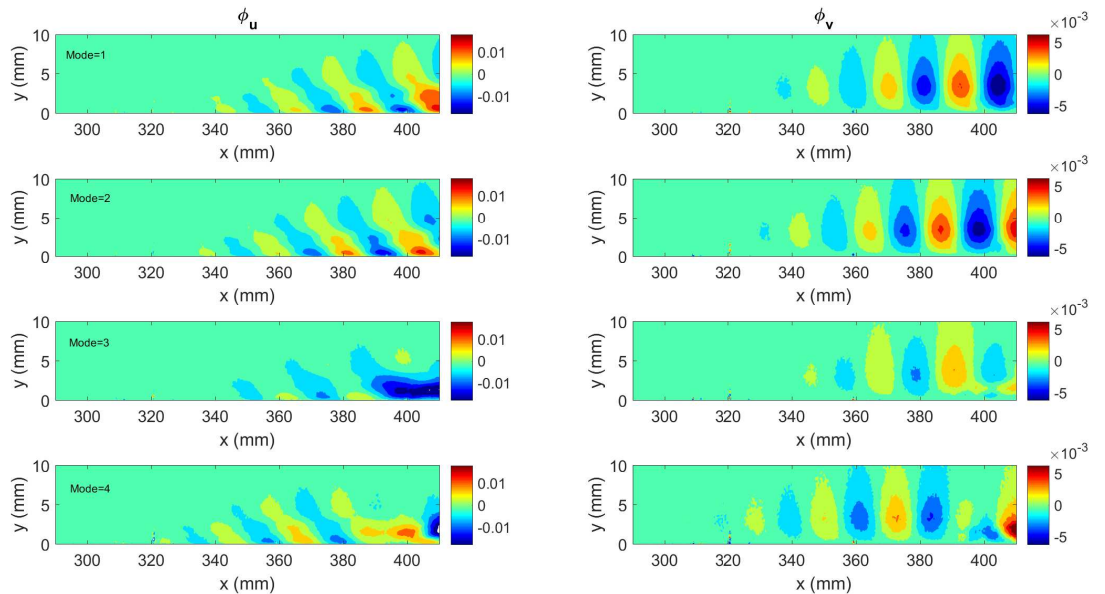
Figure 6.22: Eigen functions ϕ_u and ϕ_v for the first 4 modes. U_∞=9.4m/s

For both ϕ_u and ϕ_v, the structures present in the flow become visible. In the streamwise direction these take the shape of alternating regions of positive and negative values of ϕ. This happens for both the u and v-components, however, their shapes are quite different. The eigen-function corresponsing to the u-component(ϕ_u) has a shape that distorts and is asymmetrical. This can be seen if one considers a given x-position, where upto a certain wall-normal distance there is a positive value while it becomes negative as one goes further. For the eigen function corresponding to the v-component (ϕ_v), the structures of these modes are symmetrical in the wall-normal direction. It should be noted that no physical meaning can be derived from this contour plot of the eigen functions. In order to be able to visualize the coherent structures, the images need to be reconstructed.

Reconstructed Profiles

This section presents the reconstructed images using the most energetic modes (1 to 4) for the case U_∞=9.4m/s. The first four reconstructed images are presented here (the mean field is neglected). Figure 6.23 displays the fluctuating u and v components of the velocity. Each image row corresponds to one snapshot from the PIV Setup, the left image showing the reconstructed u-field , the right showing the v-field. It must be noted that the snapshots are not correlated. In that sense, the coherent structures visible in Snapshot 2 are not the same convected coherent structures from Snapshot 1. This is because the acquisition frequency of the camera is much lower (2.2Hz) compared to the TS frequencies (200Hz) which are convecting with the flow.
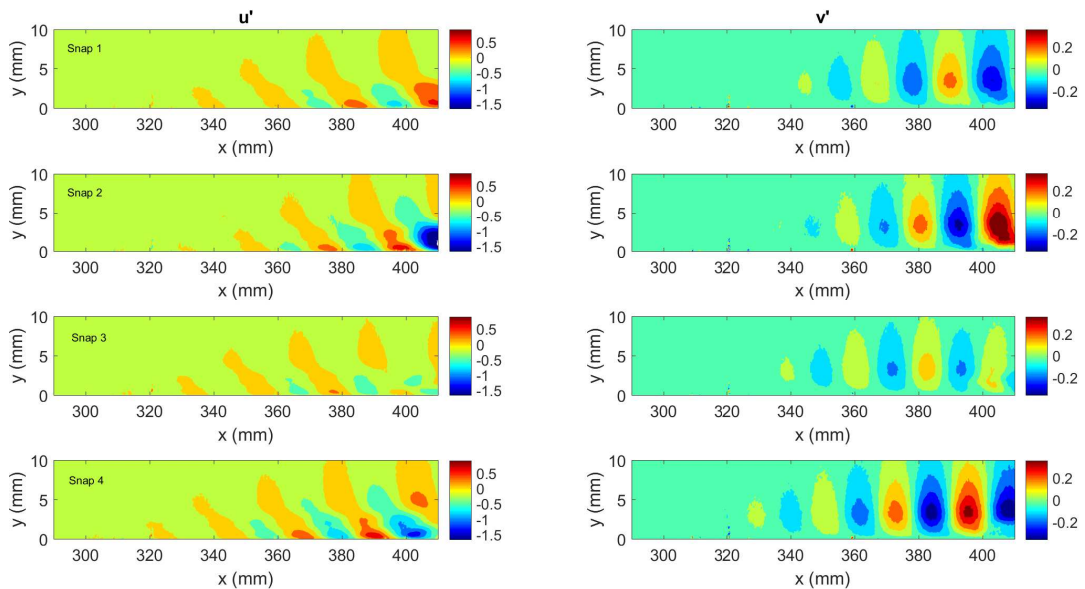
Figure 6.23: Reconstructed images for the fluctuating x- and y-components for the first four snapshots. U_∞=9.4m/s

The coherent structures presented here clearly identify as TS waves. The more redder-orange regions represent regions of positive velocity while the blue regions are of negative velocity. Taking a look at the u' components, one can see alternating regions of high and low (negative) fluctuations propagating in the x-direction.

One thing to be observed is the difference in shapes of the TS waves for the u and v components. It seems that the u-components are a bit twisted, with regions of negative velocity being above regions of positive velocity. This is so because TS structures are also, in a way, not just pressure fluctuations but also vorticity fluctuations, with clockwise and counter-clockwise rotating vortices within the flow. For the y-component, it seems the structures are mostly symmetrical in the x-z plane with either a positive velocity or a negative velocity passing through a given x-position at any moment.

Another thing to be noted is that the instabilities are not confined to the boundary layer (δ_{99} is around 4mm for this case). In fact they go well into the region outside the boundary layer. This means that these pressures developed within the boundary layer are also felt in the far field, albeit with a lesser intensity than near the wall.

It may seem at first that the TS waves start to form only at around x=340mm and propagate downstream. However, this is misleading due to the limitations of the colour-bar and are, in fact, generated much earlier than x=300mm (as seen in the PSD plots). In order to see the perturbations at the second microphone (x=300 mm), the plotting colors were saturated for the region close to this, as is seen in Figure 6.24.
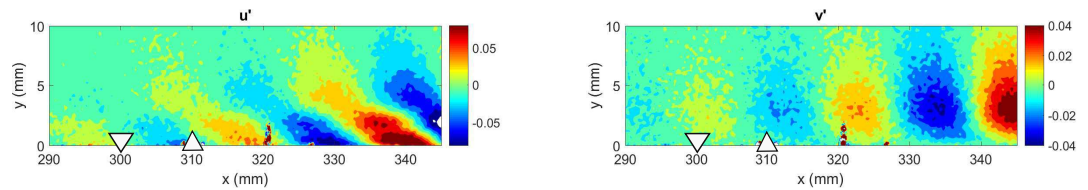
Figure 6.24: A zoomed in version with the colour bars adjusted accordingly to visualize the TS waves near the region where the actuator will be placed, x=310mm. U_∞=9.4m/s. The downward-pointing triangle represents the sensor microphone and the upward pointing microhphone represents the position of the plasma actuator

For the reconstructions of the fluctuating components for U_∞=9 and 9.8m/s, the reader is directed to Appendix A under the section Reconstructed Images.

The chosen test case for control was thus taken to be U_∞=9.4 m/s since this showed a clean spread of TS waves over the two microphones. The control location (See next section) was taken to be at x=310mm which will be the position of the plasma actuator. The downstream microphone (not shown in Figure 6.24) is at x=400mm and will measure the effect of the forcing of the plasma actuator on the perturbations at that point.

6.2. Control Implementation

The second part of this thesis and more importantly, one of its main aims is to investigate the effects of the designed Linear-Quadratic Gaussian (LQG) controller on the Tollmien-Schlichting waves present in the boundary layer. The controller was implemented as explained in Section 4.4.1 using a manufactured Dielectric-Barrier Discharge(DBD) plasma actuator. Measurement of the TS waves was done using microphones upstream and downstream of the actuator, of the same series (Linear X M53) as used in the first part of the experiment. Due to time constraints and unavailability of the low speed camera, PIV was not performed for this part.

This section mainly deals with investigating the feasibility of the controller. More specifically, the effect of the controller is studied for a range of velocities as well as for a range of base voltages. Furthermore, the effect of the controller at its design conditions is analysed followed by a robustness study (at off design conditions).

6.2.1. Pressure Measurements for the Controller

In order to make sure that the TS waves generated in the second experimental campaign are the same magnitude (since the data from the first campaign was used to design the controller), it is vital that the flexible wall provides the same C_p distribution as in the first campaign. Figure 6.25 compares the C_p for the case of U_∞=9.4 m/s.
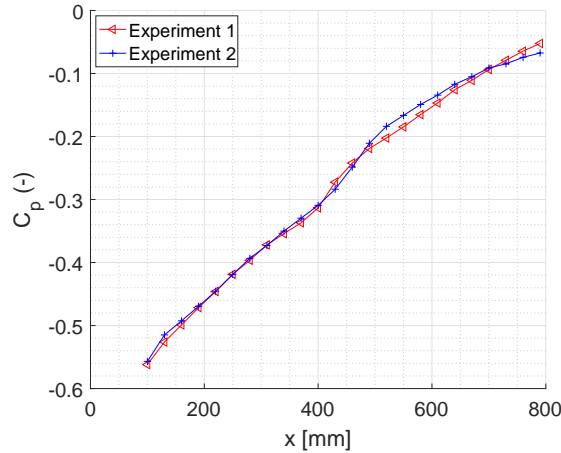
Figure 6.25: Comparing the plots of the C_p for U_∞=9.4m/s for the first and second experiment

It can be seen that the gradient of the pressure as well as the location of transition nicely line up with each other. For the region where control will be performed (x=300 mm to x=400 mm), the slope almost coincides.

As seen in the previous sections, sufficiently strong TS waves are present between x=300 mm (Microphone 2) and x=400mm (Microphone 3), for the higher range of velocities (U_∞=9,9.4 and 9.8 m/s). This is thus chosen to be our control domain and range of velocities. Since the design of the controller is such that the closer the actuation is to the sensor, the better the performance, it was decided that the plasma actuator be placed at x=310 mm, i.e. 10 mm downstream from the sensor. All analysis here onwards uses this configuration.

6.2.2. Performance at Design Conditions

The conditions for which the controller is specifically designed, viz. its nominal design conditions, was U_∞= 9.4 m/s and a peak-to-peak voltage, V_{pp} of 9kV. The CompactRio FPGA executes the control algorithm as mentioned in Section 4.4.1 (using the state estimator and state feedback) to generate the modulated signal,ϕ. However, the magnitude of this modulation is too low and must be applied over a minimum forcing (open loop case) which is required to generate plasma. This is the base or peak-to-peak-voltage. The carrier frequency was chosen to be 2kHz, and the final output signal is given by Equation 4.20.

Figure 6.26: (a) The modulatd signal,ϕ generated by the FPGA and (b) The total output signal (carrier + modulation) fed into the HV amplifier. Both signals are for the nominal design conditions, $9kV_{pp}$ and U_∞=9.4 m/s (c)zoomed in version of a small sample of Signal in (b)
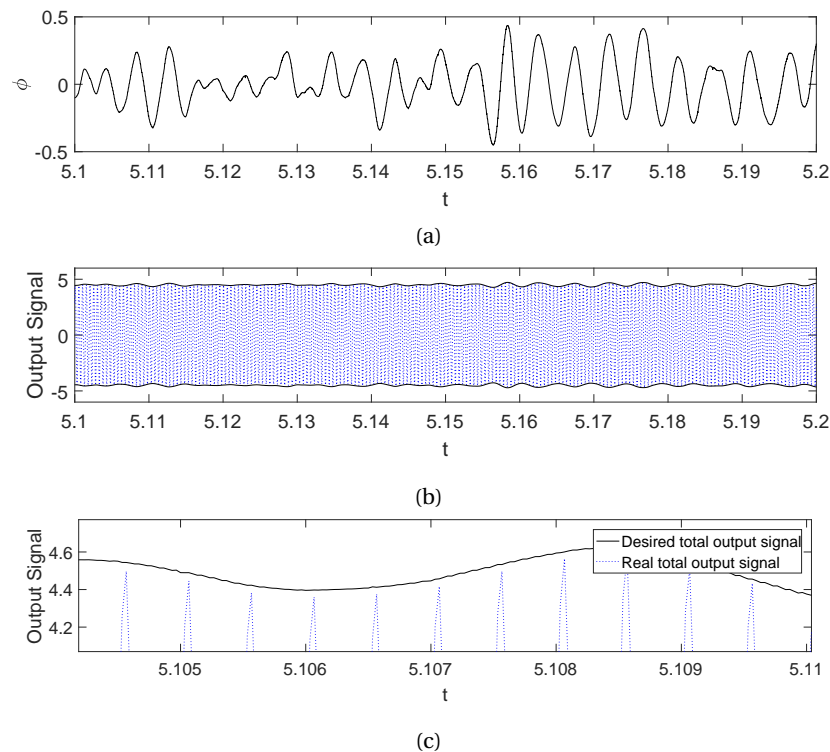
Figure 6.26 (a) and (b) represents the modulated and total output signals, respectively. All signals are multiplied with the corresponding calibration factor and filtered between 10 and 10,000 Hz to remove background and high frequency noise. Figure 6.26 showcases the slight difference in the desired signal (computed directly from the FPGA) and the real signal (signal from the HV Amplifier). This can be attributed to the internal amplifier specifications, such as resistance etc. which cause the final signal coming out from the HV Amplifier to be a bit lower in amplitude. This difference is not very significant, and for our intents and purposes, can be safely ignored.

Figure 6.27 gives the filtered signals for the upstream and downstream microphones (control off, open loop and closed loop). From Figure 6.27 (a), the typical signal for Tollmien-Schlichting waves at the upstream microphone (Mic 2) can be seen. These are visible as wave-packets and look line a bundle in the signal, which repeats over time. For the downstream microphone (Mic 3), the amplitude of the signal has grown by a factor of five, meaning stronger TS disturbance amplitudes for the control-off case. Switching on the control, the open loop case (constant actuator forcing) already shows a considerable reduction in the amplitude of the signal (Kurz et al.(2013),Widmann et al.(2013),Simon(2017). In fact, it almost reduces the amplitude of the signal to those of the upstream microphone. The constant forcing has the effect of stabilising the mean flow in a similar way that suction and blowing stabilizes the boundary layer by changing the inflection in the shape of the velocity profile.

Compared to the open-loop case, the closed loop signal clearly shows a larger reduction in the signal amplitudes. The signal amplitude has reduced to 0.3 Pa for the closed loop case from 5 Pa for the uncontrolled case. The PSD plot in Figure 6.28 gives a clearer picture of the reduction in amplitude of the dominant frequency. For the peak frequencies (around 200 Hz), the amplitude is -20dB (or 10^{-1}). On applying open loop control the signal has reduced to -55 dB (a magnitude reduction of about two-orders). The closed loop case performs even better with the peak at around -90dB. That is an overall reduction of four-orders, two orders more than the open-loop case. These results are quite significant and mean that the controller is almost twice as effective at damping peak-frequencies (only at its design conditions) than if only constant forcing was applied.
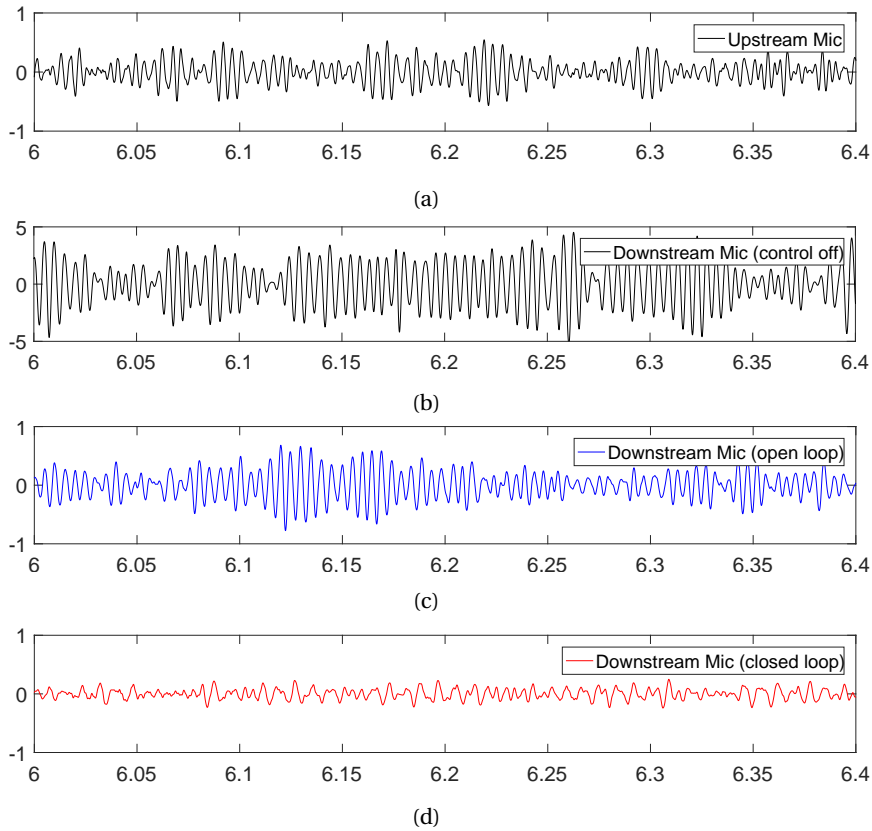
Figure 6.27: (a)Filtered Signal at the upstream sensor (Mic 2) (b)Fitered Signal at downstream sensor (Mic 3) without control (c) due to open loop control and (d) due to closed loop control. U_∞=9.4 m/s
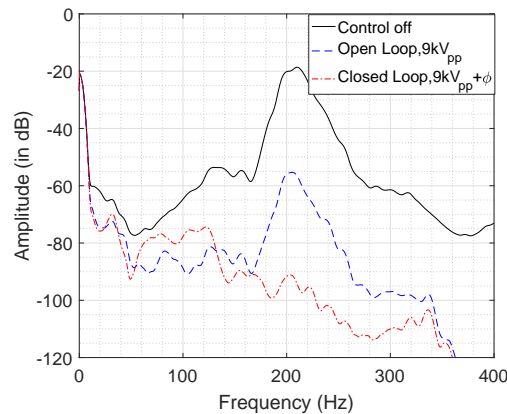
Figure 6.28: PSD plots for Downstream Mic, U_∞=9.4m/s

Another observation can be made here. Although the controller is able to attenuate frequencies in the dominant frequency mode region, it seems to amplify the lower frequencies (<150 Hz), in fact, making them even higher than the open loop case. This is attributed to what control theorists have termed 'control spillover' (Balas(1978)), whereby some of the energy of the controller is "spilled" into the uncontrolled modes (lower frequencies). Thus the actuator ends up exciting these frequencies instead of reducing them. It is hard to say whether the amplification of these smaller frequencies (which will definitely amplify as one goes downstream), will cause transition earlier or later than if LQG control was not applied. Chances are that since lower frequencies take longer to amplify than higher frequencies, transition will probably be slightly delayed, although this requires further investigation.

6.2.3. Performance at Off-Design Conditions

In order to understand the robust performance of the controller at off-design conditions, it is run over a range of velocities and voltages and the effect is investigated. The off-design velocities are U_∞=8.6, 9, 9.8 and 10.2 m/s (Table 5.8). Here PSD plots are made of the downstream microphone (Mic 3, at x=400 mm) comparing the uncontrolled case, open loop (continuous actuation) and closed loop (unsteady actuation, LQG control) case.

Effect of Free-Stream Velocity

In this section the Power-Spectral Densities for four off-design velocities are presented (U_∞ =8.6, 9, 9.8 and 10.2 m/s) at intervals of 0.4 m/s from the nominal condition, i.e. 9.4 m/s. Results are analysed for 8 kV$_{pp}$.

(a) U_∞=8.6 and 9 m/s

(b) U_∞=9.8 and 10.2 m/s
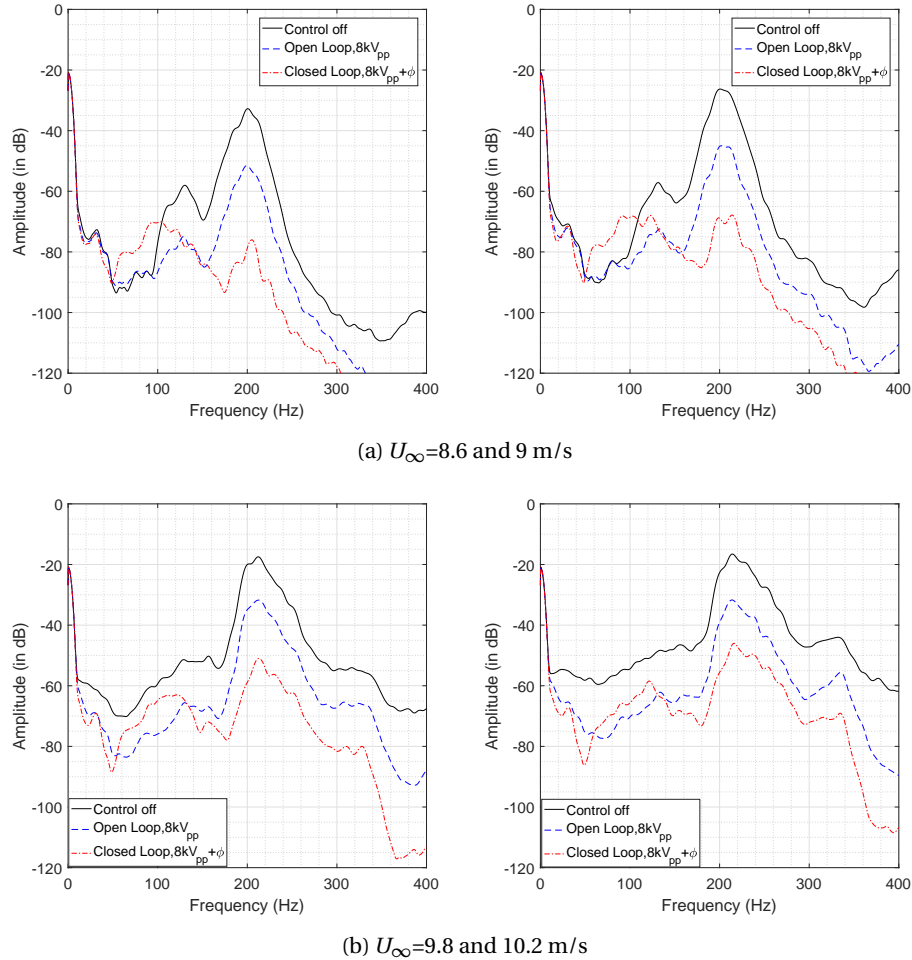
Figure 6.29: Investigating the effect of the controller for four off-design velocities at a base voltage $8kV_{pp}$

For all the cases, steady actuation reduces the dominant frequency band (180-220Hz). For the velocities below the design condition,U_∞= 8.6 and 9 m/s, the reduction for the open loop case is about 20 decibels each. For velocities above the design condition, U_∞= 9.8 and 10.2 m/s, the reduction is a bit less, being about 10 decibels.The LQG control actuation , as can be seen, is more effective at damping the dominant TS modes compared to open loop control case for all velocities. The reduction is almost two orders of magnitude, or 40dB lower than the uncontrolled cases.

It seems that the controller is better able to damp the TS modes for the lower velocities compared to the higher velocities. This is because at lower free-stream velocities, the viscous effects of the flow are more easily affected. In that sense, a constant actuator forcing and even controlled LQG forcing both are more capable of adding energy and momentum to the boundary layer, reducing the perturbations better than if the velocity was higher. At higher velocities, the added momentum due to the plasma actuator is lower relative to the free

stream velocity, hence the reduction in TS amplitudes is less. Another way of looking at this is that at these high velocities, the flow is increasingly closer to becoming turbulent and adding more energy at this stage has a lesser chance of stabilizing the already grown frequencies.

As in the case of the nominal design condition, the effects of control spillover can also be observed here, whereby the disturbance frequencies in the lower frequency range get a bit amplified compared to the open-loop case. This is visible for all the off-design velocities at the given base-voltage.

Effect of Peak-to-Peak Voltage

This section presents the effect of the base voltage (V_{pp}) on the controller performance for the cases of 9.4 m/s (nominal) and 9.8 m/s (off-design).

For the open loop case, a higher peak-to-peak voltage means that there will be a larger forcing from the plasma actuator. From Figure 6.30, it is seen that the dominant mode band has reduced substantially for the 10 kV_{pp} case compared to the 8 kV_{pp} case. For the 8 kV_{pp} case there is an open-loop reduction of about 90% (or a factor of 10 or one order of magnitude) while for the 10 kV_{pp} case there is an open-loop reduction of a factor of 1000 (three-orders of magnitude) or a reduction of 99% (the scale is logarithmic), for the peak frequencies.

For the closed loop case, the amplitude reduction of the peak frequencies is more significant. For the $8kV_{pp}$, there is an amplitude reduction of 96.8% (almost an order of 1.5) from the uncontrolled case while for the $10kV_{pp}$ case, there is an overall reduction of three-orders (99.8%) in spectral energy.
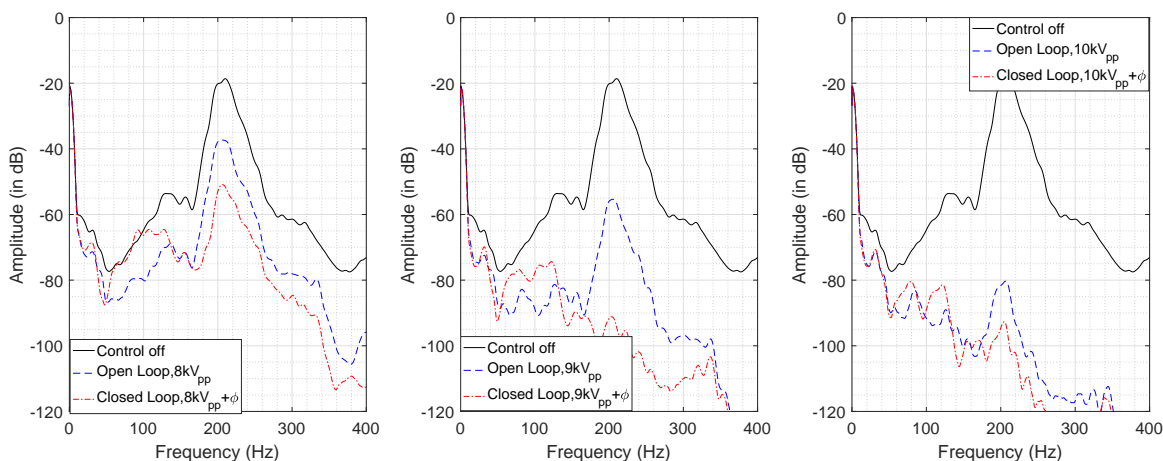

Figure 6.30: Studying the effect of Base voltage on actuator performance. $U_\infty = 9.4 m/s$

While these numbers may seem large, what matters here is the effect the LQG controller has with respect to open loop control. By that measure, the middle case ie. $9kV_{pp}$ shows the best comparative reduction. For the $9kV_{pp}$ case, there is reduction in magnitude of two orders (10^{-1} to 10^{-3}) for the open-loop case and almost four-orders ((10^{-1} to 10^{-5})) for the closed loop case. On the other hand, for the 10 kV_{pp} case, there already quite a substantial reduction of three-orders of magnitude for the open loop case, but a paltry one-order of magnitude improvement for the closed-loop case. Similarly, for the $8kV_{pp}$ case, there is reduction of about one-order of magnitude due to open-loop and another order of magnitude for closed loop. It must be kept in mind that this reduction is only for the dominant peak frequency in the band, as not all the frequencies get reduced by the controller. In fact, as seen before, the controller actually amplifies the lower frequencies due to effects of spillover.

Looking at the effect of Base voltage at a higher free-stream velocity, U_∞=9.8 m/s (Figure 6.31) further reveals that the comparative performance is best for the case of $9kV_{pp}$. Here there is an overall magnitude reduction of about two-orders due to constant forcing and three-orders due to LQG control. For the $8kV_{pp}$ case, there is about half an order magnitude reduction and one-and-a-half order reduction for the open and closed loop cases, respectively. For the $10kV_{pp}$ case there is already about three-orders magnitude reduction due to open loop, and the LQG control only reduces it by about another order of magnitude.
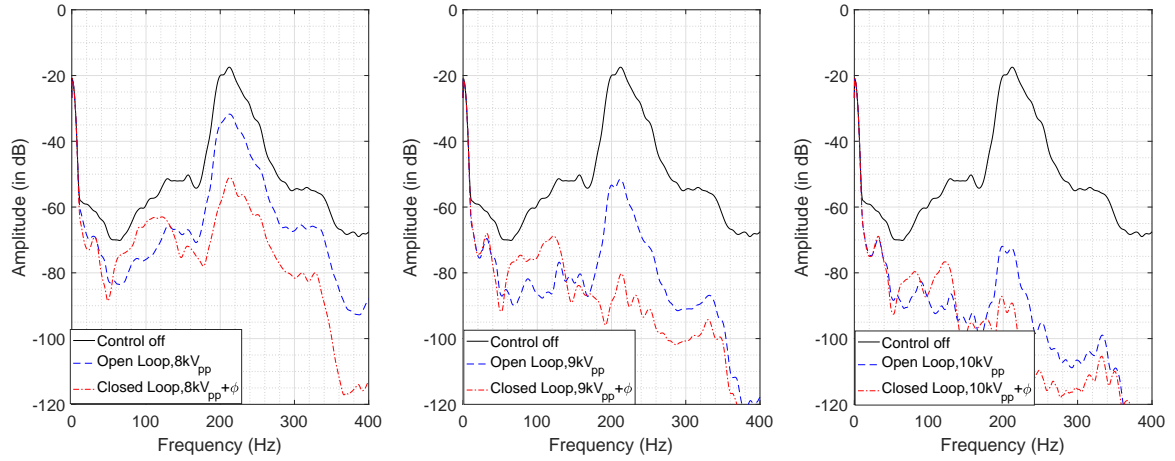
Figure 6.31: Studying the effect of Base voltage on actuator performance.$U_\infty = 9.8 m/s$

Robustness Study

In order to investigate the robustness of the controller, it is useful to compare the ratio of the standard deviation (or RMS) of the downstream signals for both open loop and closed loop cases, for a range of off-design free-stream velocities. Since RMS gives a measure of the fluctuations present in the signal, a larger value of the ratio of $\text{RMS}_{controlled}$ to $\text{RMS}_{uncontrolled}$ means that the fluctuations have not been damped very efficiently. A lower value would mean that the fluctuations left in the flow due to the control are much lower than those in the uncontrolled case, which is more effective way of measuring efficiency of the controller. Furthermore, this measures the overall robustness, i.e. the effect of the controller on the entire downstream signal rather than just the peak-frequencies.
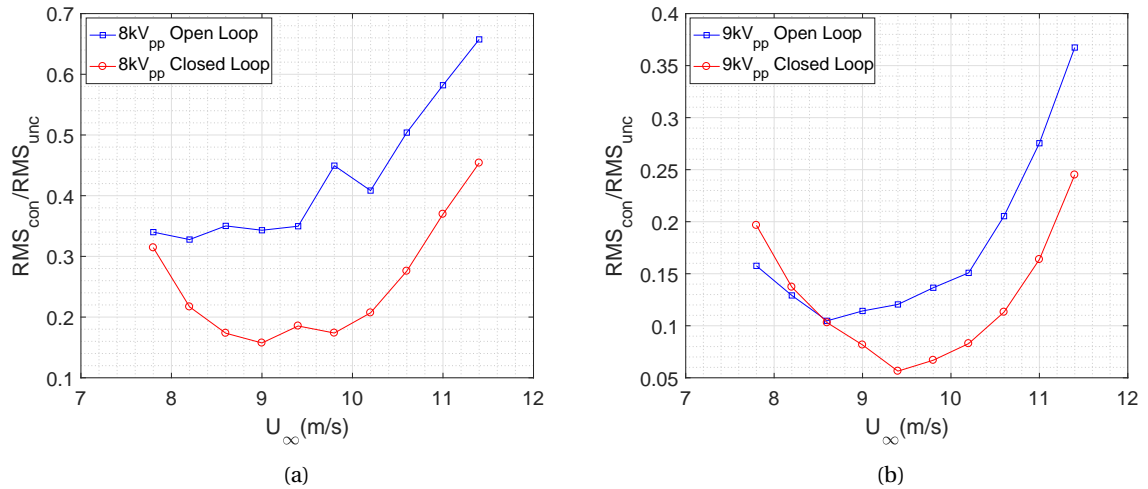
Figure 6.32: Robustness study of the controller for the open and closed loop (a)$8kV_{pp}$ and (b)$9kV_{pp}$ case for the range of free-stream velocities

Figure 6.32 (a) shows the comparison of ratios ($\text{RMS}_{con}/\text{RMS}_{unc}$) for the $8kV_{pp}$ case. The signal from the microphone is filtered using a band pass Butterworth filter of order 4 between 50 and 1000 Hz, to filter out the low frequency background noise and the high frequency noise (2 kHz) due to the operation of the plasma actuator. As expected, the closed loop damps out the fluctuations better than the open loop case, for all the range of velocities. At the design condition, there is an 65% drop in the fluctuations (from uncontrolled) for the open loop case while a 82% drop in fluctuations (from uncontrolled) for the closed-loop case. Furthermore, for the closed loop cases for $8kV_{pp}$, the ratio stays almost the same for velocities in the range of 8.6 to 9.8 m/s. This means that the controller is very robust at $8kV_{pp}$ even in slightly off-design conditions.

For the $9kV_{pp}$ case, it is also seen that the closed loop performs better at damping the fluctuations compared to the open loop, at the design condition. Here the reduction of the fluctuations from the uncontrolled case is 88% for open-loop and 94% for closed loop. This means that, compared to constant forcing, there is an additional 6% net-reduction by using the LQG controller at $9kV_{pp}$, while a 17% net-reduction by using the LQG controller at $8kV_{pp}$.

What is interesting to observe from Figure 6.32b is that the $9kV_{pp}$ case is not very robust. In fact, for a lower range of free-stream velocities (U_∞=7.8, 8.2 and 9.6 m/s), the closed loop case actually performs worse than the open loop case, with the fluctuations being amplified by the LQG controller than if constant forcing were simply applied. At U_∞=8.6 m/s , it seems that both open loop and closed loop perform the same, meaning that LQG modulation has no added benefit. Figure 6.33 also demonstrates that that the $8kV_{pp}$ case actually performs better at most of the off-design conditions compared to $9kV_{pp}$,meaning it is more robust. Only for the design-condition(U_∞=9.4 m/s) does $9kV_{pp}$ perform slightly better.
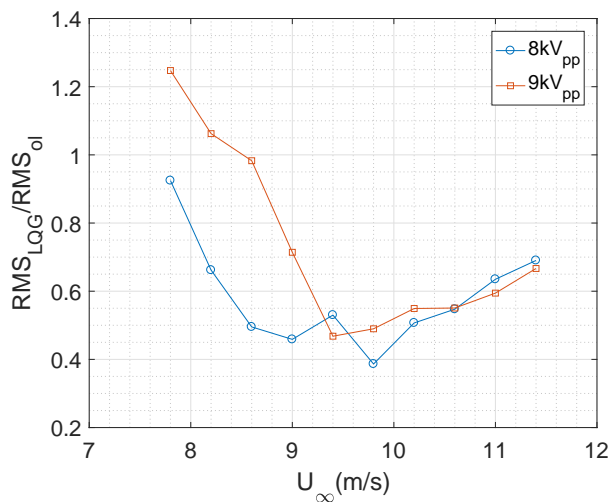
Figure 6.33: Comparison of ratio of the RMS of the LQG to the open-loop case for two base-voltages

In conclusion, the performance of the controller is summed up as follows. At the design conditions, the controller is better at damping TS waves at a base frequency of $9kV_{pp}$. However, for off design conditions, $8kV_{pp}$ is more robust. Also, comparing the relative performance improvement of the LQG controller over constant forcing, $8kV_{pp}$ performs better than $9kV_{pp}$ (at and around the design condition).

7

Conclusions and Recommendations

This section presents the main conclusions drawn from the results of the experiments carried out in this thesis. The primary research question of this thesis, as stated in the Introduction , is

"Can LQG Model-Based Control, using DBD Plasma Actuators, be used to attenuate TS waves, in an experimental setting?" In order to answer this question, it was decided that the objectives be split twofold- the identification of the TS waves and the validation of the controller.

Air was made to flow over a flat plate under the influence of an adverse pressure gradient, the strength of which was controlled using an adjustable wall opposite to the flat plate. Pressure tabs along the length of the flat plate measured the static pressure and thus the location of transition. Microphones were fitted into the body of the flat plate at specific intervals, to sample the pressure-fluctuations present within the flow. In order to quantify the flow and the boundary layer properties, Particle Image Velocimetry was carried out. Proper Orthogonal Decomposition was used to single out the most dominant energy modes and further quantify the TS waves.

For the second objective, investigating the effect of the controller on these TS waves, the same setup as the first experiment was utilized. A copper-kapton dielectric-barrier discharge (DBD) plasma actuator (positioned at x=310 mm) was employed to provide forcing within the boundary layer of the flow. A CompactRio Field-Programmable Gate Array (FPGA) designed by National Instruments executed the controller designed by Tol et al. (2017). This controller utilized the signals from the upstream microphone to generate a modulated signal which was then used to drive the plasma actuator. A downstream microphone (at x=400 mm) measured the effects of the controller by sampling the pressure fluctuations at that position.

7.1. TS Wave Characterization

The objective of the first part of this thesis was to identify and quantitatively study the behaviour of Tollmien-Schlichting waves in an adverse pressure gradient.

A series of six free-stream velocities was chosen - a lower range (U_∞=6.2, 6.6 and 7 m/s) and an upper range (U_∞=9,9.4 and 9.8 m/s) using which observations on the flow were made over all the microphones.

Pressure Analysis

Measurements of the static pressure demonstrated that the flow over the flat plate was indeed adverse, having an average value of around 0.7 m^{-1} over the first few microphones (Figure 6.1). This adverse pressure gradient varied slightly with distance, having a value of 0.87 m^{-1} between microphones 2 and 3, while reducing slightly to 0.68 m^{-1} over microphones 3 and 4. For the lower set of velocities, transition was observed to be at about x=525 mm while for the higher velocities it was found to be at x=420mm (Figure 6.2).

Spectral data analysis using the signals from the microphones showed that for the lower range of velocities, clear Tollmien-Schlichting waves are observed between Microphones 3 and 4 (noticeable as a typical bundle of frequencies having a higher power in the PSD plots, Figure 6.5).The peak frequency is observed to be around 80 Hz (having an amplitude of about -50dB). For the higher range of velocities, also clean TS waves were observed between microphones 2 and 3 (Figure 6.6). The dominant frequency is seen at around 210 Hz, and has a magnitude of around -20dB.

What is also observable is that the frequencies for the higher velocities (U_∞=9,9.4 and 9.8 m/s) are more evenly spread out over the two microphones, with them being linear in the first and on the verge of becoming non-linear in the second. This is the desired choice of spread. For the lower range of velocities, the flow has already become slightly non-linear and even possibly turbulent , and this range is thus not considered.

The two dimensionality of the TS waves was also investigated by looking at the PSD plots of two spanwise microphones at a distance of 30 mm from the centerline (Figure 6.9). The showed almost identical spectral distributions, with the peak of frequencies being at about 210 Hz for the U_∞=9.4 m/s case. Furthermore, analysis of the spanwise static pressure also revealed the C_p values (and error values) to be in the same range. Thus the flow can be considered two-dimensional in our region of interest.

Velocity Field Statistics

Time-averaged Particle Image Velocimetry (PIV) provides further insights to quantitatively estimate the behaviour of the boundary layer as well as measure the field statistics. The wavelength of the dominant frequency for the higher-velocity cases was calculated to be about 2.2 to 4.1 cm. Thus an appropriate Field of View , of size 13 cm was selected which should be able to capture a chain of a few TS waves. The time-averaged mean flow showed a growth in the boundary layer, streamwise as well as with increasing velocity (Figure 6.11). For the case of U_∞=9.4 m/s, the 99% Boundary Layer Thickness(δ_{99}) is around 3.8 mm at x=300mm and increases to 4.5 mm at x=400mm. The displacement thickness (δ^*) changes from about 1.6 mm to about 1.9 mm from x=300 to x=400 mm. The momentum thickness (θ) has an average value of about 0.6 mm. The shape factor analysis also shows the flow transitioning from linear to non-linear regimes, as the velocity profile becomes less and less full on moving downstream (Figure 6.14).

Analysis of the RMS profiles (Figure 6.15), further reveals the strength of the perturbations. For a given case the magnitude of fluctuations is higher downstream that it is upstream. Furthermore, the magnitude increases wiht an increase in the free-stream velocity. Plotting the U_{rms} profiles(Figure 6.16) reveals the double-crested curve close to the wall, a typical TS wave footprint. There is also a minima just below one-boundary layer thickness, and a bump just above it, matching that observed from literature (Grundmann and Tropea(2008)).

Investigation of the Reynolds stress profiles (Figure 6.17) tells a similar story, with an increase in the stresses at more downstream positions and at higher velocities. This is because at higher velocities, the momentum flux addition due to the stronger perturbations to the boundary layer is larger,leading to larger values in the Reynolds stress term.

Turbulent Kinetic Energy(TKE) statistics (Figure 6.19) also show that the energy of the "eddies" in the flow. Although, not turbulent yet, the statistical analysis indicates the regions having more of this perturbation energy. As expected, these plots also show a higher value of TKE (around 0.42 for U_∞=9.4 m/s) for more downstream positions as compared to upstream positions. (around 0.003 for U_∞=9.4 m/s).

Proper Orthogonal Decomposition (POD) decomposes the flow into different modes, each having its own energy. By selectively isolating and adding the modes that have the largest contribution to the overall energy in the field, one can reconstruct the flow field only showing those most energetic modes (and remove the background noise). The TS waves (coherent structures) are nicely visible in both the x and y directions (Figure 6.23). A train of them is observed, with the strength increasing on moving to more downstream positions.

The chosen test case for control is thus $U_\infty = 9.4 m/s$ with the actuator being placed 1 cm downstream from the second microphone (Figure 6.24), as this location has good measurable TS structures. Another reason for the selection of this location has to do with the logic of the controller. For model based systems, the closer the sensor is to the controller output signal, the easier it is to model and also behave more effectively.

7.2. Effect of the Controller

The second objective of this thesis is to demonstrate the feasibility of the designed LQG controller in the test setup and investigate its effect on the TS waves, as well as its nominal and robust performance.

The setup used for this part is the same as that in the first campaign, and efforts were made to obtain almost equivalent C_p distributions (Figure 6.25). The conclusions drawn in this section are based on the Power Spectral Density analysis of the downstream microphone for thee cases, the uncontrolled case (no actuation), the open loop case (constant forcing) and the closed loop or LQG case (modulated forcing).

At Design Conditions

The analysis of the controller at its nominal design conditions was investigated, i.e. U_∞=9.4 m/s and V_{pp}=9 kV. The open loop case demonstrated a reduction in the spectral energy of two-orders of magnitude of the dominant frequency while the reduction for the closed loop case was four-orders of magnitude(Figure 6.28). It must be kept in mind that this reduction of the energy is only for the peak frequencies, not the whole signal. In order to judge the reduction of the overall signal and the added benefit of the LQG control, the ratio of the RMS of the signal was computed for the controlled and uncontrolled case. For the nominal design conditions, a maximum additional reduction of about 55% is observed in the RMS of the pressure signals. Furthermore, the PSD showed that the actuator tends to amplifiy frequencies in the lower range (<130 Hz), due to the effects of control spillover.

This is a significant result and demonstrates that the LQG controller is not just feasible, but also efficient in damping TS waves, at least more than that due to constant forcing. However, further investigation in this area is recommended before any such comments about efficiency can be made.

At Off-Design Conditions

Analysis was performed at four off-design free-stream velocities (U_∞=8.6, 9, 9.8 and 10.2 m/s) at a peak-to-peak voltage (V_{pp}) of 8kV. Compared to the uncontrolled case, steady actuation (for U_∞=8.6 and 9 m/s)shows a reduction in the TS amplitudes of about 20dB. The closed loop case is even better, reducing the magnitude of the peak-frequency by 40dB (Figure 6.29). The LQG controller seems to perform better for the velocities which are lower than the design velocity compared to the velocities higher than the design velocity. This was attributed to the fact that at a lower velocity, momentum addition plays a bigger role in stabilizing the inflected profile than if the same forcing were to be applied at a higher velocity. This is true for both the open and the closed loop case, and is clearly visible.

Another effect observed is the effect of control spillover (a concept in control theory), wherein the frequencies that the controller is not designed for controlling (non-peak TS frequencies in this case), tend to get amplified. In control theory, this is due to some of the energy being "spilled" into the uncontrolled modes. This effect is also observable for the closed loop case for all the off-design velocities . Frequencies below 120Hz are amplified higher than even the open loop case.

The effect of the base-voltage was investigated for two free-stream velocities, U_∞=9.4 m/s (nominal) and U_∞=9.8 m/s (off-design). Analysis was done for V_{pp}=8, 9 and 10 kV. For the U_∞=9.4 m/s case, the actuator performs best at $9kV_{pp}$: an energy reduction of 40 decibels for the peak-frequency for the open loop case and 80dB for the closed loop case. What is important to compare is the relative performance of the LQG controller compared to the open-loop control. For the $9kV_{pp}$ case, the LQG controller shows an energy reduction of four-orders of magnitude of the peak-frequencies, two-more than the open loop case. For the $8kV_{pp}$ and $9kV_{pp}$, the improvement is only about one order-of magnitude of the peak-frequency(Figure 6.30). Again, these are only for the peak frequencies. In order to get the full picture of the overall reduction, the RMS of the pressure signals was compared for the open and closed loop cases. For the range of off-design conditions (U_∞=8.6 m/s to 10.2 m/s), a reduction in the RMS of 30-60% is achieved compared to open loop control (Figure 6.32).

For U_∞=9.8m/s, the controller again performs best for $9kV_{pp}$. There is an energy amplitude reduction of the peak-frequency of 3 orders for LQG control, compared to a reduction of 2 orders for constant forcing. For the $8kV_{pp}$ and $10kV_{pp}$, there is about a one order improvement for both (Figure 6.31).

Robust Performance

A study of the robustness of the controller (its performance away from the design conditions) is also evaluated for $8kV_{pp}$ and $9kV_{pp}$ by computing the RMS of the filtered pressure signal for the uncontrolled and the controlled case. While the LQG controller is more effective at reducing fluctuations than the open loop case, the reduction is more for $9kV_{pp}$ compared to $8kV_{pp}$ (Figure 6.27). Furthermore, it is observed that the $9kV_{pp}$ is actually less robust compared to the $8kV_{pp}$ case. In fact,for $9kV_{pp}$, the LQG controller tends to perform worse for lower velocities (U_∞=7.8 and 8.2 m/s). However, for higher velocities, $9kV_{pp}$ is still more efficient than $8kV_{pp}$.

To summarize, comparing the overall performance, $9kV_{pp}$ performs better than $8kV_{pp}$ in damping flow-instabilities, showing a maximum additional reduction of 55% in the RMS of the pressure fluctuations from the open loop case, for the design conditions. However, for off-design conditions, $8kV_{pp}$ shows more robustness with an overall reduction in the RMS of the pressure signals of 30-60% compared to open-loop forcing.

7.3. Recommendations

- The results of this thesis demonstrate that the LQG controller designed by Tol et al.(2017) is feasible and is able to damp Tollmien-Schlichting waves to a considerable degree. However, this does not mean that it is better compared to other existing model-based techniques(Fabbiane et al.(2015)) or model-free techniques (such as FXLMS, Kotsonis (2015)). In order to determine that, a comparative study will have to be performed studying not only which is better at cancelling TS waves better, and which is more robust but also which one would cause a delay in transition.

- Although it was clearly observed that the reduction in TS amplitudes was significant, it is yet to be investigated whether this actually leads to a transition delay. Although this was out of scope of this thesis, a study on whether this LQG achieves some delay would be useful in furthering the use of model-based approaches for flow-perturbation reduction, especially at a practical level

- A big assumption made in the entire thesis is that the flow is two-dimensional. The controller, too, was designed, taking this into consideration. In reality, however, flow around most bodies of practical applications is almost always 3-dimensional and it remains to be seen how the controller can be modified/tested for TS waves that vary spanwise.

- One study that was not carried out (although was intended to) was to study the effect of the distance of the actuator from the sensor signals. However, due to the fact that the current actuators were manufactured by hand, there was a large chance that each actuator would behave differently because each actuator has different force properties. This could be overcome by machine manufactured actuators, which would lead to a better characterization and more precise measurements. Furthermore, it was observed that the current actuators tended to deteriorate over time breaking down after a certain time. This is highly inconvenient, if tests of longer duration are to be performed.

- For future tests, Particle Image Velocimetry (PIV) would be an added benefit to studying the effect of the controller on the flow, since in this study, only one source, viz. microphone measurements were relied on to investigate the performance.

This study, to the author's knowledge, is the first demonstration of a white-box model-based control of naturally occuring TS waves in an experimental framework. Although promising, there is still a long way to go before this can be used as a viable drag-reduction technique.

On one hand, plasma generation often requires a bulky setup such as a high-voltage amplifier (often with a large cooling system), which is not as convenient on an aircraft as simply mounting vortex-generators. Furthermore, the use of plasma actuators as a viable drag reduction technique is still in its infancy. A lot of control techniques are still to be tested and studied before one can say how effective they are at reducing drag. Then there is also the possibility of electromagnetic interference since plasma generation causes large charge accumulations.

On the other hand, there is the appeal that model-based techniques are backed by a stronger and more elegant basis and since this can be physically understood there is also scope that this can be used to damp other flow instabilities that lead to transition, such as streaks and cross-flow instabilities. Furthermore, in the future, more than one sensor can be used to obtain upstream information or even an array of sensors could be performed. An array of actuators could also be tested, since one may not be enough to bring about significant drag reduction. There is also the possibility of using hybrid approaches, as suggested by Fabbiane et al.(2014) - having the practicalities of model-free-techniques whilst also consisting of the white-box physics of model-based techniques. Either way, this thesis demonstrates that LQG model based control as a flow control option is a means worth investigating further.

A
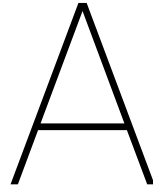
Velocity Fields Statistics

A.1. RMS Profiles

This section presents the profile of the root-mean-square of the v-component (V_{rms}) computed using PIV, for three free-stream velocities U_∞=9,9.4 and 9.8 m/s. As is seen, the fluctuations in the y-component are higher for a larger free-stream veocity , which is expected. This means that perturbations (TS waves etc) grow stronger in both the x and y-directions with an increase in free-stream velocity. The RMS of the v-fluctuations is much lower than those of the u-fluctuations since the perturbations are much stronger in the wall-parallel direction than in the wall-normal direction (as seen in the POD modes).
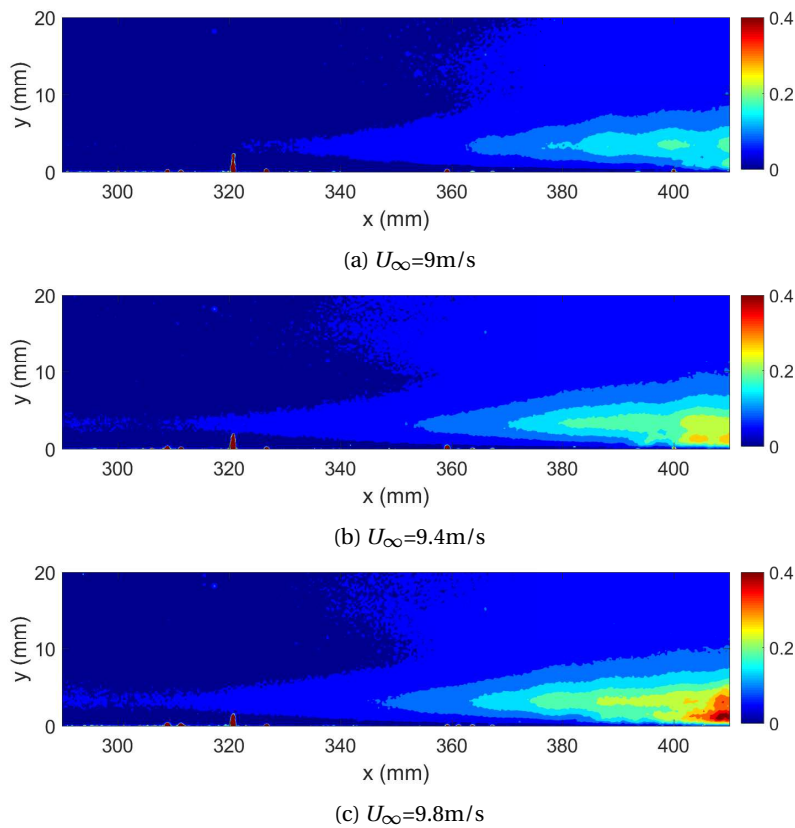

(a) U_∞=9m/s

(b) U_∞=9.4m/s

(c) U_∞=9.8m/s

Figure A.1: Contour plots of the V_{rms} for three free-stream velocities U_∞=9,9.4 and 9.8 m/s

(a) U_∞=9m/s
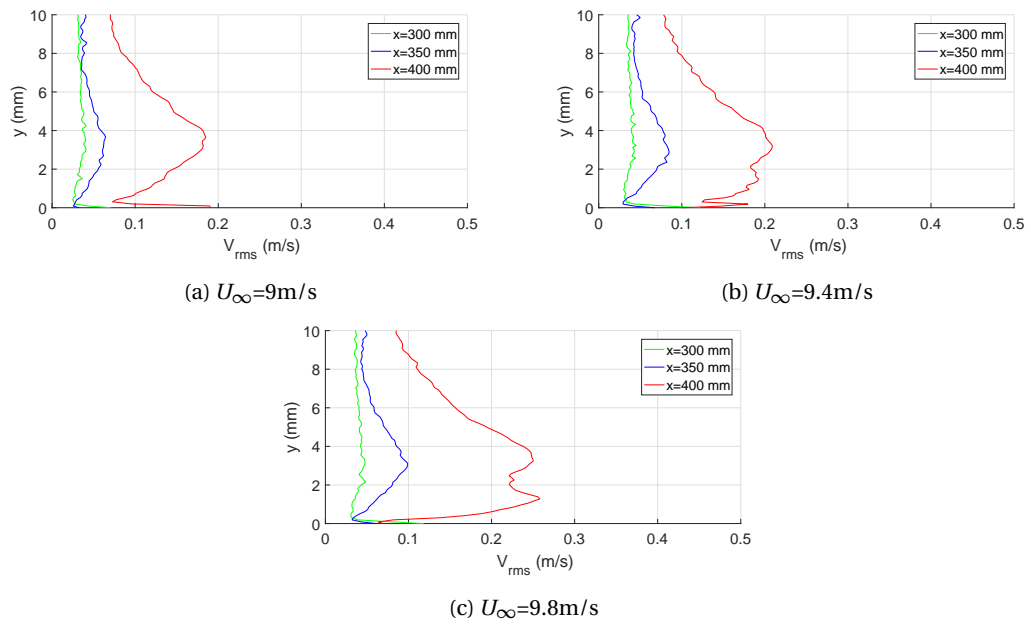

(b) U_∞=9.4m/s

(c) U_∞=9.8m/s

Figure A.2: Profiles of the V_{rms} at three streamwise positions x=300,350 and 400 mm

A.2. Reynolds Stress Profiles

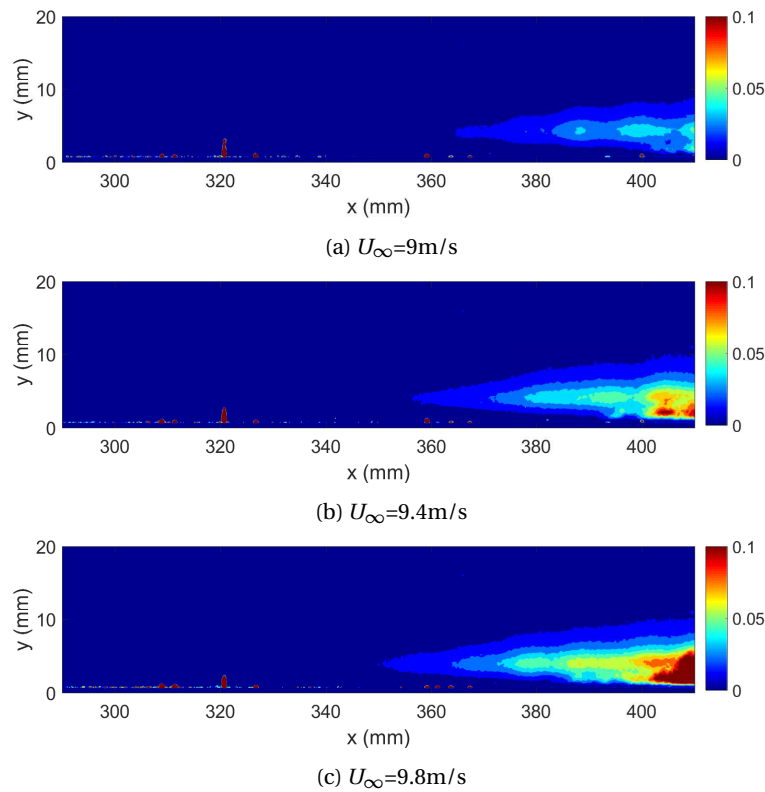This section describes the v-normal and the shear Reynolds stress values for U_∞=9,9.4 and 9.8 m/s.

(a) U_∞=9m/s

(b) U_∞=9.4m/s

(c) U_∞=9.8m/s

Figure A.3: Reynolds stresses $\rho \overline{v'v'}$ for 9,9.4 and 9.8 m/s

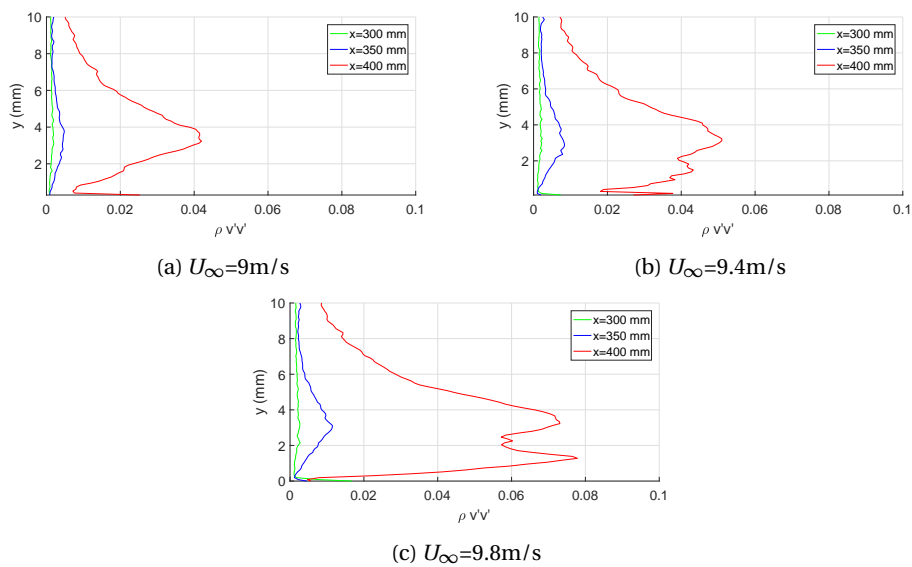

(a) U_∞=9m/s

(b) U_∞=9.4m/s

(c) U_∞=9.8m/s

Figure A.4: Profiles of the normal Reynolds stress $\rho \overline{v'v'}$ at x=300,350 and 400mm

The v-normal value of Reynolds stresses grows larger as the velocity increases, reaching a value of about 0.1 for the U_∞=9.8 m/s case. For the U_∞=9m/s case, the value is about 0.04. The Reynolds stress profiles also show that the growth is the strongest at x=400 mm as compared to x=300 mm. In fact, at x=400mm, the maximum value of the Reynolds stress grows by almost twice from U_∞=9 to 9.8 m/s, while that at x=350 mm

it grows by a factor of 1.6 over the ame range of velocities. This suggests that an increase in velocities also increases the growth rate of the fluctuations.

Figure A.5 shows the shear Reynolds stresses for the same velocities and Figure A.6 shows the profiles at three streamwise locations. Like before, similar results regarding the TS fluctuations can be observed from both diagrams.

(a) U_∞=9m/s

(b) U_∞=9.4m/s

(c) U_∞=9.8m/s
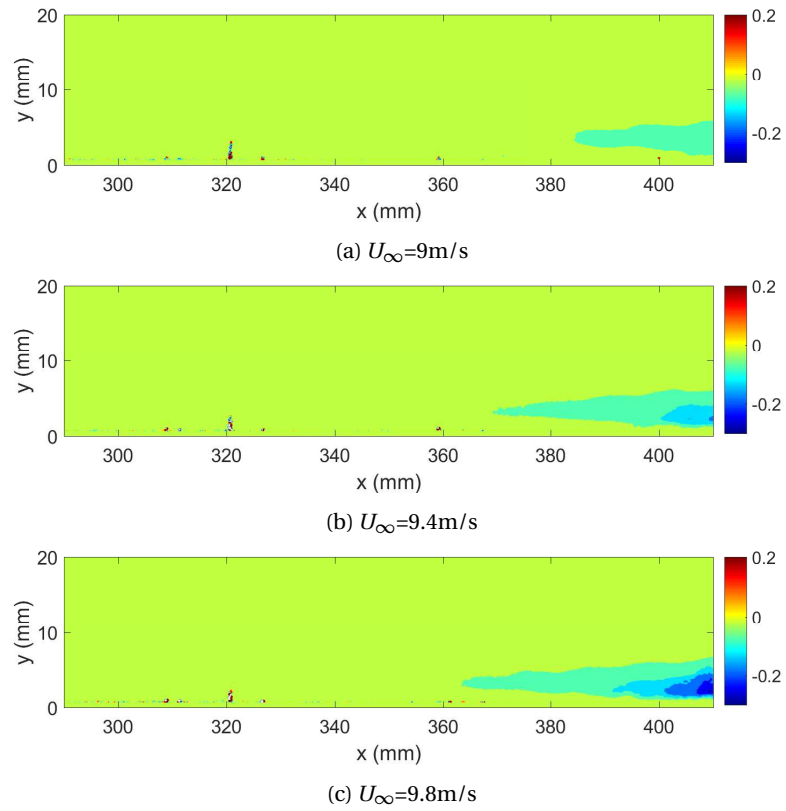
Figure A.5: Reynolds stresses $\rho\overline{u'v'}$ for 9,9.4 and 9.8m/s

(a) U_∞=9m/s

(b) U_∞=9.4m/s

(c) U_∞=9.8m/s
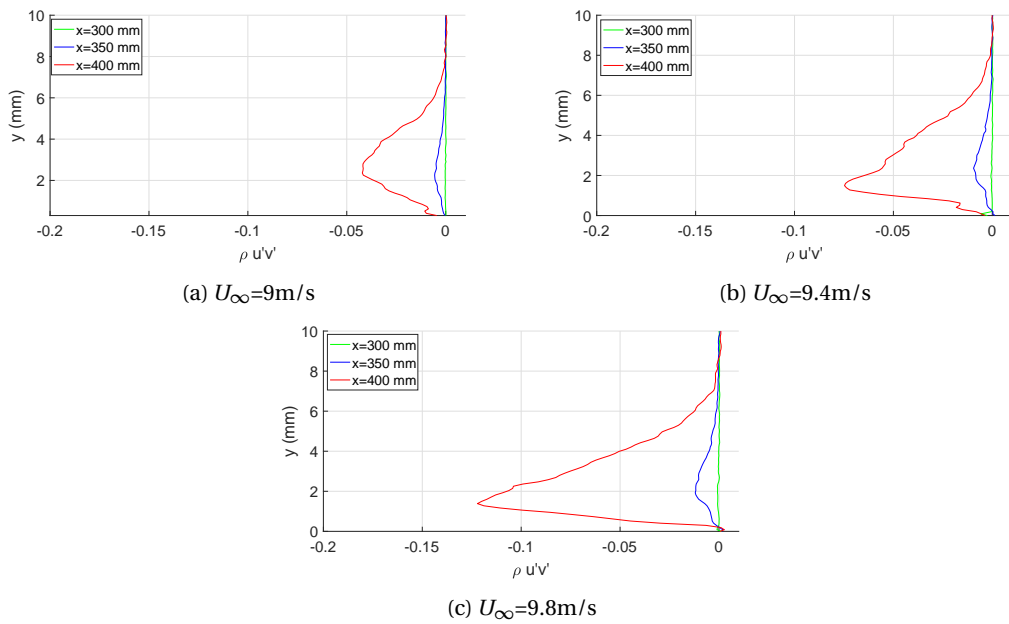
Figure A.6: Profiles of the normal Reynolds stress $\rho\overline{u'v'}$ at x=300,350 and 400mm

A.3. Modal Analysis

This section presents the first 4 modes for the velocities U_∞=9.4 and 9.8 m/s, computed using Proper Orthogonal Decomposition (POD). It should be noted that these modes do not have any physical meaning, and are simply the computed spatial eigen functions. However, they are still able to show us the highs and lows within the modal fields. For U_∞=9.8 m/s, the spatial modes are much stronger than those for U_∞=9.4 m/s, which is also as expected.
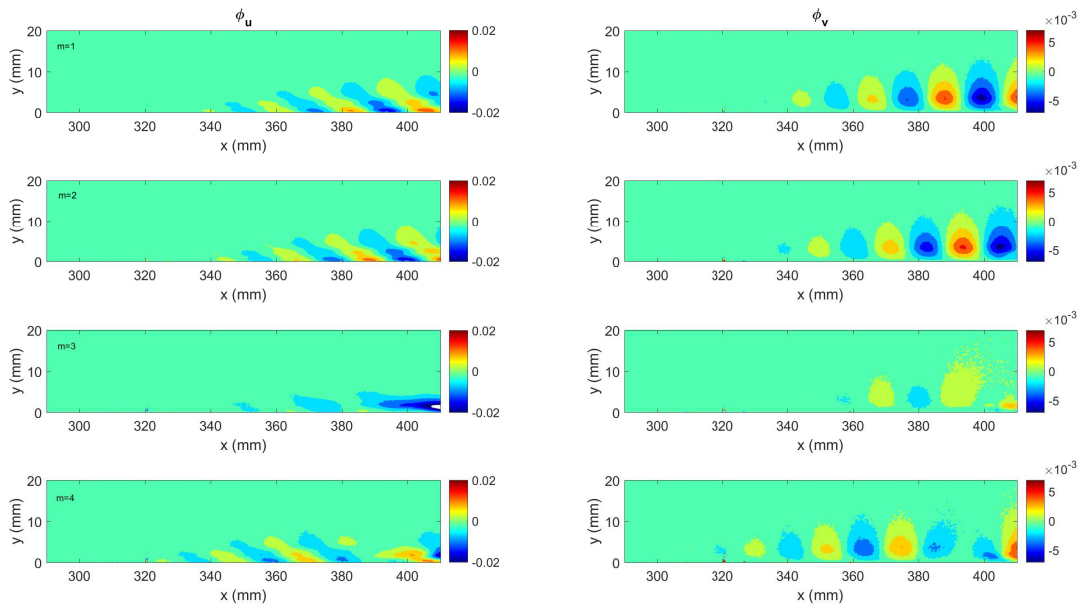

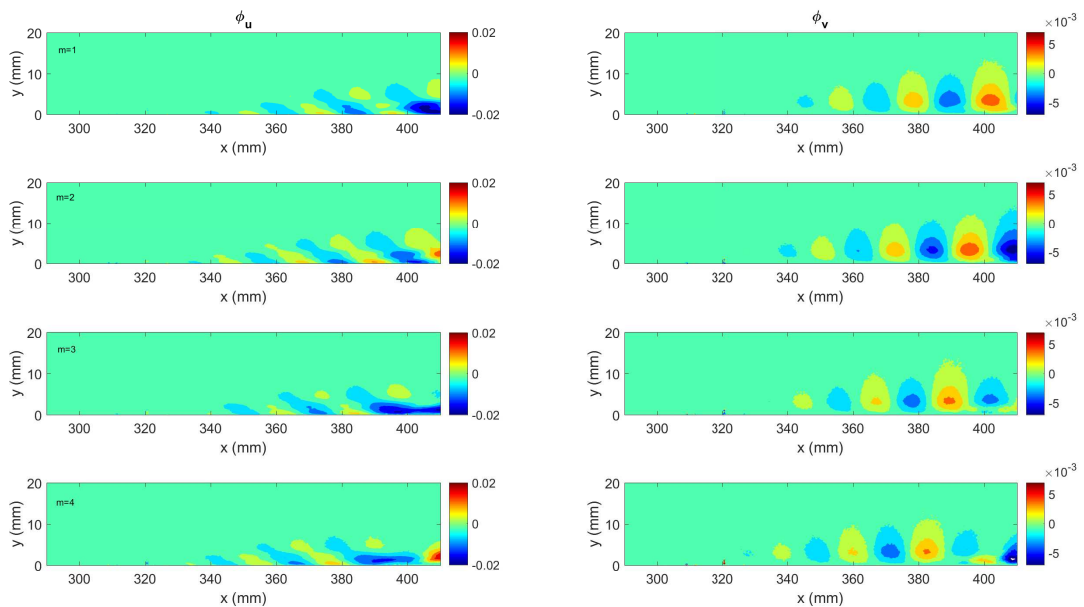Figure A.7: Eigen functions ϕ_u and ϕ_v for the first 4 modes. U_∞=9m/s

Figure A.8: Eigen functions ϕ_u and ϕ_v for the first 4 modes. U_∞=9.8m/s

A.4. Reconstructed Velocity

The reconstructed velocities for U_∞=9 and 9.8 m/s are presented in Figures A.9 and A.10. These are the first four snapshots using PIV, and are not correlated. Again like before,comparing the individual snapshots, the U_∞=9.8 m/s case showcases stronger pressure fluctuations for both the u and v-components compared to the U_∞=9 m/s case. The x-components showcase the asymmetry of the waves which also extend into regions outside the boundary layer. The v fluctuations are symmetrical in the y-z plane, an also extend well out of the boundary layer.
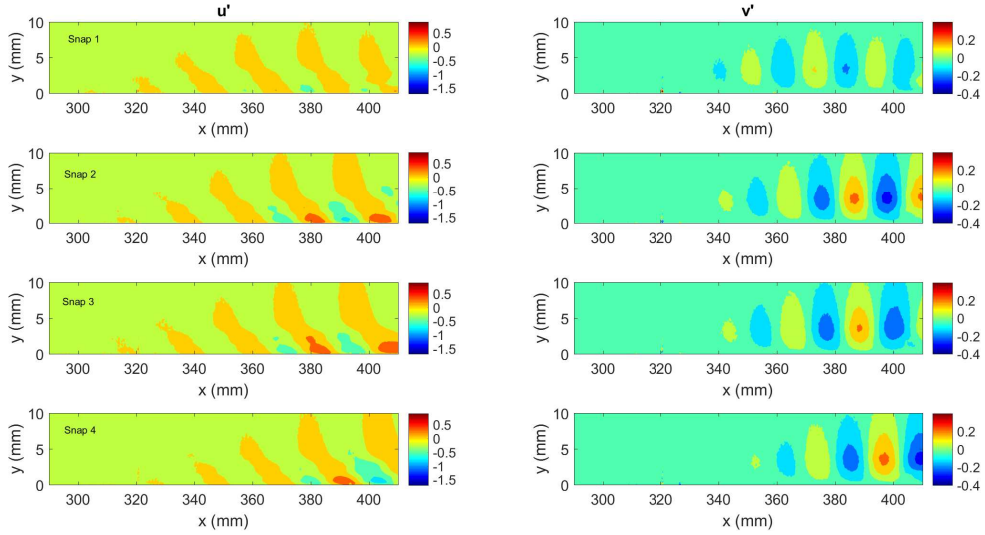

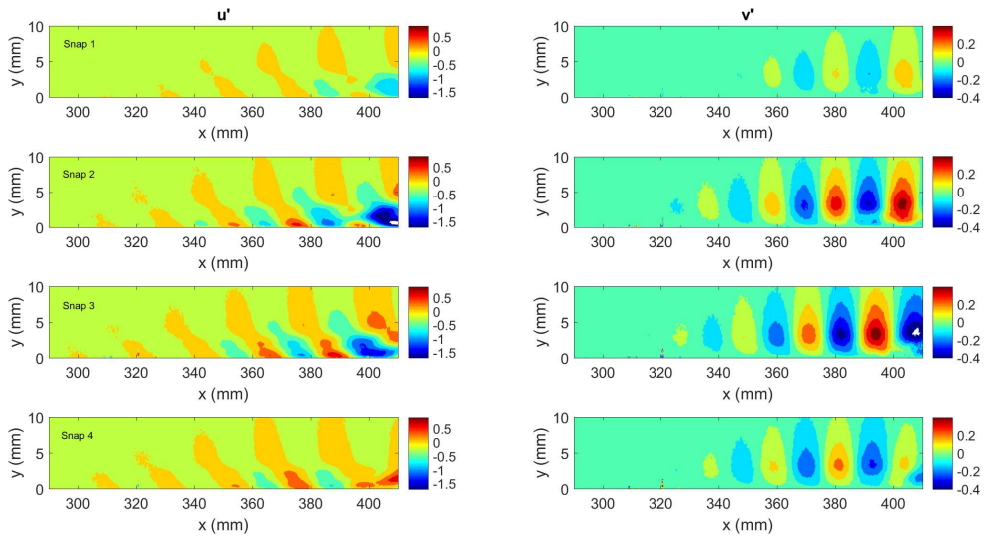Figure A.9: Reconstructed images for the fluctuating x- and y-components for the first 5 snapshots. U_∞=9 m/s

Figure A.10: Reconstructed images for the fluctuating x- and y-components for the first 5 snapshots. U_∞=9.8 m/s

Bibliography

D. Arnal. Boundary layer transition: Prediction, application to drag reduction. Technical report, Office National D'etudes et de Recherches Aerospatiales Toulouse (France), 1992.

K. J. Åström and B. Wittenmark. *Adaptive control.* Courier Corporation, 2013.

M. Athans. The role and use of the stochastic linear-quadratic-gaussian problem in control system design. *IEEE transactions on automatic control*, 16(6):529–552, 1971.

S. Bagheri and D. S. Henningson. Transition delay using control theory. *Philosophical Transactions of the Royal Society A: Mathematical, Physical and Engineering Sciences*, 369(1940):1365–1381, apr 2011. ISSN 1364-503X. doi: 10.1098/rsta.2010.0358.

M. Balas. Feedback control of flexible systems. *IEEE Transactions on Automatic Control*, 23(4):673–679, 1978.

T. R. Bewley and S. Liu. Optimal and robust control and estimation of linear paths to transition. *Journal of Fluid Mechanics*, 365:305–349, 1998.

W. L. Brogan. *Modern control theory.* Pearson education india, 1982.

S. L. Brunton and B. R. Noack. Closed-loop turbulence control: progress and challenges. *Applied Mechanics Reviews*, 67(5):050801, 2015.

T. C. Corke, C. L. Enloe, and S. P. Wilkinson. Dielectric Barrier Discharge Plasma Actuators for Flow Control. *Annual Review of Fluid Mechanics*, 42(1):505–529, jan 2010. ISSN 0066-4189. doi: 10.1146/annurev-fluid-121108-145550. URL http://www.annualreviews.org/doi/10.1146/annurev-fluid-121108-145550.

R. Dadfar and D. S. Hanifi, A.and Henningson. Feedback control for laminarization of flow over wings. *Flow, Turbulence and Combustion*, 94(1):43–62, 2015.

A. V. Dovgal, V. V. Kozlov, and A. Michalke. Laminar boundary layer separation: instability and associated phenomena. *Progress in Aerospace Sciences*, 30(1):61–94, 1994.

N. Fabbiane, O. Semeraro, S. Bagheri, and D. S. Henningson. Adaptive and model-based control theory applied to convectively unstable flows. *Applied Mechanics Reviews*, 66(6):060801, 2014.

N. Fabbiane, B. Simon, F. Fischer, S. Grundmann, S. Bagheri, and D. S. Henningson. On the role of adaptivity for robust laminar flow control. *Journal of Fluid Mechanics*, 767, 2015. doi: 10.1017/jfm.2015.45.

M. Gad-el Hak. Flow control. *Appl. Mech. Rev*, 42(10):107–109, 1989.

N. Gautier and J. Aider. Feed-forward control of a perturbed backward-facing step flow. *Journal of Fluid Mechanics*, 759:181–196, 2014.

T. Glad and L. Ljung. *Control theory.* CRC press, 2000.

N. Goldin, R. King, A. Pätzold, W. Nitsche, D. Haller, and P. Woias. Laminar flow control with distributed surface actuation: damping tollmien-schlichting waves with active surface displacement. *Experiments in fluids*, 54(3):1478, 2013.

S. Grundmann and C. Tropea. Delay of boundary-layer transition using plasma actuators. In *46th AIAA Aerospace Sciences Meeting and Exhibit*, page 1369, 2008.

S. Grundmann and C. Tropea. Active cancellation of artificially introduced tollmien–schlichting waves using plasma actuators. *Experiments in Fluids*, 44(5):795–806, 2008.

S. Grundmann and C. Tropea. Delay of boundary-layer transition using plasma actuators. In *46th AIAA Aerospace Sciences Meeting and Exhibit*, page 1369, 2008.

S. Grundmann and C. Tropea. Experimental damping of boundary-layer oscillations using DBD plasma actuators. *International Journal of Heat and Fluid Flow*, 30(3):394–402, 2009. doi: 10.1016/j.ijheatfluidflow. 2009.03.004.

T. Herbert, J. H. Haritonidis, and X. Fan. Laminar flow control with neural networks. In *ASME, Fluids Engineering Div, 1996 International Mechanical Engineering Congress and Exposition, Atlanta, GA*, pages 87–91, 1996.

A. Hervé, D. Sipp, P. J. Schmid, and M. Samuelides. A physics-based approach to flow control using system identification. *Journal of Fluid Mechanics*, 702:26–58, 2012.

S. S. Joshi, J. L. Speyer, and J. Kim. A system theory approach to the feedback stabilization of infinitessimal\r\nand finite-amplitude disturbances in plane Poiseuille flow. *Journal of Fluid Mechanics*, 332:157–184, 1997.

F. Juillet, B. J. McKeon, and P. J. Schmid. Experimental control of natural perturbations in channel flow. *Journal of Fluid Mechanics*, 752:296–309, 2014.

Y. S. Kachanov. Physical mechanisms of laminar-boundary-layer transition. *Annual review of fluid mechanics*, 26(1):411–482, 1994.

Y. S. Kachanov and V. Y. Levchenko. The resonant interaction of disturbances at laminar-turbulent transition in a boundary layer. *Journal of Fluid Mechanics*, 138:209–247, 1984.

Y. Katz, B. Nishri, and I. Wygnanski. The delay of turbulent boundary layer separation by oscillatory active control. *Physics of Fluids A: Fluid Dynamics*, 1(2):179–181, 1989.

P. S. Klebanoff, K. D. Tidstrom, and L. M. Sargent. The three-dimensional nature of boundary-layer instability. *Journal of Fluid Mechanics*, 12(1):1–34, 1962.

M. Kotsonis, S. Ghaemi, L. Veldhuis, and F. Scarano. Measurement of the body force field of plasma actuators. *Journal of Physics D: Applied Physics*, 44(4):045204, 2011.

M. Kotsonis, R. K. Shukla, and S. Pröbsting. Control of Natural Tollmien-Schlichting Waves using Dielectric Barrier Discharge Plasma Actuators. *International Journal of Flow Control*, 7(1-2):37–54, 2015. doi: 10. 1260/1756-8250.7.1-2.37.

J. Kriegseis, C. Schwarz, C. Tropea, and S. Grundmann. Velocity-information-based force-term estimation of dielectric-barrier discharge plasma actuators. *Journal of Physics D: Applied Physics*, 46(5):055202, 2013.

A. Kurz, N. Goldin, R. King, C. Tropea, and S. Grundmann. Hybrid transition control approach for plasma actuators. *Experiments in fluids*, 54(11):1610, 2013.

A. Kurz, S. Grundmann, C. Tropea, M. Forte, A. Seraudie, O. Vermeersch, D. Arnal, R. Goldin, and R. King. Boundary layer transition control using dbd plasma actuators. *AerospaceLab*, (6):p–1, 2013.

D. M. Ladd. Control of natural laminar instability waves on an axisymmetric body. *AIAA journal*, 28(2):367–369, 1990.

H. W. Liepmann and D. M. Nosenchuck. Active control of laminar-turbulent transition. *Journal of Fluid Mechanics*, 118:201–204, 1982.

N. Lin, H. L. Reed, and W. S. Saric. Effect of leading-edge geometry on boundary-layer receptivity to freestream sound. In *Instability, Transition, and Turbulence*, pages 421–440. Springer, 1992.

L. M. Mack. Transition prediction and linear stability theory. In *In AGARD Laminar-Turbulent Transition 22 p (SEE N78-14316 05-34)*, 1977.

L. M. Mack. Boundary-layer linear stability theory. *Special Course on Stability and Transition of Laminar Flow*, AGARD Report 709, 1984.

K. E. Meyer, D. Cavar, and J. M. Pedersen. Pod as tool for comparison of piv and les data. In *7th International Symposium on Particle Image Velocimetry*, volume 7, pages 1–12. Faculty of Engineering, University "La Sapienza", 2007.

T. Michelis. *Boundary Layer Separation: Diagnostics and Control.* PhD thesis, Delft University of Technology.

R. W. Milling. Tollmien–schlichting wave cancellation. *The Physics of Fluids*, 24(5):979–981, 1981.

E. Moreau. Airflow control by non-thermal plasma actuators. *Journal of Physics D: Applied Physics*, 40:605–636, 2007. ISSN 0022-3727. doi: 10.1088/0022-3727/40/3/S01.

M. V. Morkovin. Transition in open flow systems-a reassessment. *Bull. Am. Phys. Soc.*, 39:1882, 1994.

M. Raffel, C. E. Willert, S. T. Wereley, and J. Kompenhans. *Particle image velocimetry: a practical guide.* Springer, 2013.

R. Rathnasingham and K. S. Breuer. Active control of turbulent boundary layers. *Journal of Fluid Mechanics*, 495:209–233, 2003.

Lord Rayleigh. On the stability, or instability, of certain fluid motions. *Proceedings of the London Mathematical Society*, 1(1):57–72, 1879.

E. Reshotko. Boundary-layer stability and transition. *Annual Review of Fluid Mechanics*, 8(1):311–349, 1976.

W. S. Saric, H. L. Reed, and E. J. Kerschen. Boundary-layer receptivity to freestream disturbances. *Annual review of fluid mechanics*, 34(1):291–319, 2002.

F. Scarano. Reader :experimental aerodynamics, ae-4180, 2013.

H. Schlichting. Berechnung der anfachung kleiner störungen bei der plattenströmung. *ZAMM*, 13:171–174, 1933.

H. Schlichting. Boundary-layer theory. 1968.

H. Schlichting and K Gersten. Boundary layer theory springer-verlag. *Berlin, Heidelberg*, 2000.

H. Schlichting, K. Gersten, E. Krause, H. Oertel, and K. Mayes. *Boundary-layer theory*, volume 7. Springer, 1955.

P. J. Schmid and D. S. Henningson. *Stability and transition in shear flows*, volume 142. Springer Science & Business Media, 2012.

P. J. Schmid and D. Sipp. Linear control of oscillator and amplifier flows. *Physical Review Fluids*, 1(4):040501, 2016.

G. B. Schubauer and H. K. Skkamstad. Laminar-Boundary-Layer Oscillationa and Transition on a Flat Plate. (March), 1956.

G. B. Schubauer and H. K. Skramstad. Laminar-boundary-layer oscillations and transition on a flat plate. Technical report, National Aeronautics and Space Administration Washington DC, 1948.

G. B. Schubauer and H. K. Skramstad. Laminar-boundary-layer oscillations and transition on a flat plate. *Journal of Research of the National Bureau of Standards*, 38:251–292, 1948.

A. Sciacchitano and B. Wieneke. Piv uncertainty propagation. *Measurement Science and Technology*, 27(8): 084006, 2016.

A. Seifert, S. Eliahu, D. Greenblatt, and I. Wygnanski. Use of piezoelectric actuators for airfoil separation control. *AIAA journal*, 36(8):1535–1537, 1998.

A. Seraudie, O. Vermeersch, and D. Arnal. Dbd plasma actuator effect on a 2d model laminar boundary layer. transition delay under ionic wind effect. In *29th AIAA applied aerodynamics conference*, page 3515, 2011.

B. J. Simon. *Active Cancellation of Tollmien-Schlichting Waves under Varying Inflow Conditions for In-Flight Application.* PhD thesis, Technische Universität Darmstadt, 2017.

D. Sipp and P. J. Schmid. Linear closed-loop control of fluid instabilities and noise-induced perturbations: A review of approaches and tools. *Applied Mechanics Reviews*, 68(2):020801, 2016.

L. Sirovich. Turbulence and the dynamics of coherent structures. i. coherent structures. *Quarterly of applied mathematics*, 45(3):561–571, 1987.

A. M. O. Smith and N. Gamberoni. *Transition, pressure gradient and stability theory*. Douglas Aircraft Company, El Segundo Division, 1956.

J. G. Spangler and C. S. Wells Jr. Effects of freestream disturbances on boundary-layer transition. *AIAA Journal*, 6(3):543–545, 1968.

D. Sturzebecher and W. Nitsche. Active cancellation of tollmien–schlichting instabilities on a wing using multi-channel sensor actuator systems. *International journal of heat and fluid flow*, 24(4):572–583, 2003.

T. Theodorsen. Mech. anism of turbulence. In *Proceedings of seconnd Midwestern Conference on Fluid Mech. anics, Ohio State University, Columbus, OH.*, 1952.

C. Thill, J. Etches, I. Bond, K. Potter, and P. Weaver. Morphing skins. *The Aeronautical Journal*, 112(1129): 117–139, 2008.

H. J. Tol, M. Kotsonis, C. C. de Visser, and B. Bamieh. Localised estimation and control of linear instabilities in two-dimensional wall-bounded shear flows. *Journal of Fluid Mechanics*, 824:818–865, 2017. doi: 10. 1017/jfm.2017.355.

W. Tollmien. Über die entstehung der turbulenz. nachr. ges. wiss. göttingen 21–24. *English translation NACA TM*, 609:1931, 1929.

J. van Ingen. The eN method for transition prediction. *Historical review of work at TU Delft AIAA paper*, 3830, 2008.

J. L. van Ingen. Een semi-empirische methode voor de bepaling van de ligging van het omslaggebied van de grenslaag bij onsamendrukbare tweedimensionale stromingen. *Technische Hogeschool Delft, Vliegtuig-bouwkunde, Rapport VTH-71*, 1956.

H. Viets, M. Piatt, and M. Ball. Boundary layer control by unsteady vortex generation. *Journal of Wind Engineering and Industrial Aerodynamics*, 7(2):135–144, 1981.

P. Welch. The use of fast fourier transform for the estimation of power spectra: a method based on time averaging over short, modified periodograms. *IEEE Transactions on audio and electroacoustics*, 15(2): 70–73, 1967.

F. M. White. Viscous fluid flow, 640 pp, 1974.

A. Widmann, A. Kurz, B. Simon, S. Grundmann, and C. Tropea. Characterization of the interaction between tollmien-schlichting waves and a dbd plasma actuator using phase-locked piv. In *PIV13; 10th International Symposium on Particle Image Velocimetry, Delft, The Netherlands, July 1-3, 2013*. Citeseer, 2013.

B. F. A. Wieneke. *PIV Uncertainty Quantification and Beyond*. PhD thesis, Delft University of Technology, 2017.